PROCESSING, CHARACTERIZATION AND MODELING CARBON NANOTUBE MODIFIED INTERFACES IN HYBRID POLYMER MATRIX COMPOSITES

A Thesis

by

HIEU THI XUAN TRUONG

Submitted to the Office of Graduate Studies of
Texas A&M University
in partial fulfillment of the requirements for the degree of

MASTER OF SCIENCE

Approved by:

Co-Chairs of Committee,	Ozden O. Ochoa
	Dimitris C. Lagoudas
Committee Members,	J.N. Reddy
	Ibrahim Karaman
Head of Department,	Jerald A. Caton

December 2012

Major Subject: Mechanical Engineering

ABSTRACT

Multifunctional hybrid composites are proposed as novel solutions to meet the demands in various industrial applications ranging from aerospace to biomedicine. The combination of carbon fibers and/or fabric, metal foil and carbon nanotubes are utilized to develop such composites. This study focuses on processing of and fracture toughness characterization of the carbon fiber reinforced polymer matrix composites (PMC) and the CNT modified interface between PMC and a metal foil. The laminate fabrication process using H-VARTM, and the mode I interlaminar fracture toughness via double cantilever beam (DCB) tests at both room temperature and high temperature are conducted. The cross-sections and fracture surfaces of the panels are characterized using optical and scanning electron microscopes to verify the existence of CNTs at the interface before and after fracture tests. The experimental results reveal that CNT's improve bonding at the hybrid interfaces. Computational models are developed to assist the interpretation of experimental results and further investigate damage modes. In this work, analytical solutions to compute the total strain energy release rate as well as mode I and mode II strain energy release rates of asymmetric configurations layups are utilized. Finite element models are developed in which the virtual crack closure technique is adopted to calculate strain energy release rates and investigate the degree and effect of mode-mixity. Results from analytical solutions agree well with each other and with results obtained from finite element models.

DEDICATION

To my grandfather, my very first academic instructor and best friend

To my family, whose love and support I deeply treasure

ACKNOWLEDGEMENTS

I would, foremost, like to express my sincerest gratitude to my advisor, Dr. O. Ochoa, for her continuous guidance and support, for providing me with numerous opportunities for professional development, and for enthusiastically inspiring me to journey through difficulties toward my academic objectives. I sincerely appreciate her kindness and assistance, her patience in explaining and discussing the problems throughout this project. It has been a privilege and great experience working and learning under their guidance.

I also sincerely thank my co-advisor, Dr. D. Lagoudas, for his patient and kind advice, for the challenges he brought to our discussions which help me *think* and grow, for inspiring and encouraging me to achieve, to think above and beyond, and to be an independent researcher.

I would also like to thank Dr. J.N. Reddy and Dr. I. Karaman for serving on my committee and providing me with valuable comments on my work. In addition, I would like to thank Dr. J. Whitcomb for his great help and the tremendous amount of time he put on the discussions throughout different stages in the project, and for providing me an opportunity to use his research group's computational tool.

I am appreciative for the opportunity to work closely with Patrick Klein and W. Ross McLendon. I thank them for their great help and patient instructions when I first started the experimental and computational effort in this project.

Moreover, I would like to thank all of my teachers and professors over the years for helping me gain the knowledge I need and leading me to where I am today. I also would like to thank my friends and colleagues, the students and researchers in Dr. Ochoa's group, Dr. Lagoudas' group, Dr. Whitcomb's group, Dr. Sue's group, and other MURI students.

Financial support by AFOSR AWARD No FA-9550-09-1-0686 that makes the research possible is greatly appreciated.

I wholeheartedly thank the McArthur's for all their help when I first came to America as a high school and then college student, for everything they have done for me and especially, for loving me as their own child. They have become a family of mine.

Last but not least, I would like to send my heartiest appreciation to my family for the scarification they have made, for their unconditional love and support, for being with me through the highs and lows in life both academically and personally, for inspiring me and providing me with the strength I need to follow my dreams. I can never thank them enough.

TABLE OF CONTENTS

Page

LIST OF FIGURES

Page

LIST OF TABLES

Page

1 INTRODUCTION

1.1 Overview of Fiber Metal (Hybrid) Laminates

Recent vehicle technology advances have enabled aircraft to fly as fast as twenty four times the speed of sound. For example, NASA's unmanned aircraft, X-43 supersonic combustion scramjet, can fly around the world in less than two hours. However, the flight conditions are extreme and pose great challenges to typical aerospace composites operating at temperatures as high as 1650^{o}C. Future aerospace structures operating under extreme conditions as well as over a wide range of speed and extended period of time necessitate pioneering new multifunctional materials. Fiber metal laminates, herein referred as hybrid laminates, are receiving significant attention due to their perceived enhancements in fatigue, impact and residual strength [1]. Some fiber metal laminates are of sandwich construction where thin foil metal is the skin and the core is polymer matrix laminate, whereas others are more intermingled through the thickness. By combining these two material systems, the advantages of each constituent are optimally utilized while their weaknesses are reduced. The concept of hybrid laminates was initiated in 1978, when the first generation of fiber metal laminates called ARALL (Aramid fiber composite/aluminum laminate) were fabricated at the Delft University in The Netherlands [2]. Since then, different variants of fiber metal laminates were developed such as GLARE (GLAss REinforced laminate), TiGr (Titanium Graphite laminate), CARALL (CARbon fiber composite/ALuminum Laminate). Khan et al summarized pros and cons of different Fiber Metal Laminates (FML) and their

advantages over monolithic materials respectively as depicted below in Tables 1.1 and 1.2.

Table 1.1 Pros and Cons of different fibers for FMLs [3]

Fiber	Advantage	Disadvantage	Available laminates
Aramid	Low weight	Low strength	ARALL
Glass	High strength High failure strain	High weight Low stiffness	GLARE
Carbon	Low weight High stiffness High strength	Low failure strain Corrosion issue Expensive	TiGr CARALL

Table 1.2 Advantages of FMLs over monolithic materials [3]

Improved material behavior	+Fatigue +Fracture toughness +Impact +Corrosion
Increased safety	+Improved material behavior +Fire resistance
Possibilities for cost saving	-Material cost +Operating cost +Maintenance and inspection +Production simplification

One of the leading generations of fiber metal laminates, which has been considered as a material used for the wings in Boeing 7A7 and several other

applications, is titanium graphite laminate, TiGr. A TiGr laminate consists of laminated polymer matrix composite core with titanium skins as illustrated in Figure 1.1.

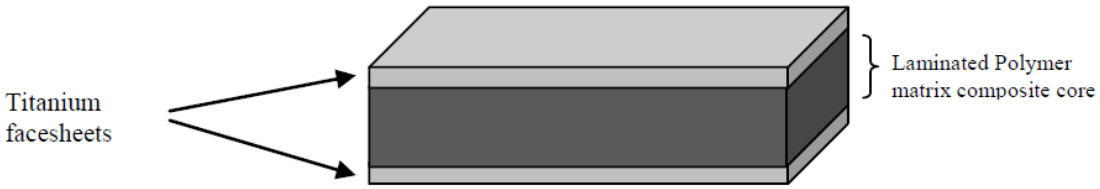

Figure 1.1 TiGr Laminate Schematic

The Titanium layers protect the polymer matrix composite core from oxidation, moisture and other environmental, temperature dependent effects while enhancing impact resistance [4]. In addition, because of the higher strength to weight and stiffness to weight ratios that the PMC core has, compared to the Titanium face sheet, it is said that the composite core is less sensitive to fatigue effects [5]. As a result, TiGr laminate has a combination of advantages from each of these two constituents such as high strength and toughness, excellent impact resistance, electrical conductivity, ease of machining and repairing from Titanium layers and high strength and stiffness, good fatigue and corrosion resistance from the polymer matrix [6, 7].

The concept of fiber metal laminates was originally developed to further improve the fatigue resistance of metal laminates. Yet at present, a reliable and accurate

predictive capability of metal laminates is lacking in spite of considerable research efforts focusing on GLARE and TiGr.

Recently, it has been proposed that the research on multifunctional hybrid composites consisted of multi-layers based on the concept of TiGr and GLARE is conducted to develop novel materials used in the prospective generation of aerospace vehicles for different purposes [2]. Some suggested functions that these composites will perform include self-sensing of damage and failure, actively cooling and self-healing, thermal/environmental and damage propagation barriers, mechanical damping, load bearing.

1.2 Interface Improvements

Compiled of different constituents, metal laminates, i.e. hybrid composites, are heterogeneous systems and thus require thorough understanding of their response both in static and dynamic loading, potential failure mechanisms including in and out of plane. Simple loading conditions such as longitudinal tension and compression, transverse tension and compression, and in-plane shear need to be simulated to assess local buckling, matrix cracking, fiber fracture, fiber-matrix delamination and interlaminar debonding. Of these damage mechanisms, the most critical is the interfacial debonding especially in this class of hybrid composites of the interface between fiber and matrix.

Generally there are two different approaches to improve the performance of composites: enhancing the properties of each individual material or upgrading the capabilities of the composite as a whole system [8-11]. However, the first approach

seems less effective since it does not address the critical debonding of interfaces. Several solutions to improve resistance to delamination have been suggested and studied including z-pining, stitching, 3D-textiles. All the solutions mentioned above reinforce the composites in the z-direction and inadvertently cause reduction of the in-plane properties reduction, for instance, matrix damage due to the insertion of z-axis pins [8, 9, 10, 11]. Another potential solution is the reinforcing the interface between laminae by introducing a layer of carbon fiber/fabric with carbon nanotubes grown on the surface. Furthermore, such an approach may also lead to thermal and electrical tailorability without altering specific stiffness and strength. Studies have shown that polymer nanocomposites utilizing carbon nanotubes can overcome poor interfacial adhesion and demonstrated increases in modulus by 68% and strength by 22.9% [12, 13] and other mechanical properties. Bekyarova et al stated when compared to the carbon fiber composites which did not contained carbon nanotubes, those with carbon nanotubes reinforcement enhanced the interlaminar shear strength by approximately 30%, significantly improved out-of-plane electrical conductivity, while preserving in-plane mechanical properties [14].

There are various processes to grow carbon nanotubes on fibers. Two of the most efficient and common procedures are chemical vapor deposition and electrophoresis. The chemical vapor deposition method has been used efficiently for the growth of carbon nanotubes on various surfaces such as glass fiber, and is proposed to grow carbon nanotubes on metal substrates. Aligned carbon nanotubes can be grown on either the fiber surfaces or individual fibers. It is worth noting that carbon nanotubes are grown on

all of the fiber but are not always uniform. In other words, carbon nanotubes forests can be separated from each other at the microscale. Figures 1.2 and 1.3 below show the plane view of carbon fiber (within the carbon fabric reinforced with carbon nanotubes in this study) with carbon nanotubes vertically grown using the chemical vapor deposition method under the low-magnification optical microscope and high-resolution scanning electron microscopy.

Figure 1.2 T650 carbon fiber bundle with CNTs as viewed under optical microscope

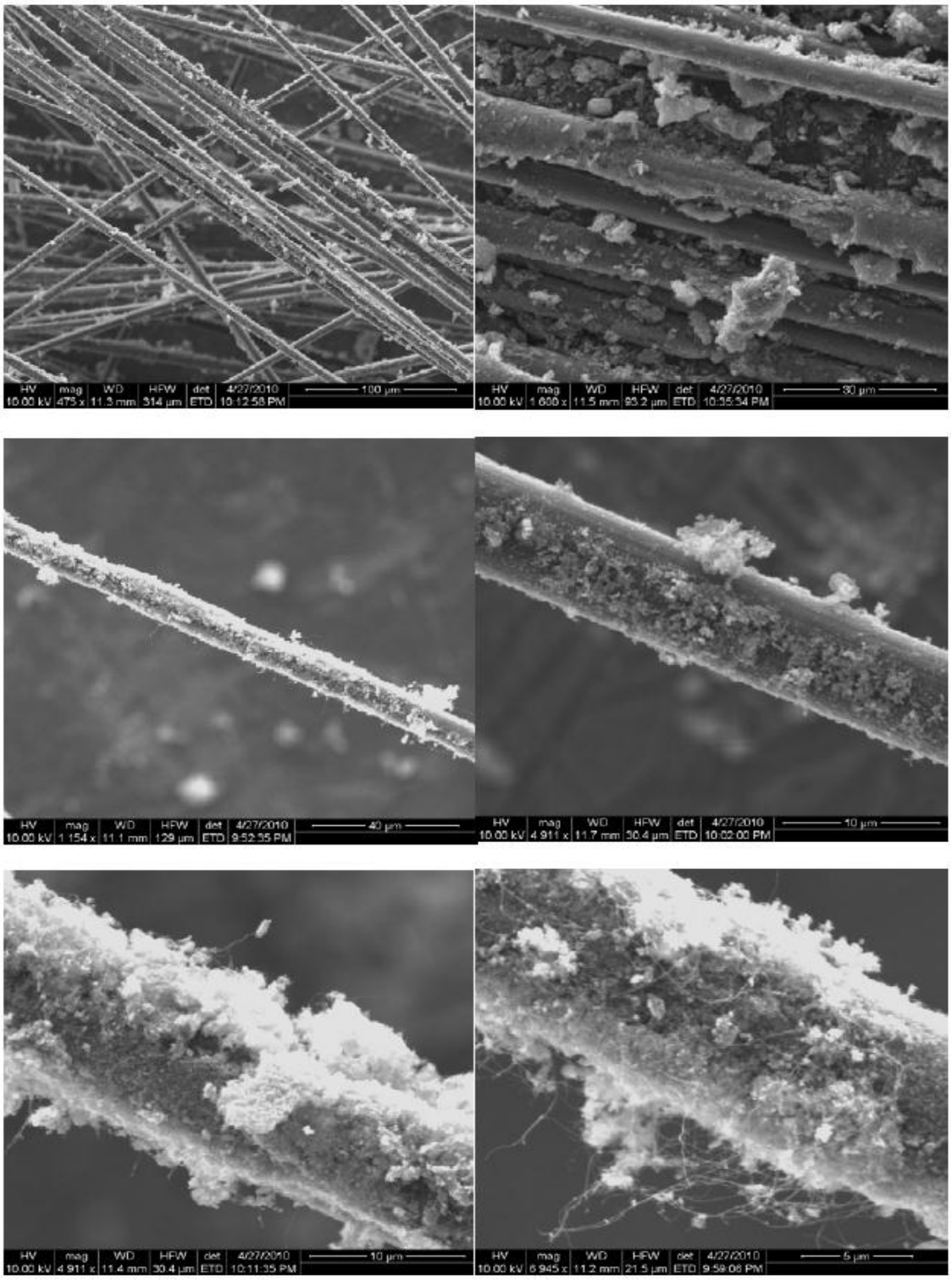

Figure 1.3 SEM micrographs of fuzzy T650 fibers

1.3 Objectives

The objectives are to fabricate and characterize Metal-PMC composites (hybrid laminates) subjected to thermo-mechanical loads experimentally and computationally. The metrics of interest are the resistance to delamination of the hybrid interface, as a function of temperature.

1.4 Approach

In this study, we focus on the assessment of fracture toughness of polymer matrix composite (PMC) and Metal-PMCs with interfaces where carbon nanotubes (CNT) are grown directly on carbon fabrics (fuzzy fabric) and Titanium foil (fuzzy Ti). Various panels with hybrid fuzzy interfaces are designed and fabricated. The laminates are then characterized by thermal-mechanical analyzers such as dynamic mechanical analyzer (DMA), differential scanning calorimetry (DSC), thermal gravimetric analyzer (TGA). Double cantilever beam (DCB) tests are conducted at both room temperature (25^{o}C) and elevated temperature (110^{o}C). Different imaging and spectroscopy techniques are utilized to observe and verify the presence of CNT in the manufactured hybrid composite panels and at the interfaces, before and after each experiment. In addition, computational models are created to help further understand the double cantilever tests, specifically to assess any potential presence of mode mixity due to the asymmetric geometry and different materials at the interface.

2 FABRICATION OF PANELS AND SAMPLES

2.1 Material Systems

Three different series of hybrid composites are fabricated to investigate the effect of carbon nanotubes at the hybrid interfaces

2.1.1 IM7 carbon fabric and Epoxy matrix

In the first phase of this study, comparisons are made between two panels, one with carbon nanotubes at the interface, and the other without. Both 4-harness satin weave IM7 carbon fabric and 8-harness satin weave T650 carbon fabric are utilized in this panel where the marix is EPON 862 epoxy. Carbon nanotubes were grown on both surfaces of a single layer T650 fabric carbon fabric and will be denoted herein as fuzzy T650 fabric. A Teflon layer was inserted in the center of the layup to create the initial crack. A schematic of the layup for this series is visualized in Figure 2.1.

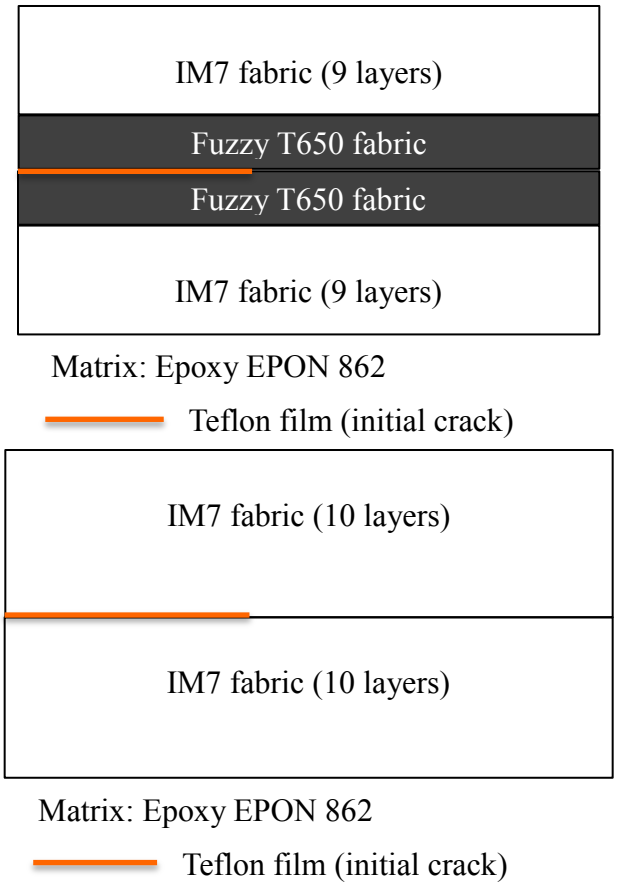

Figure 2.1 Schematic of IM7/EPON 862 Series

2.1.2 T650 carbon fabric and Epoxy matrix

In the second phase of this study, DCB tests are conducted with two separate panels with and without carbon nanotubes at the interface, as a function of temperature: at room temperature (25^{o}C) and high temperature (110^{o}C). The reinforcements used to make this second series of composites panels are 8-hardness satin weave T650 carbon fabric and fuzzy T650 carbon fabric. A T650 fabric with carbon nanotubes grown on both of its faces using the carbon vapor deposition method is called fuzzy T650 fabric.

The matrix is EPON 862 epoxy. The initial crack is created by a layer of Teflon film, placed in the middle of the layup. A schematic of the layup for this series is visualized in Figure 2.2.

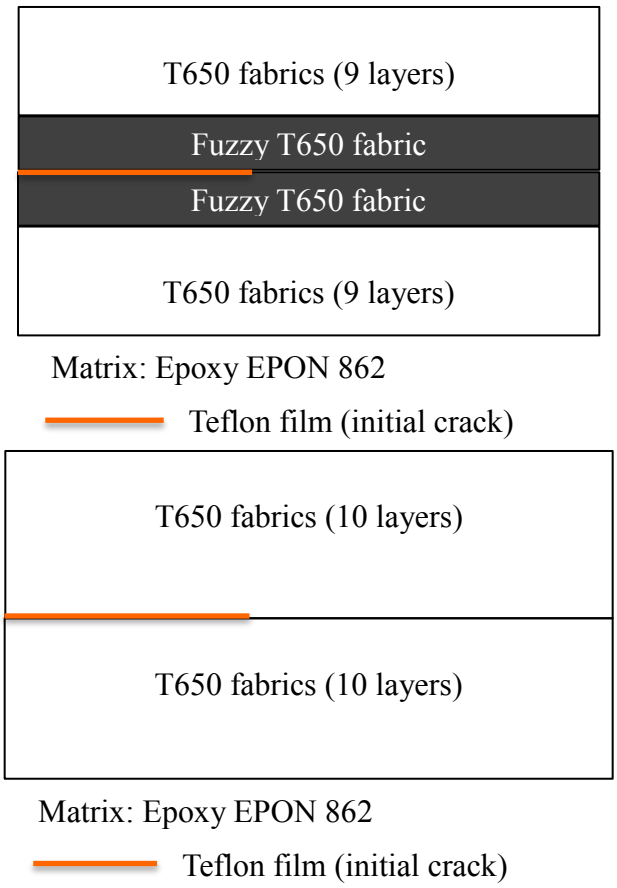

Figure 2.2 Schematic of T650/EPON 862 Series

2.1.3 T300 carbon fabric, Titanium foil and Epoxy matrix

In the third phase of this study, the hybrid composite laminates are composed of T300 plain weave carbon fabric, fuzzy T300 plain weave carbon fabric, plain Titanium foil (Ti foil as received from manufacturer), fuzzy Titanium foil, and EPON 862 epoxy matrix. A T300 fabric with carbon nanotubes grown on both of its faces using the carbon vapor deposition method is called fuzzy fabric or FF. Similarly, fuzzy Titanium foil, denoted as fTi, designates Titanium foil with carbon nanotubes grown on one side of its surfaces. The initial crack, created by Teflon film, is located between the Titanium foil and a layer of fuzzy fabric. A schematic of the layup for this series is shown in Figure 2.3.

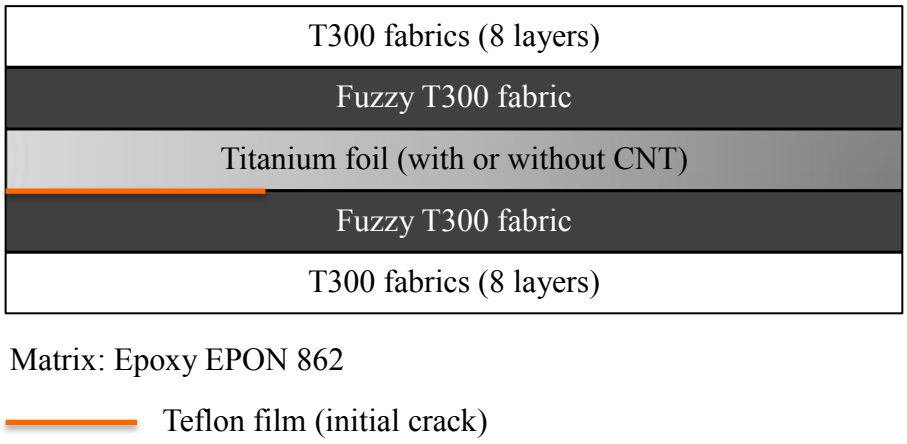

Figure 2.3 Schematic of T300/Ti/EPON 862 Series

2.2 Layup and Cure Process

All of the composite panels for this study are fabricated using the heated vacuum assisted resin transfer molding process, referred to as H-VARTM. The H-VARTM process contains five main steps: preparing the mold plate and laying up fabric, sealing the mold and creating a vacuum, preparing and degassing the resin, injecting the resin into the fabric lay-up and curing the fabricated laminates. Since the manufacturing process is the same for all three sets of composite panels, the following detailed descriptions for fabrication steps are for the third series laminates: the T300 plain weave carbon fabric, Titanium foil and Epoxy matrix.

The fuzzy T300 fabric received from the University of Dayton have the size of 10.75 in by 13 in. It was cut into four pieces of the same size 5.38 in by 6.5 in, used in fabrication of two different panels. Sixteen pieces of plain T300 fabric of 6.5 in by 8 in dimensions were cut for each panel layup. The fuzzy and plain Titanium foils were of size 6.5 in by 7.5 in. It is important that the fabric got cut carefully because the fabric is frangible, therefore, if the change in weaves of the component fabric, or bending of the fibers can affect the properties of fabricated laminates. The mass of the fabric plies was then determined to calculate the volume fraction of fibers and resin. A summary of the panel layup, material density as well as mass measurements and fiber volume fraction calculation can be found in Table 2.1. Three sheets of yellow vacuum bag material of sizes 9.5 in by 12 in, 11 in by 13 in, and 22 in by 22 in were cut. Two pieces of peel ply material (white, silky cloth) were cut of dimensions 7 in by 11 in and 7 in by 11.5 in. Since this material does not permanently attach to the fabricated laminates, it was used

for the ease of removal after curing process. Screen material was utilized to make sure that the resin flows in, on, under and through all the plies. Three pieces of screen were cut with dimensions and orientations of 6.5 in by 11 in at 90^o, 6.5 in by 12 in at 90^o and 45^o. Breather material (white cotton material) is used, so there exists no air between the two vacuum bags during fabrication process. A release Teflon film of size 6.5 in by 3.5 in was created for crack initiation. Therefore, it is essential that the edges of this thin blue film were cut as straight as possible. To achieve this, a brand new razor blade was used.

The next step was laying up the panel. Sealing tape was applied along the edges of a clean glass plate, leaving a gap of about half an inch from the edges. This will be used to seal the outer vacuum bag. Similarly, sealing tape is applied on the plate for the inner vacuum bag, forms a rectangular of size 10 in by 12.5. The 9.5 in by 12 in vacuum bag was then stuck on the plate, inside the rectangle created by the sealant tape. After that, the screen and peel ply material pieces of 11 in long were placed on top of the yellow bag, respectively. The fabrics and Titanium foil were then stacked on top of the peel ply $[0]_8$/FF/Ti/FF/$[0]_8$ and $[0]_8$/FF/fTi/FF/$[0]_8$ for the FF/Ti and FF/fTi panels respectively. The Teflon film used to create initial crack was placed in the between the two inner plies mentioned above and from one end of the plies. On top of the stack formed, the remaining peel ply sheet and the other two layers of screen material were situated. The inlet tubing for resin inlet and outlet tubing for vacuum were then created. These tubes consisted of 9.75 in spiral tubes connected to 6 in Viton tubes. They were then wrapped by yellow tape and stuck to the existing yellow-tape-rectangles at the two

edges of the peel plies. On the parallel, opposite sides of the yellow tape rectangle, the yellow-tape-rolls, which had diameter-matching size of the Viton tubes and tape wrapped around them, were placed in line to ensure symmetry and that the vacuum bags will be sealed properly. The inner vacuum bag was then placed on top of the lay-up. This bag was sealed carefully until it is seen that the peel ply, the release film forming the inner bag was smoothly wrapped over the preform underneath. Then, the free end of the vacuum Viton tube was connected to the vacuum pump, the resin inlet Viton tube is clamped off. A small test was performed to check if there existed any leakage in the inner vacuum bag. This was done by listening to the noise of air leakage. If none of this noise found, and the vacuum was dropped to about -29 or -30 mmHg, the vacuum pump was turned off for about half an hour. If the pressure indicated on the pump scale goes up less than 5% of the vacuum pressure, no leakage existed. If there was a leakage, the bag needed to be checked and sealed again until it was confirmed that there is no leakage; otherwise, breather materials were placed along the edges of the peel plies. Figure 2.4 (a), (b), (c), (d) and (e) show the bottom plain T300 fabric stack, the fuzzy Titanium foil, the layup after putting Ti foil stacked, the finished layup and the first vacuum done respectively.

The outer vacuum bag was then put on top. Again, it is important to make sure that there was no leakage from the outer bag. The vacuum was then left on for about twelve hours or overnight to make sure the seal was good and the layup is completely vacuumed. This is very important for the resin infusion process. After vacuuming, the assembly was ready to be injected by resin.

Resin was then prepared. A container holding 140.04 grams of EPON 860 resin was put in a preheated oven at 122^{o}C for ten minutes. Then the resin was well-mixed with 36.98 grams (or 26.4 percent of the mass of resin), EPIKURE W curing agent. The mixture was placed in a vacuum oven for degassing. The oven was vacuum pumped and heat to 50^{o}C. Keep the resin in the vacuum until there were no bubbles on the resin surface.

During the resin degassing process, the created assembly and resin infusing assembly were heated up. This step was done to make sure that there was no difference in temperature between the assembly and prepared resin. A temperature sensor was placed at the bottom of the glass plate, underneath the fabric layup and then put on top of the heating pad. The heating instruments were set to about 65^{o}C and it was waited until the desired temperature reached.

Next step was the resin infusion. The vacuum Viton tube was clamped off and a clip was placed on the connecting tube between the resin container and the resin inlet Viton tube. This Viton tube was then unclamped. Pressure and vacuum in the preform were maintained. The clip previously placed on the connecting tube was then carefully unscrewed and adjusted to regulate the resin flow rate. It is important that the resin flowed relatively slow to make sure that every part of the layup was infused resin. The location of the resin over the preform was marked after every one minutes. This was done to help with studying in resin flow rate if necessary. Figure 2.5 below shows an example of the top view of the layup after resin injection. Schematic of the cross-section of the layup is shown in Figure 2.6.

After the resin was completely injected, the Viton tubes were clamped off, and temperature sensor was removed. The whole assembly was then placed in a preheated oven cured at 122°C for two hours and 177°C for another two hours. During the curing process and at least 12 hours post-curing, the preform was held at constant pressure of 30’’Hg.

(a) (b) (c)

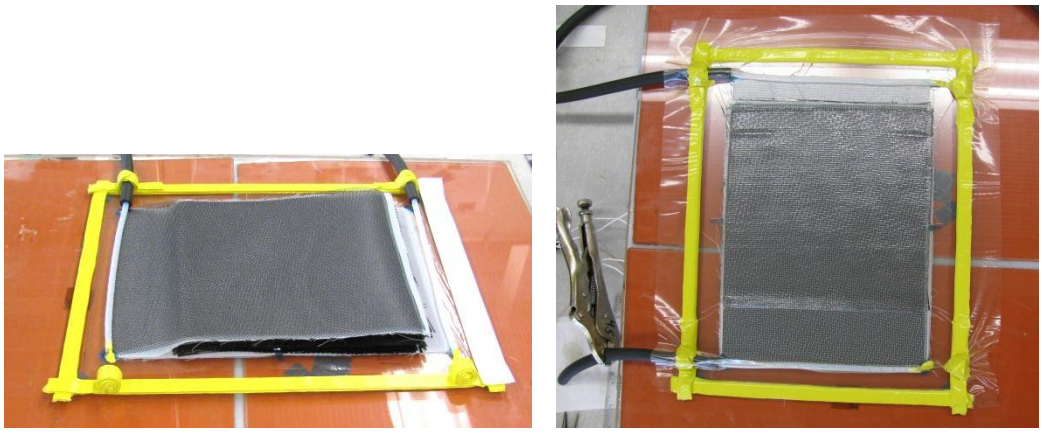

(d) (e)

Figure 2.4 (a) Bottom plain T300 fabrics stack (b) Fuzzy Titanium foil (c) After putting the fTi in the layup (d) Layup finished (e) After the first vacuum

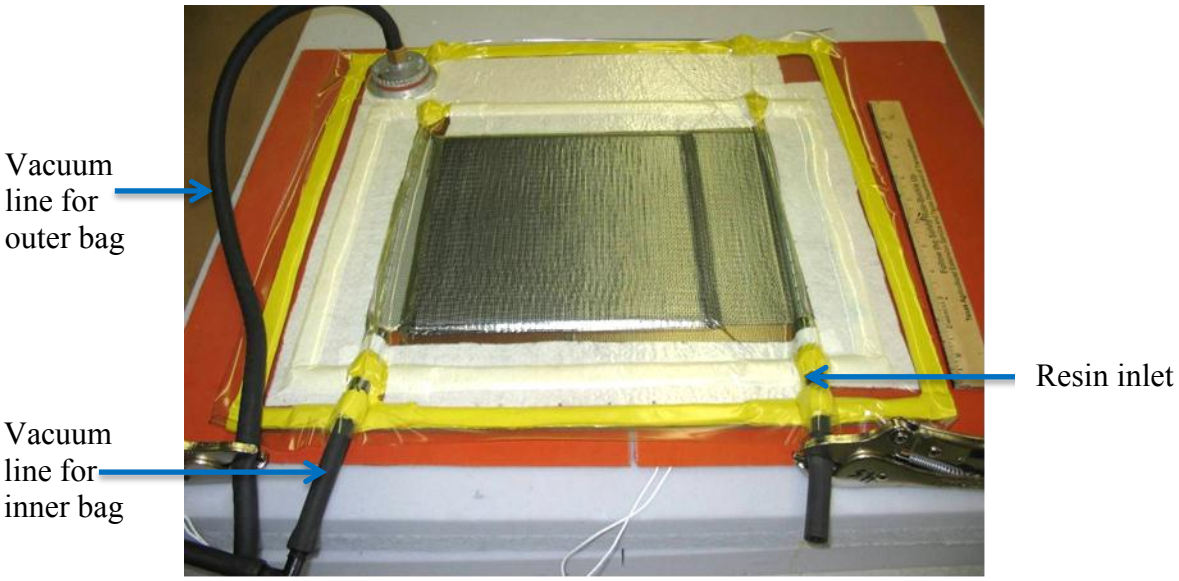

Figure 2.5 An example of the fabrication setup after resin infusion

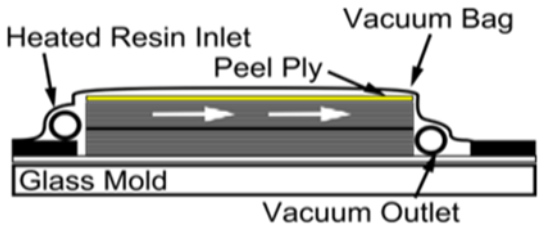

Figure 2.6 Schematic cross-section of VARTM layup

Table 2.1 Summary of the FF/Ti and FF/fTi panel properties

	FF/Ti	FF/fTi
Panel layup	$[0]_8$/FF/Ti/FF/$[0]_8$	$[0]_8$/FF/fTi/FF/$[0]_8$
Final panel mass (g)	212.29	283.63
Fiber + CNT Mass (g)	118.15	139.63
Plain fiber mass (g)	104.15	122.2
Ti mass (g)	17.62	45.75
Resin Mass (g)	94.14	98.25
Fiber density (g/cm^3)	1.76	1.76
Resin density (g/cm^3)	1.2	1.2
Fiber Volume (cm^3)	67.13	79.33
Resin Volume (cm^3)	78.45	81.88
Fiber mass Fraction (%)	56.0	49.23
Fiber volume fraction (%)	46.11	49.21

3 CHARACTERIZATION EXPERIMENTS

3.1 Double Cantilever Beam (DCB) Test

ASTM Standard D 5528-01 guidance is used to prepare Double Cantilever Beam specimens to estimate Mode I strain energy release rate. There are three data reduction methods for calculating G_I values proposed in this standard which are (a) the modified beam theory, (b) the compliance calibration method and (c) modified compliance calibration method. Of the above methods, the modified beam theory yields the most conservative values and it is adopted here [15]. Mode I interlaminar fracture toughness, G_I, was calculated as follows:

$$G_I = \frac{3P\delta}{2b(a + |\Delta|)}$$

where

P = load,

δ = load point displacement,

b = specimen width,

a = delamination length,

Δ = correction factor which may be determined experimentally by generating a least squares plot of the cube root of compliance C as a function of delamination length,

C = compliance, the ratio of the opening displacement to the corresponding applied load [15].

3.2 Test Specimen Preparation

As recommended by the ASTM Test Method D 5528 – 01, the specimen dimensions were kept at least 125 mm long and from 20 to 25 mm wide [15].

3.2.1 IM7 carbon fabric and epoxy matrix

There are two specimens cut from the fabricated composite panels of length 7.5 inches or 190.5 mm tested. The labels IM7_AM_DCB_1 and IM7_AM_DCB_2 respectively represent the DCB specimens with and without fuzzy T650 fabric in the mid-layer. Relevant details are presented in Table 3.1.

Table 3.1 IM7_AM_DCB Specimens Details

Name	**IM7_AM_DCB_1**	**IM7_AM_DCB_2**
Layup	$[90/0/90/0/90/0/90/0/90/0_{CNT}]_s$	$[90/0/90/0/90/0/90/0/90/0]_s$
Matrix	EPON 862/W	EPON 862/W
Fabric layers/type	14 x IM7 4-harness satin	16 x IM7 4-harness satin
Fuzzy Fabric layers/type	2 x T-650 8-harness satin	None
Average Thickness	5.757 mm	4.817 mm
Loading Rate	3 mm/min	3 mm/min
Initial crack length	47.7 mm	57.4 mm

Two piano hinge loading tabs of nominal size of 25 mm and 50 mm were adhesively pasted to the outer faces of the specimens at the cracked end. More details of hinges bonding process will be shown in section 3.2.3. One of the edge of the specimen was painted while to improve visibility of the crack tip. To measure the crack length, a self-adhesive scaling label of 6 cm long was applied to the painted edge of the specimen, starting at the crack initiation point. Then, the specimen is pinned to the test frame. Figure 3.1 shows a schematic view of the double cantilever beam test specimen.

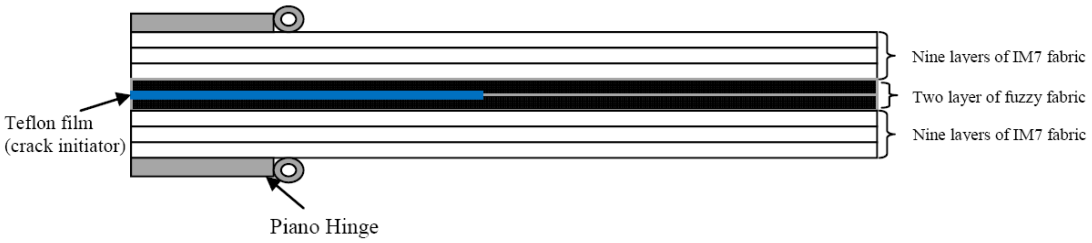

Figure 3.1 Schematic of IM7_AM_DCB_1 specimens

3.2.2 T650 carbon fabric and Epoxy matrix

Details of the two panels fabricated for this series are summarized in Table 3.2. T650_AM_FF denotes the panel that contains two layers of fuzzy fabrics in the center. Four specimens were cut from this panel. Two were tested at room temperature (RT) 25^{o}C, and the other two were tested at 110^{o}C, high temperature (HT). The panel named

T650_AM does not contain fuzzy fabric in its layup. Five specimens were cut from this panel. However, only three were tested, two at RT and one at HT. Detailed descriptions for hinge bonding process for RT-DCB and HT-DCB specimens will be mentioned in section 3.2.3.

Table 3.2 Summary of two panels fabricated for T650/EPON 862 series

Panel ID	T650_AM_FF	T650_AM
Resin Type	EPON 862/W	EPON 862/W
Total Layer Count	16	16
Fuzzy Fabric Layers/Type	2 x T-650 8-harness satin	none
Plain Fabric Layers/Type	14 x T-650 8-harness satin	16 x T-650 8-harness satin
Panel Size	6"x 6"	6"x 6"
Number of Specimens	4	5
RT DCB	2	2
HT DCB	2	1

3.2.3 T300 plain weave carbon fabric, Ti foil and epoxy matrix

The specimens were cut from the two T300/Ti panels, named and assigned DCB testing at either room temperature or elevated temperature (110^{o}C). Figure 3.2 (a) and (b) show the specimens' positions in relation to panels with and without fuzzy Titanium foil respectively. The specimens' ID tell the composite series name, where it was

fabricated, for example, T300_AM_FF/Ti_1 indicates that the specimen number is 1 and it is cut from the T300_FF/Ti panel fabricated at Texas A&M. Table 3.3 shows ID and test assignment for each specimen. The tested specimens' width, thickness and initial crack length data of are reported in Table 3.4.

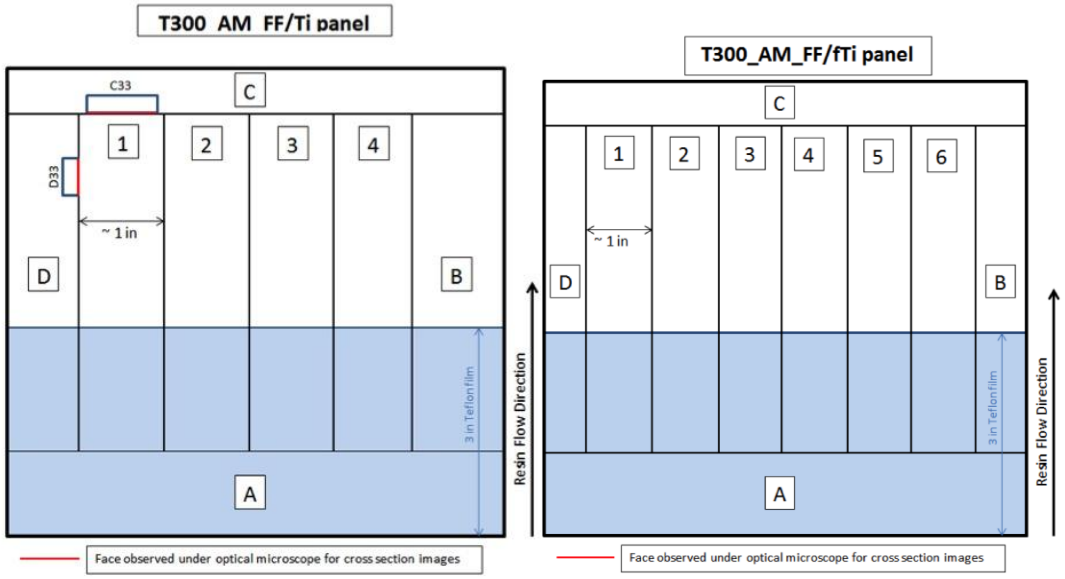

(a) (b)

Figure 3.2 Schematic of Ti-T300-PMC panels cut for DCB testing and cross-section imaging

Table 3.3 Specimens' ID and test assignment

Panel ID	Sample ID	Resin Type	RT DCB	HT DCB	DSC
T300_AM_FF/Ti	T300_AM_FF/Ti_1	EPON 862/W	x		
	T300_AM_FF/Ti_2*	EPON 862/W	x		
	T300_AM_FF/Ti_3*	EPON 862/W		x	
	T300_AM_FF/Ti_4	EPON 862/W		x	
T300_AM_FF/fTi	T300_AM_FF/fTi_1	EPON 862/W	x		
	T300_AM_FF/fTi_2*	EPON 862/W	x		
	T300_AM_FF/fTi_3*	EPON 862/W		x	x
	T300_AM_FF/fTi_4	EPON 862/W		x	
	T300_AM_FF/fTi_5 **	EPON 862/W			
	T300_AM_FF/fTi_6	EPON 862/W	x		

* indicates over-cured specimens during hinges attachment process

** indicates untested specimen

Table 3.4 Tested specimen dimensions and initial crack length

Sample ID	Width (mm)	Thickness (mm)	Initial crack length (mm)
T300_AM_FF/Ti_1	25.18	4.28	25.27
T300_AM_FF/Ti_2	25.15	4.34	35.60
T300_AM_FF/Ti_3	25.16	4.37	37.37
T300_AM_FF/Ti_4	25.17	4.35	34.01
T300_AM_FF/fTi_1	24.67	4.45	43.29
T300_AM_FF/fTi_2	25.20	4.47	43.21
T300_AM_FF/fTi_3	25.28	4.51	44.44
T300_AM_FF/fTi_4	24.11	4.49	43.91
T300_AM_FF/fTi_6	25.26	4.45	50.93

Before attaching hinges to the specimens, their edges were polished. Hinges attachment process is different for the room and high temperature DCB specimens. For each specimen, two piano hinge loading tabs (military rate, purchased from McMaster Carr) of 25 mm nominal width were cut and sanded in the back with 180 grit sand paper in two diagonal direction to improve attachment between specimen and hinges. The specimen was hold in place in a hinge attachment fixture so that the specimen's end with initial crack was of the same length as the hinge from the fixture. For room temperature testing, the Scotch Weld DP 460 adhesive was used. Its two parts were mixed and

stirred well. Then the two hinges were bonded to the outer faces of the specimens at the Teflon end. After that, the specimen was cured at 50^{o}C for at least four hours. One of the edges of the specimen was painted white and then cured at 60^{o}C for at least two hours to improve visibility of the crack tip. To measure the crack length, a self-adhesive scaling label of 6 cm long was applied to the painted edge of the specimen, starting at the crack initiation point. For high temperature testing, the adhesive used was M-bond GA-61. Part A of the adhesive was heated up to 60^{o}C before mixing with part B. It is important that adhesive, specimen and hinges were heat up before attaching. Then, the specimen with hinges adhered was cured at 125^{o}C for six hours and then 150^{o}C for two hours. After curing, the specimen was painted white on the cracks observing edge and cured again at 60^{o}C for more than two hours. A scale was hand-drawn on the white edge to help determine crack length during high temperature testing. This was done because the regular scaling label will not remain on the specimen at 110^{o}C during the test. It is noted that four samples were accidentally subjected to 200^{o}C instead of 150^{o}C for two hours during attachment curing. Thus additional experiments with DCS were undertaken to find the glass transition temperature to ensure that the composite properties did not changed considerably.

3.3 Test Procedures

3.3.1 Room temperature DCB test

After the specimen was prepared, it was loaded into the test frame by pinning the horizontal tabs to the vertical tabs of the piano hinges. The latter tabs were held by the

test frame grips. It was needed to make sure that the pins were removed easily under no load. If they could not slide freely, there might have existed twisting somewhere. This would affect the test results so it was important to get rid of these unexpected loads before testing. As suggested by ASTM Standard D 5528-01, an optical microscope or equivalent magnifying device should be used to observe the delamination front along the painted edge during the test [15]. It was best to videotape the test and observe the crack tip on a magnifying television screen when testing or replaying the video in case the crack length cannot be measure precisely the first time. The timing of the video correlates with that of the data collection pretty well. One crucial issue of this method is that the camera needed to be in line with the crack and specimen to improve the accuracy of measurement. Figures 3.3 and 3.4 show a schematic of room temperature double cantilever beam test setup done in this study and the DCB specimen being monitored by a digital camera during the test.

The testing machine used in this study was the Electro Mechanical 30kN Standard length MTS Insight servo-hydraulic connected to a monitoring computer. The Testwork program was used for data collection during the test. When the load was applied, the crosshead displacement was controlled at a rate of 3.0mm/min. The load was removed prior to any loading on the specimen. The specimen was loaded until the crack grew about 5 mm or there was a significant drop in loading. The crack tip's location was observed and recorded; then the specimen was unloaded before the next loading which would yield the next crack advancement. This process was repeated until the crack propagates to the end of the scaling label or the specimen failed. The test was

conducted under room temperature and conditions. Figure 3.5 (a) and (b) show the crack length monitored on the TV and an example of the Testwork program during the experiment.

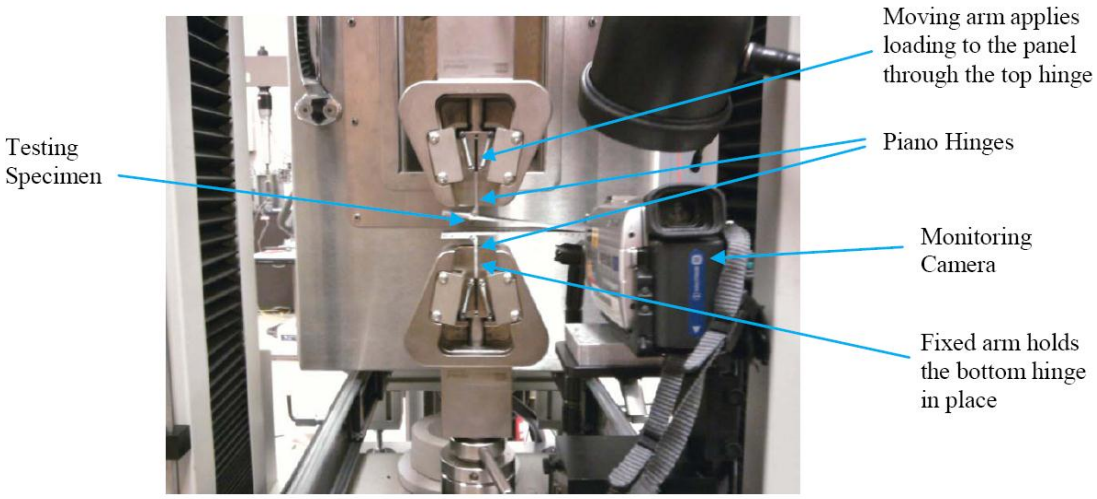

Figure 3.3 RT-DCB Test Setup

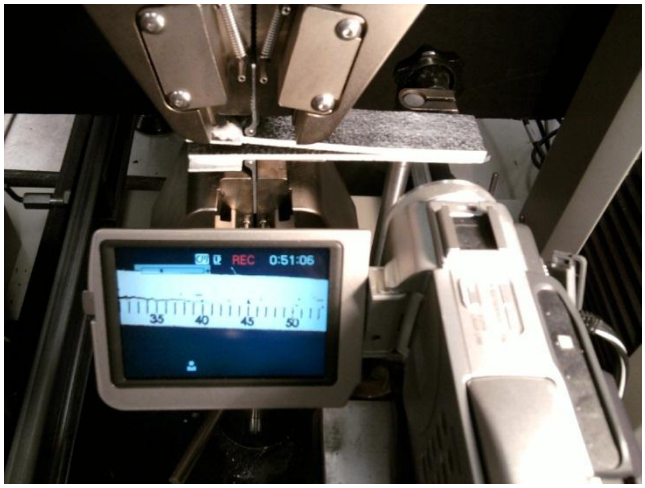

Figure 3.4 DCB Specimen during testing and digital camera recording the test

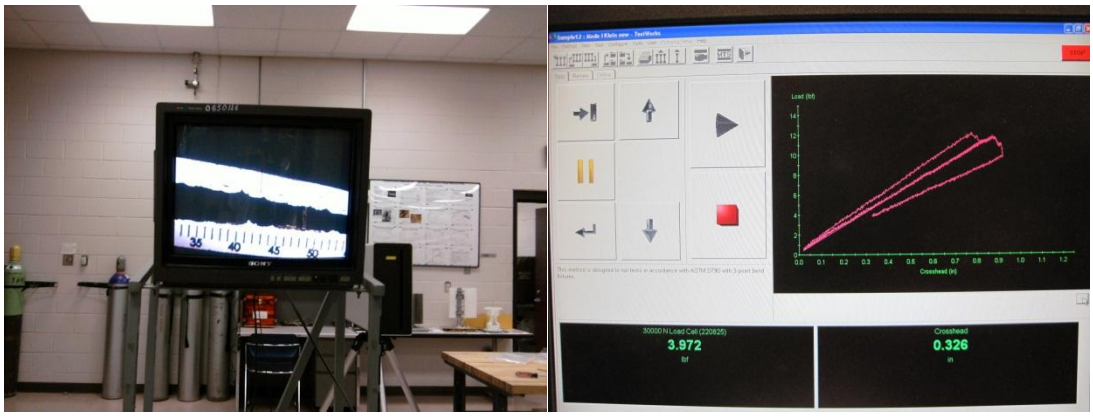

(a) (b)

Figure 3.5 (a) TV connected to camera monitoring crack opening

(b) Example of the load vs crosshead curve shown on the Testwork program

3.3.2 High temperature DCB test

High temperature DCB test was performed in a similar fashion, except in an oven at 110^{o}C. The oven was heated up to the testing temperature before the specimen was

loaded to the test frame. Then, the specimen was left in the oven for about half an hour, until stable state was reached. An example of high temperature DCB test setup is shown in Figure 3.6 below.

Figure 3.6 High temperature DCB test setup

3.4 Microscopy Observations

3.4.1 Scanning Electron Microscopy (SEM)

Scanning electron microscopy is conducted to study the fracture surfaces of the tested specimens. The instrument used in this work is a Field-Emission Scanning Electron Microscope; JEOL JSM-7500F.

3.4.2 Optical Microscopy (OM)

Optical microscopy is utilized to characterize the cross-sections of fabricated composite panels as well as fracture surfaces of tested DCB specimens.

3.4.3 Glass Transition Temperature characterizations

The glass transition temperature (T_g) of the composite is characterized using differential scanning calorimeter (DSC) and dynamic mechanical analyzer (DMA). The purpose of measuring T_g of the composites is to assist with determining the elevated temperature at which the mechanical characterizations will be carried out. This elevated temperature or high temperature (HT) should not exceed the onset of glass transition zone as observed from DSC and DMA curves.

3.5 Results and Discussions

3.5.1 Fracture toughness evaluation via DCB tests

3.5.1.1 IM7-Epoxy series

Figure 3.7 shows the load-displacement curve for IM7_AM_DCB_1 specimen. Due to elastic loading, the initial response of each specimen is linear. Then, when there is a major drop in loading due to cracking in the matrix, the loading process is paused for crack-tip observation followed by unloading and reloading process. The saw-toothed behavior of the load-displacement plots below can be commonly seen in woven fabric composites and characterized by the stick-slip response when a crack is reached to one point as the specimen is unloaded and reloaded until it is sufficiently loaded for the crack to propagate.

The least squares and R-curve plots for the two specimens are presented in Figures 3.8 to 3.11 and a comparison is depicted in Figure 3.12. It is noted that the fuzzy panel underwent higher loading which may be attributed to the higher resistance in fuzzy interface. Carbon nanotubes may also have enhanced the matrix strength locally

thus increasing load capacity. In addition, the spacing between loads where crack propagation occurs in the fuzzy specimen is bigger than that in the plain panel. In other words, the resistance to delamination growth in the sample is increased.

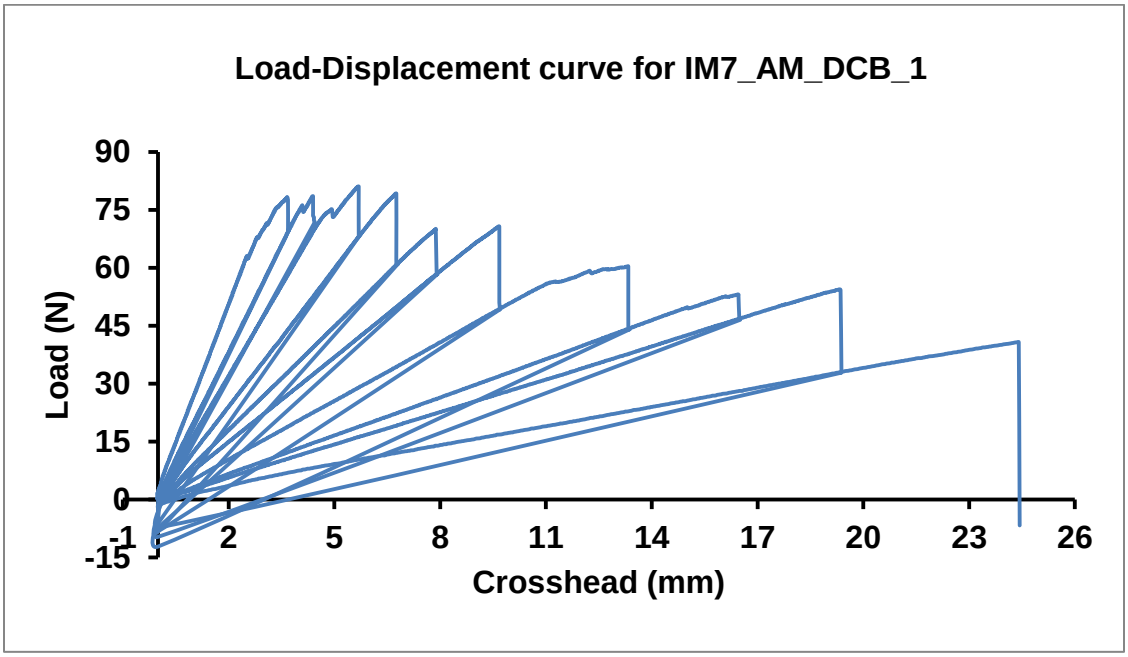

Figure 3.7 Load vs Displacement curve of the IM7_AM_DCB_1 specimen (with fuzzy fabric mid-layers)

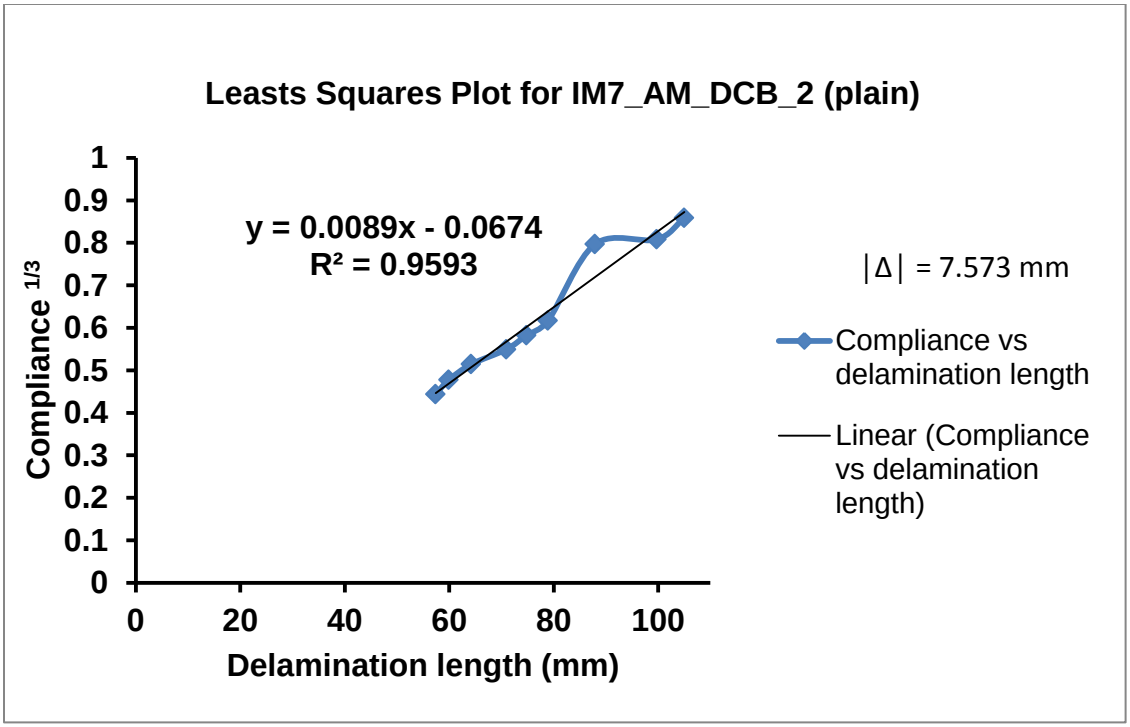

Figure 3.8 Least Squares plot for the IM7_AM_DCB_2 specimen

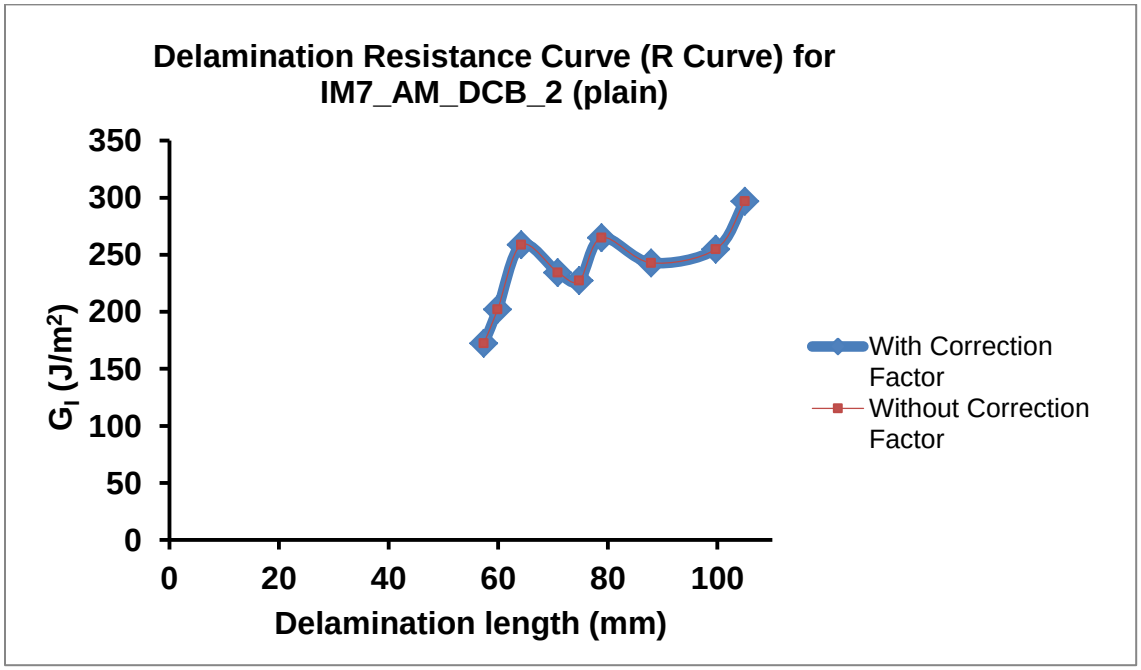

Figure 3.9 R-Curve plot of the IM7_AM_DCB_2 (plain) specimen

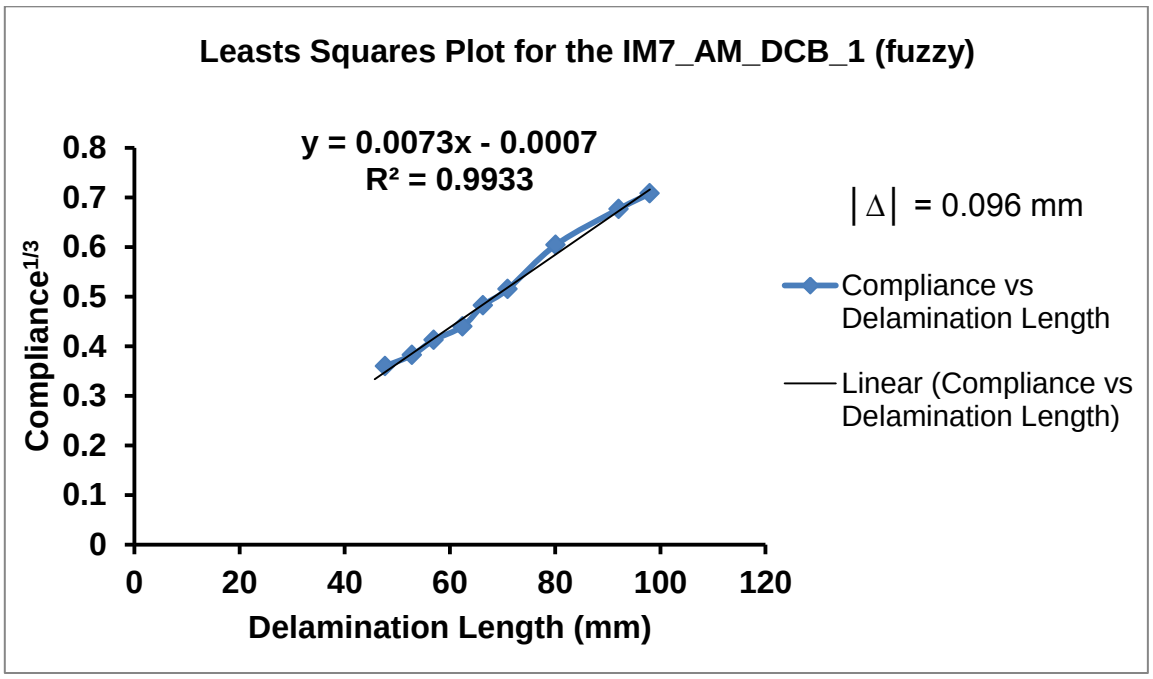

Figure 3.10 Least Squares plot for the IM7_AM_DCB_1 specimen

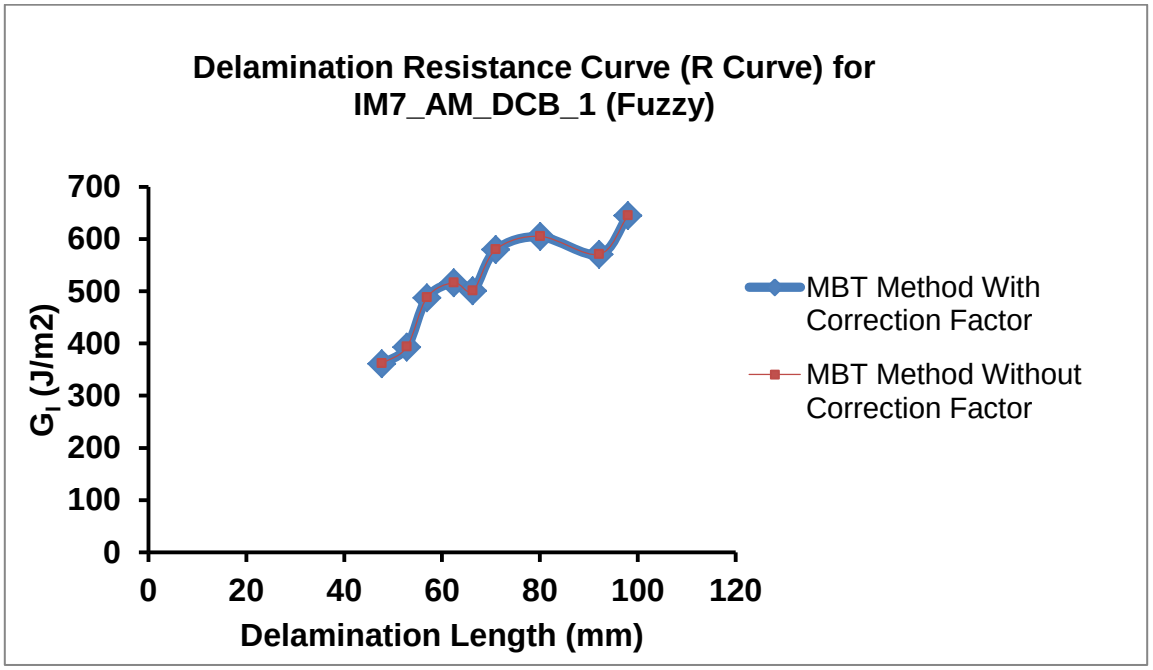

Figure 3.11 R-Curve plot of the IM7_AM_DCB_1 (fuzzy) specimen

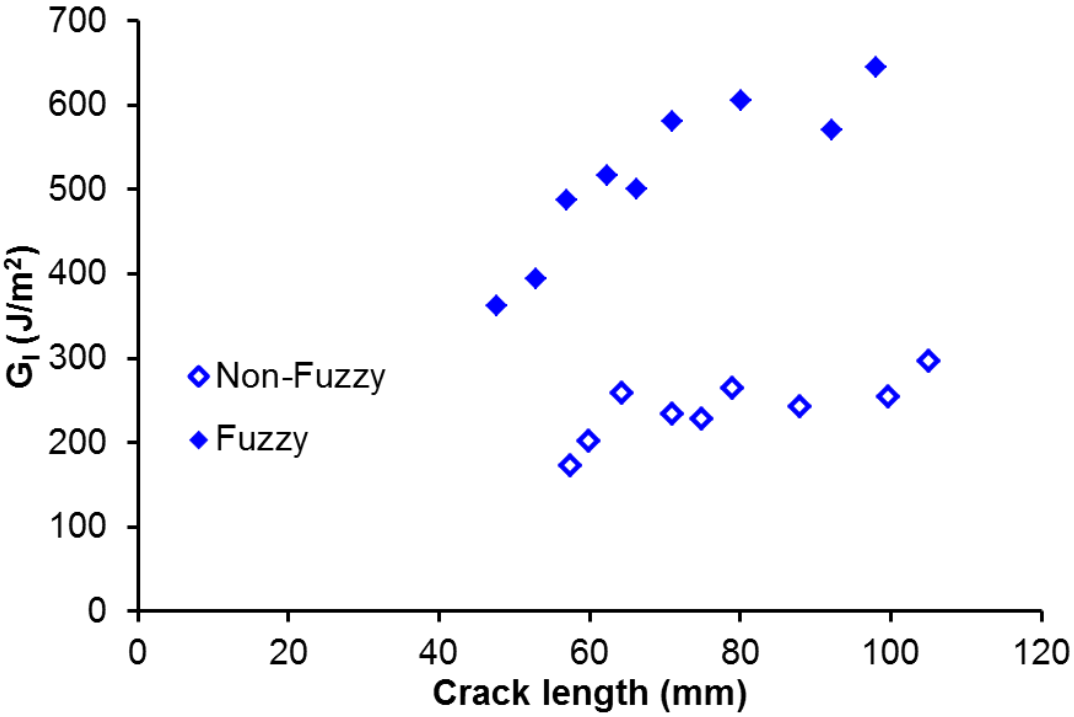

Figure 3.12 Mode I interlaminar fracture toughness of IM7 panels with and without fuzzy interface

3.5.1.2 T650_Epoxy series

Figure 3.13 summarizes the mode I interlaminar fracture toughness of the DCB specimens tested. Room temperature versus high temperature conditions and fuzzy versus non-fuzzy interface effects are highlighted. The data for room temperature is plotted in blue while high temperature data is depicted in red. Fuzzy interface results are show as filled data symbols and non-fuzzy interface data is plotted as unfilled symbols.

Assessing the non-fuzzy data series, fracture toughness values at elevated temperature are about three times higher than those at room temperature. However, for the fuzzy interface data, temperature seems to have no effect on fracture toughness values measured. In addition, it can be observed that at room temperature the fracture toughness of fuzzy interface is higher than that of non-fuzzy interface, up to 2.5 times. However, the single specimen with non-fuzzy interface tested at high temperature demonstrated higher fracture toughness in comparison to the room temperature values.

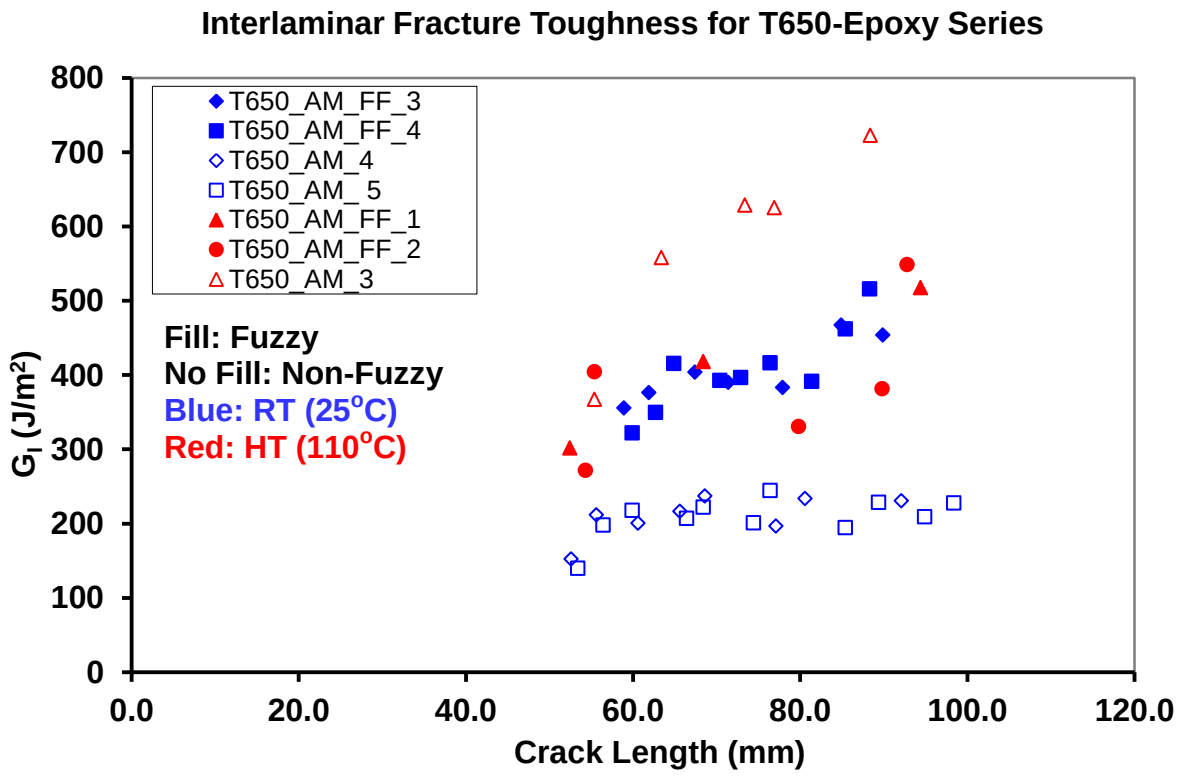

Figure 3.13 Mode I Interlaminar Fracture Toughness for T650-Epoxy specimens

3.5.1.3 T300/Ti_Epoxy series

The mode I fracture toughness values for the Ti T300-PMC series are presented in Figure 3.14. The data for room temperature are plotted in blue while the ones for high temperature are plotted in red. Fuzzy Titanium interface results are shown as filled data points and non-fuzzy Titanium interface data are plotted as unfilled points.

It should be noted that the G_I values here were calculated based on the assumption of uniform crack front across specimen width. For both panels, CNTs were present at the interface. However, the panel that contains fuzzy Titanium has CNTs at the interface come from both PMC and metal, the other panel, which has plain Titanium foil in its layup, has CNTs came from the PMC side solely. In general, as observed from Figure 3.14, metal interfaces that contain CNTs have higher fracture toughness. In addition, the FF/Ti specimens show temperature dependence, while the FF/fTi ones are little dependent of temperature.

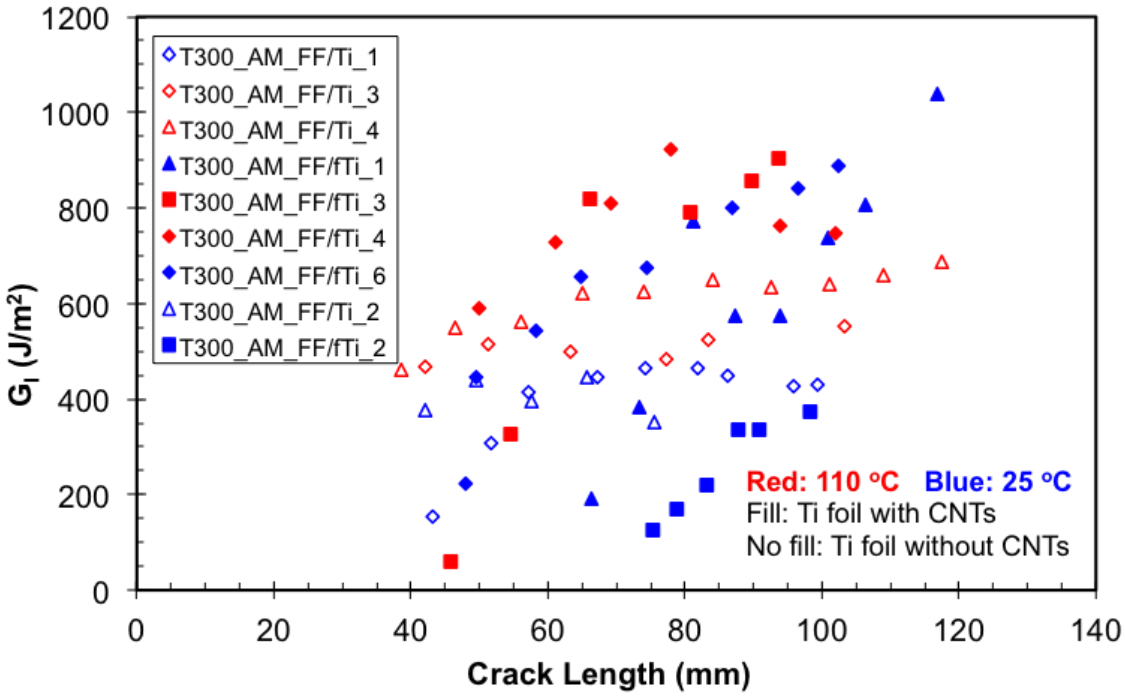

Figure 3.14 Mode I Fracture Toughness for T300/Ti_Epoxy Series

For ease of analysis, the room temperature data and high temperature data are plotted separately in Figure 3.15. Generally, fracture toughness for specimen that has fuzzy Ti interface was higher. However it is important to reflect on the quality of crack propagation in these tests; in some specimens, the crack jumped from one interface to another. For example, crack progressed from the interface between fuzzy fabric and fuzzy Ti to the interface between the fuzzy fabric and the layer of textile adjacent to it. More details of this can be seen in Appendix A where crack growth lengths are correlated to the total strain energy release rate calculated corresponding to each of them for each specimen tested in this series.

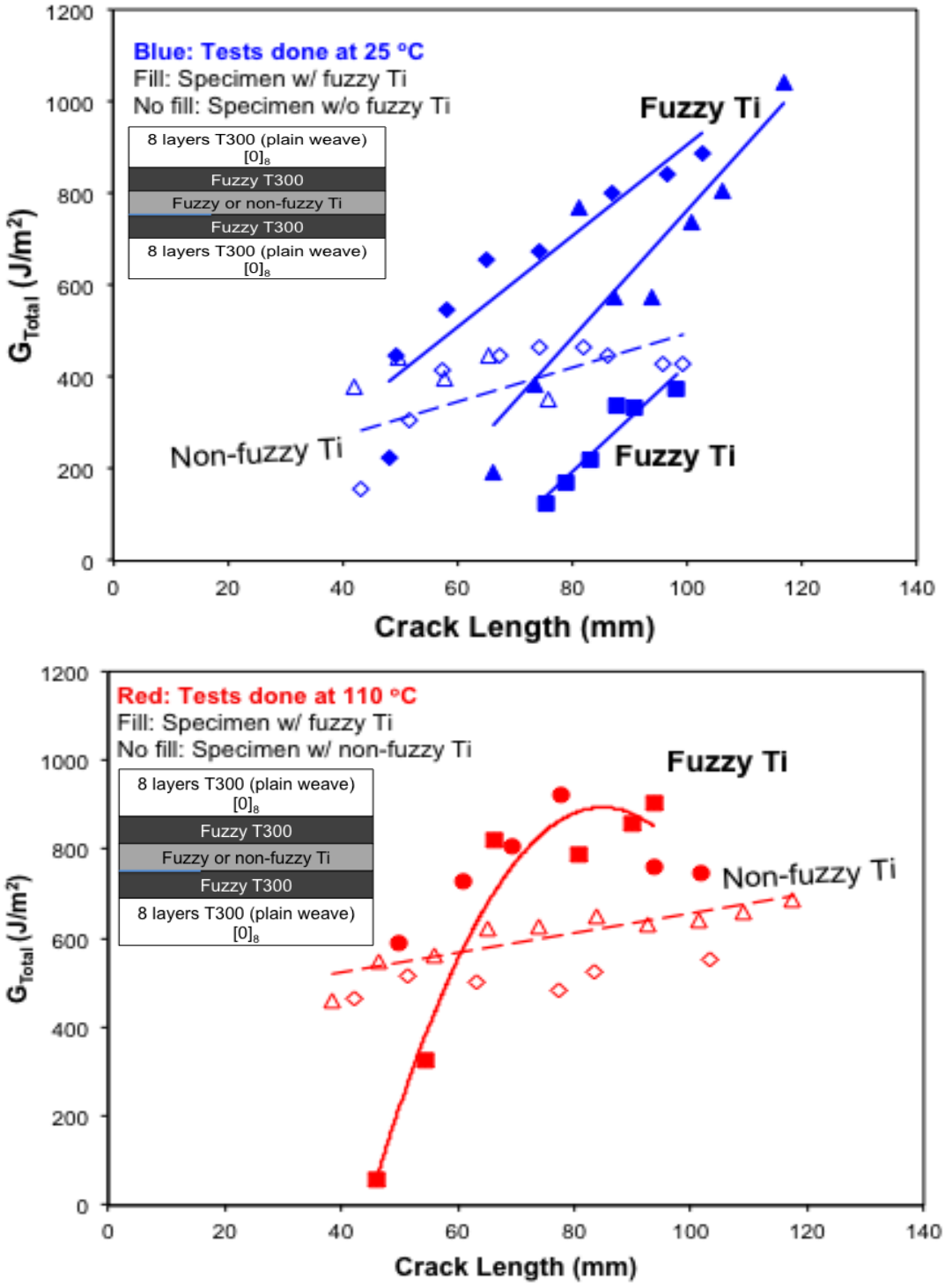

Figure 3.15 Fracture toughness of fuzzy versus non-fuzzy Ti interfaces

3.5.2 Cross-section microscopy observations

3.5.2.1 IM7_Epoxy panels

Below is a series of optical microscope cross-section images together with the schematic of the panel shown in Figure 3.16 and the cross-section sample for IM7_Epoxy panels shown in Figures 3.17 to 3.20.

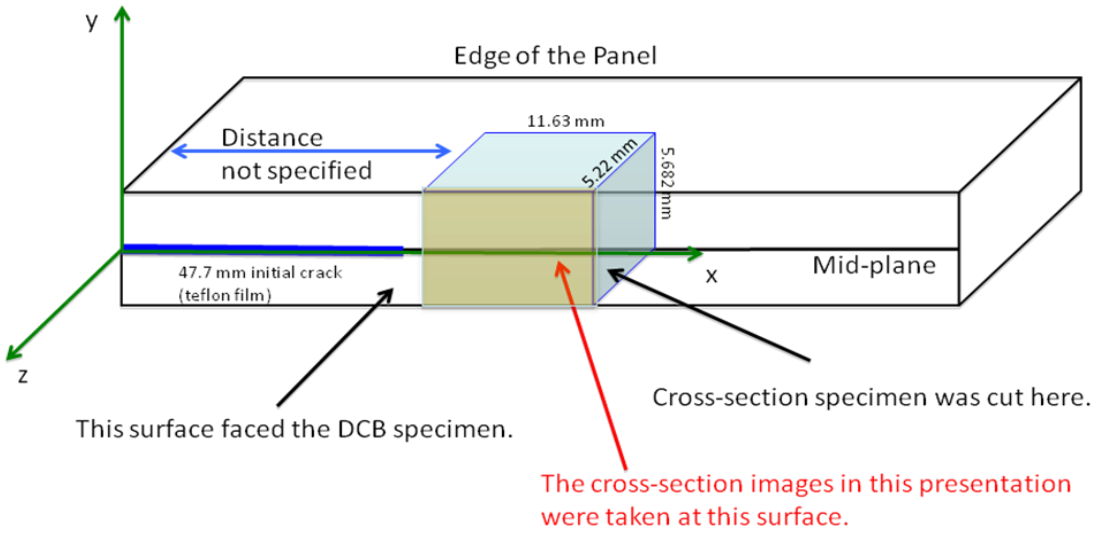

Figure 3.16 Schematic of the panel and the IM7_AM_DCB_1 Cross-section sample

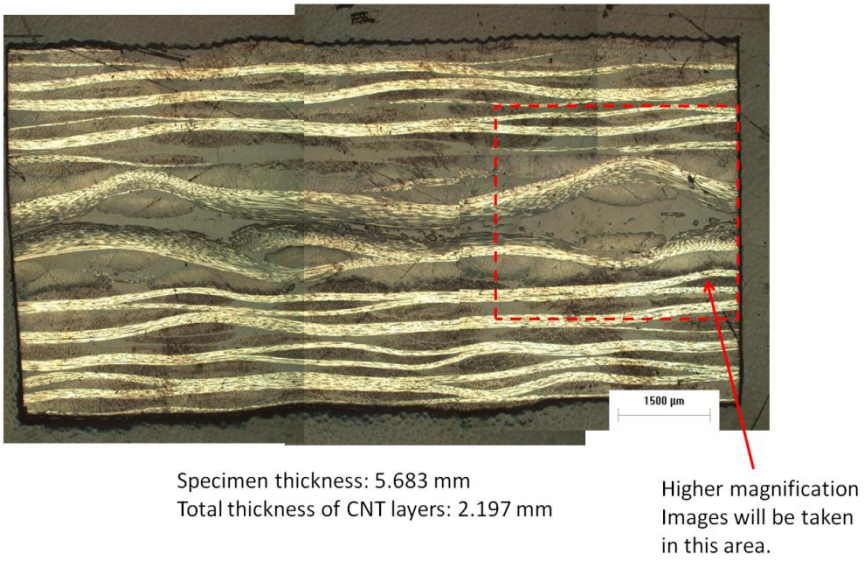

Figure 3.17 The IM7_AM_DCB_1 Specimen Cross-section

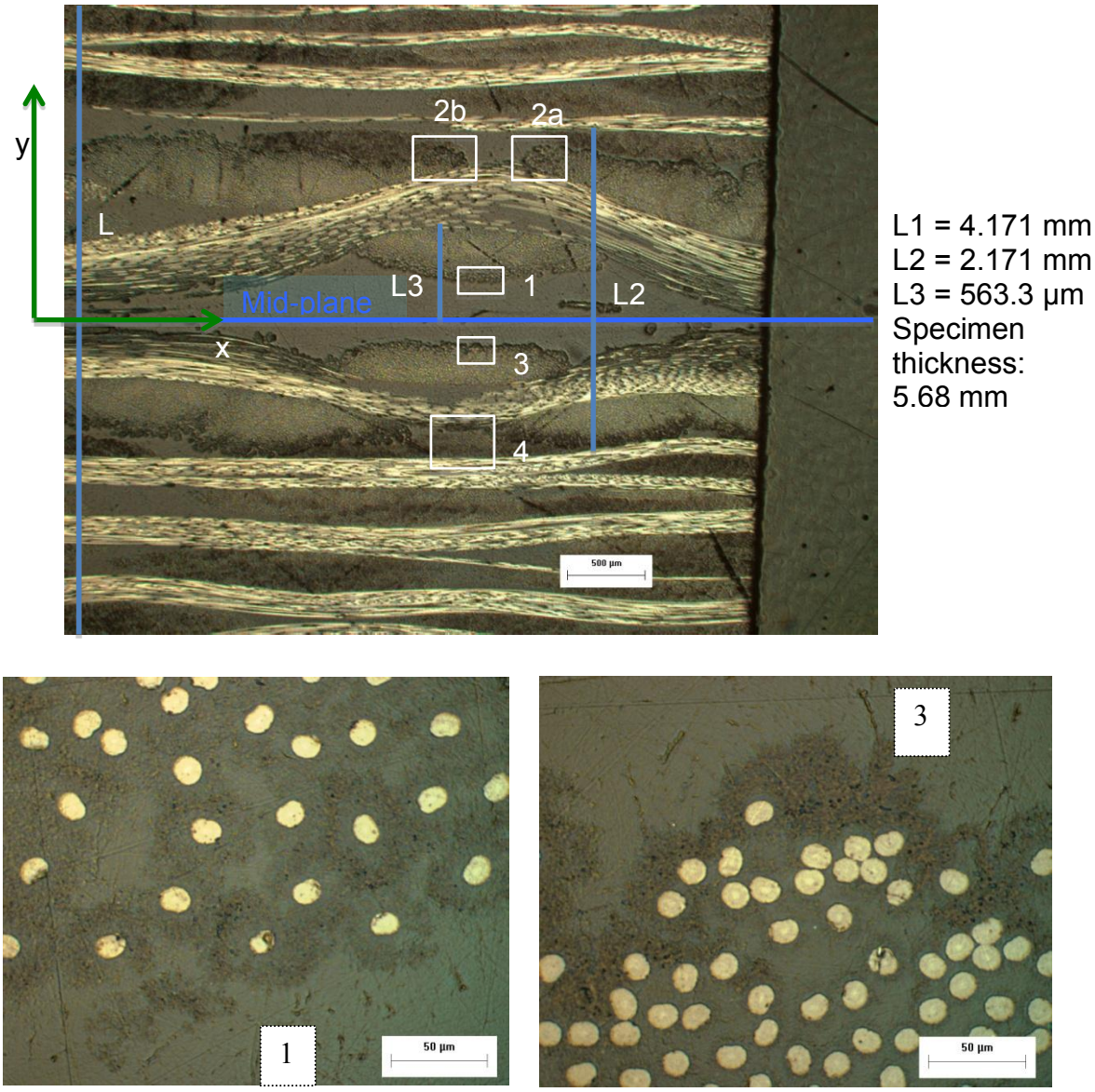

Figure 3.18 The IM7_AM_DCB_1 cross-section images taken at different magnifications and locations

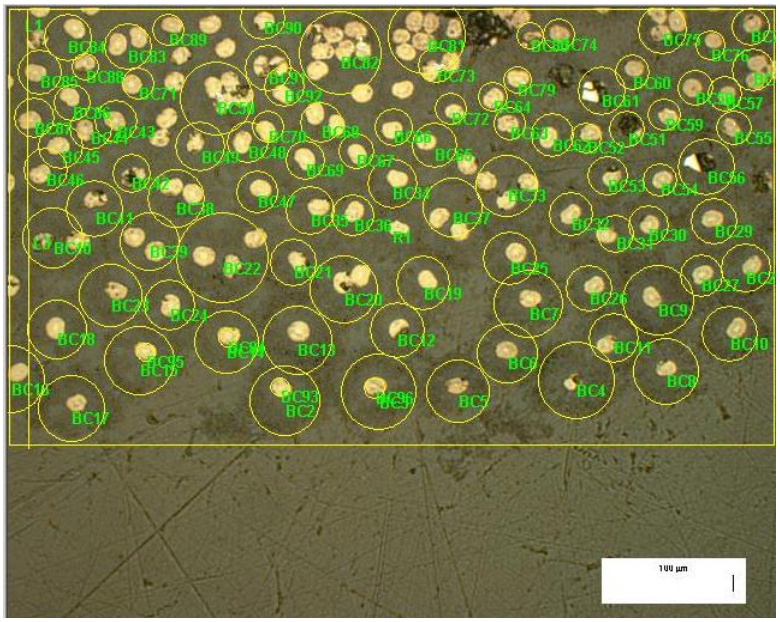

L1 = 373.13 µm

$A_{rectangle}$ = 238000 µm^2

$A_{circles}$ = 127968 µm^2

A_{fibers} = 23436 µm^2

A_{CNTs} = 104532 µm^2

A_{CNTs}/A_{rect} = 43.92%

Figure 3.19 Image at location 1 and %CNT measurements

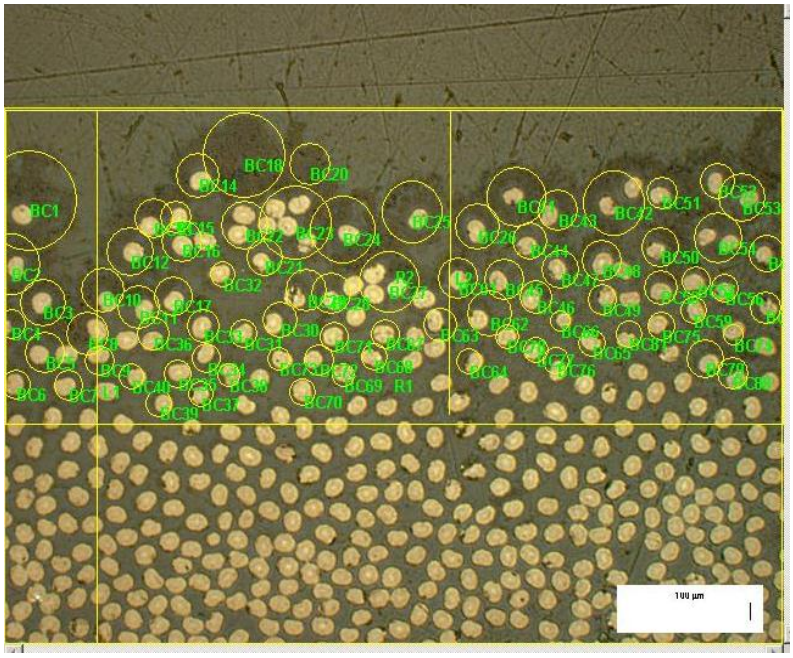

$L1 = 245.37\ \mu m$
$L2 = 428.89\ \mu m$
$A_{rectangle} = 163320\ \mu m^2$
$A_{circles} = 65991\ \mu m^2$
$A_{fibers} = 18167\ \mu m^2$
$A_{CNTs} = 47824\ \mu m^2$
$A_{CNTs}/A_{rect} = 29.28\%$

Figure 3.20 Image at location 3 and %CNT measurements

Carbon nanotubes grown on T650 fabric's surface are very visible in these specimens. From the above measurements, assume the existence percentage of CNT's in the panel is the same everywhere, it is calculated that the %CNT in the panel is roughly 1.84%. SEM images shown in Figure 3.21 help ensure the presence of CNTs in the fiber bundles at the interface.

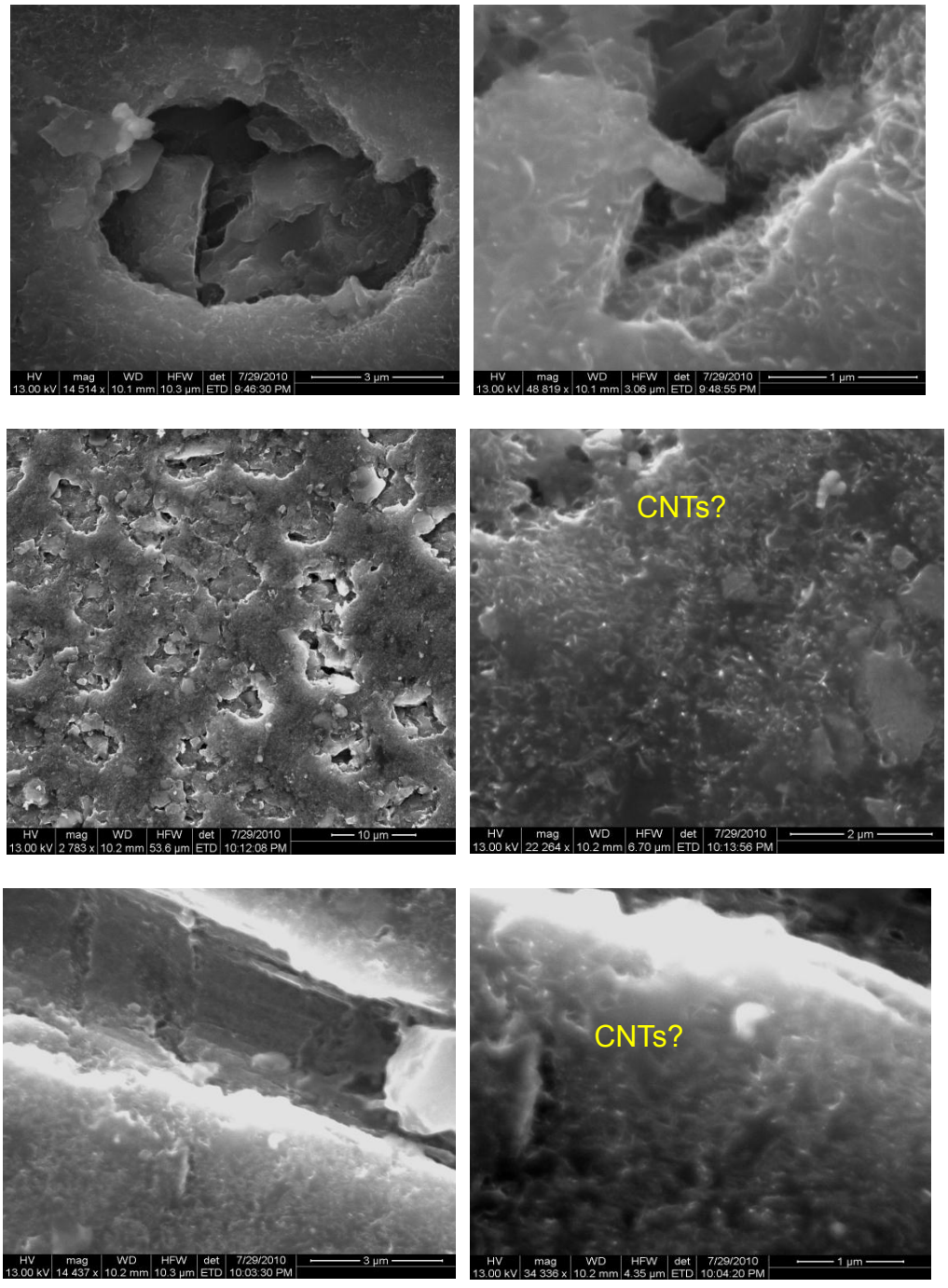

Figure 3.21 High magnification SEM images of cross-section

3.5.2.2 T300/Ti_Epoxy panels

Figure 3.22 shows SEM images of a fuzzy T300 fiber and CNTs bundles on its surface. The cross section images obtained from optical microscopy for the FF/Ti panel are shown on Figure 3.23. It can be pointed out that carbon nanotubes distribution in the panels appears to be non-uniform. They generally located on the surfaces of the fabric. Several other conclusions can be made here are that CNTs are not firmly attached to the fabric tows and tend to move to the panels' resin rich regions.

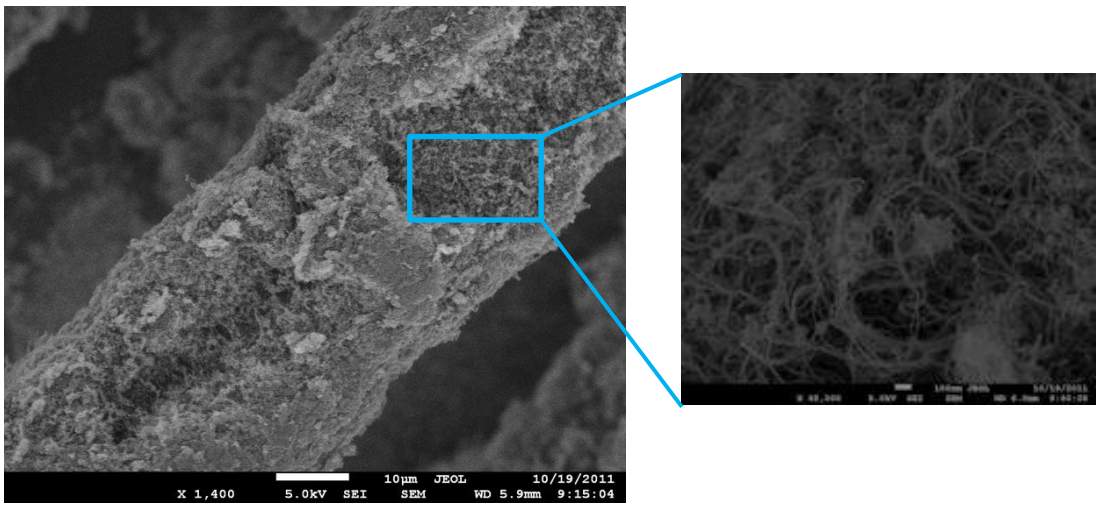

Figure 3.22 Fuzzy T300 fiber and CNTs bundle on its surface

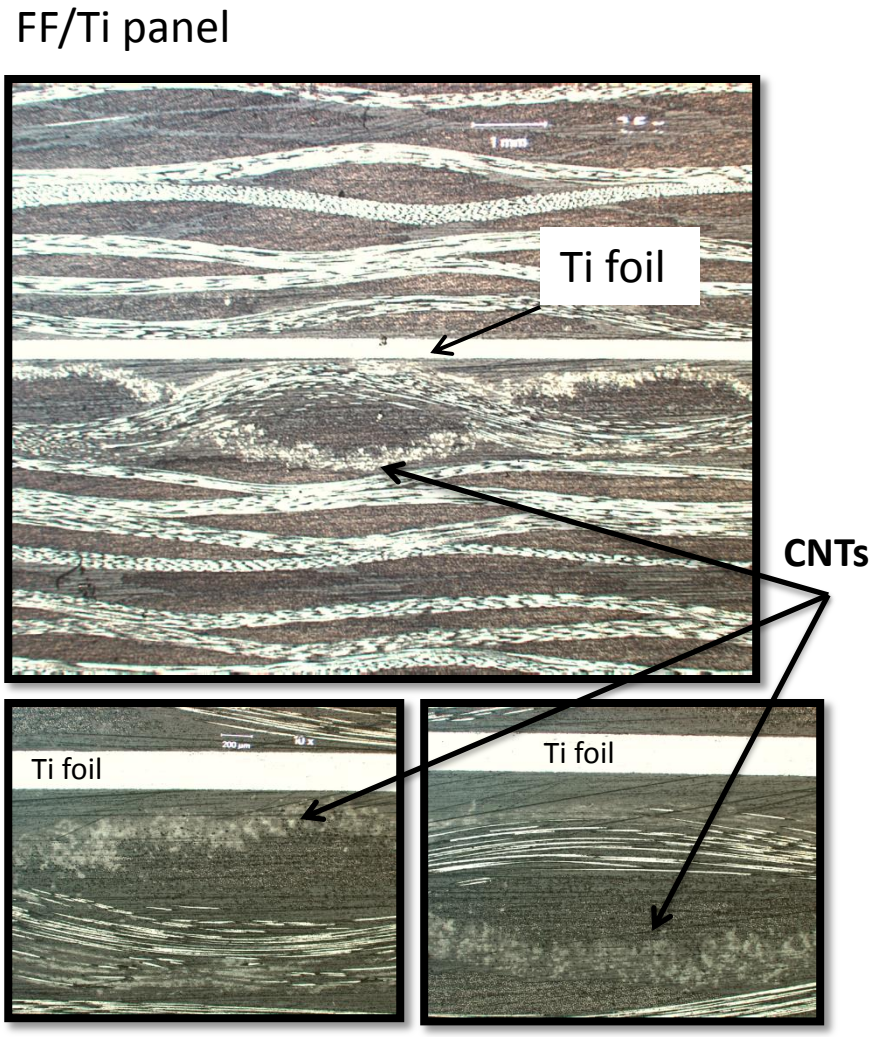

Figure 3.23 OM cross-section images of the FF/Ti panel

3.5.3 Fracture surface characterizations

3.5.3.1 IM7_Epoxy panels

Characterizations of the IM7_AM_DCB_1 specimen's fracture surface are shown on optical microscope and SEM images in Figures 3.24 to 3.26.

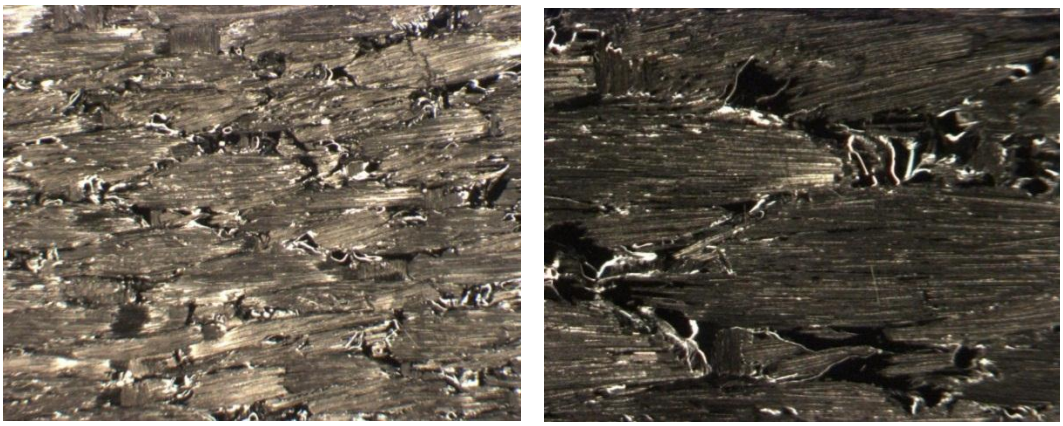

Figure 3.24 Fracture surface of IM7_AM_DCB_1 after DCB test at 0.5x and 1.4x under optical microscope

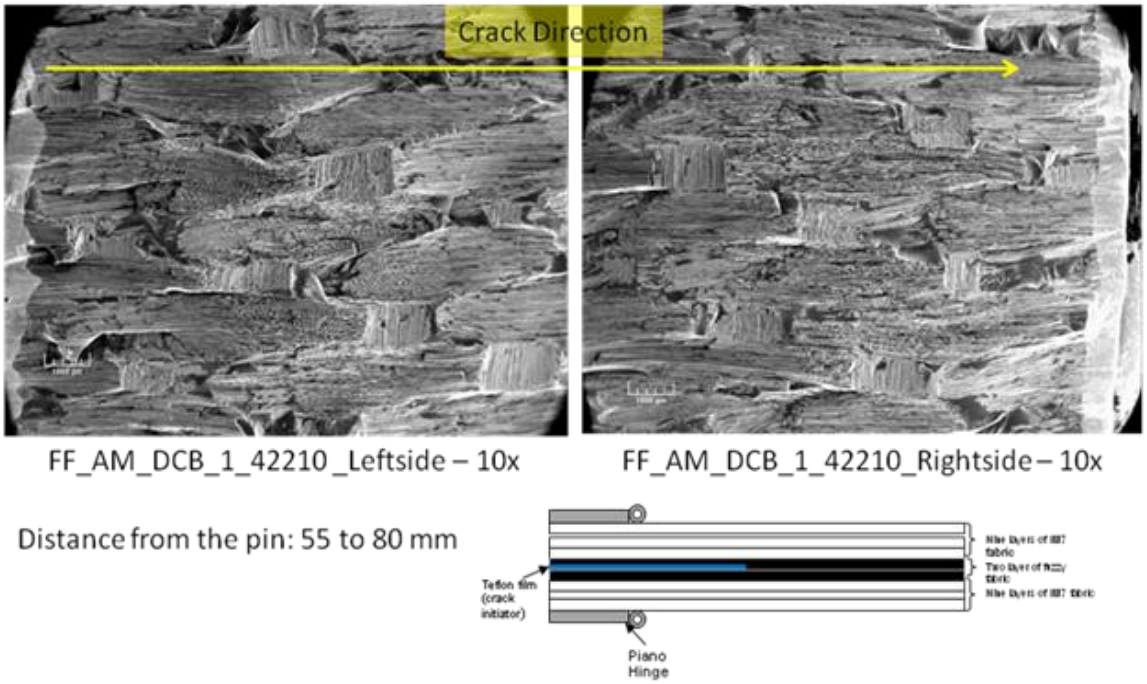

Figure 3.25 SEM fracture surface images of the IM7_AM_DCB_1 and schematic of the DCB Specimen

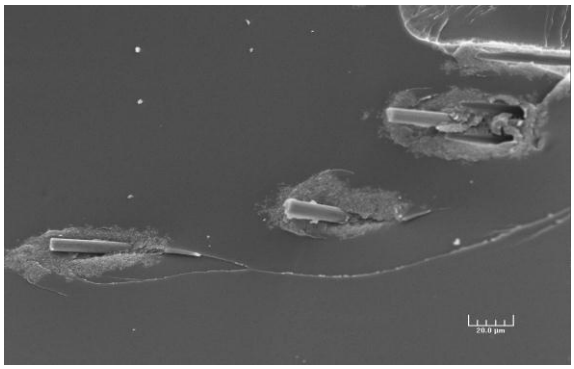

IM7_AM_DCB_1 at 500x

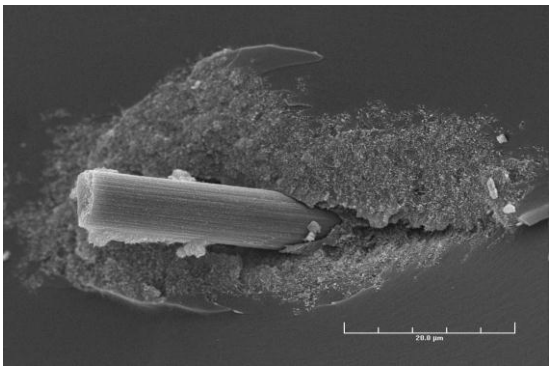

IM7_AM_DCB_1 at 2000x

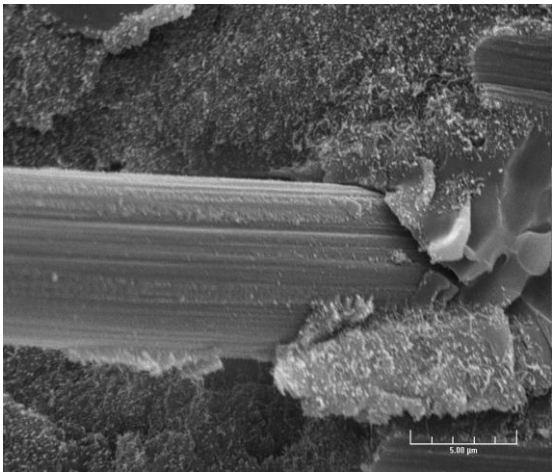

IM7_AM_DCB_1 at 5000x

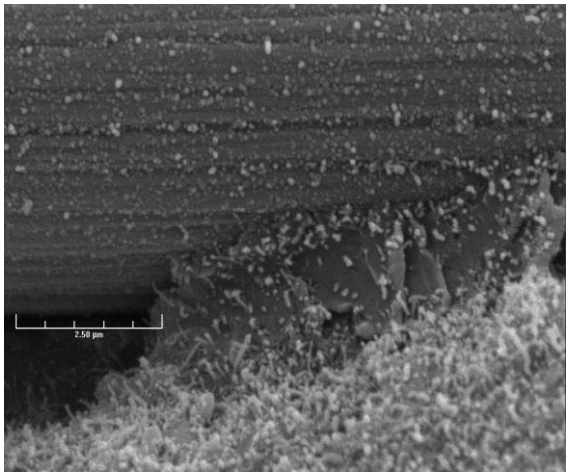

IM7_AM_DCB_1 at 13000x

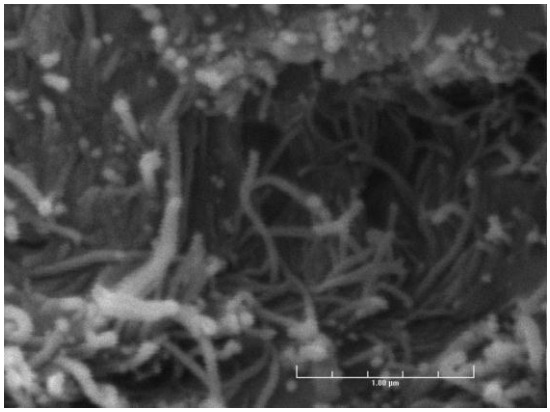

IM7_AM_DCB_1 at 40000x

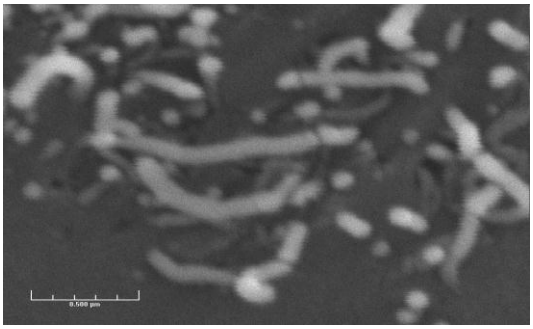

IM7_AM_DCB_1 CNT's

Figure 3.26 SEM Fracture surface images of the IM7_AM_DCB_1 specimen

3.5.3.2 T650_Epoxy panels

Figure 3.27 shows optical microscopic images of fracture surfaces for T650_Epoxy DCB specimens both for plain and fuzzy interfaces as well as RT and HT. For the plain interface, fracture surfaces for both RT and HT are dry, the drier surface occurs in the high temperature DCB specimen. This indicates that the specimen failed at the carbon fabric surface, which has more resistance than failure inside the resin rich region. This can help explain why higher fracture toughness is observed from the plain specimen tested at 110°C. Fracture surfaces for fuzzy interface tested at both RT and HT show failure in the matrix rather than in the fabrics.

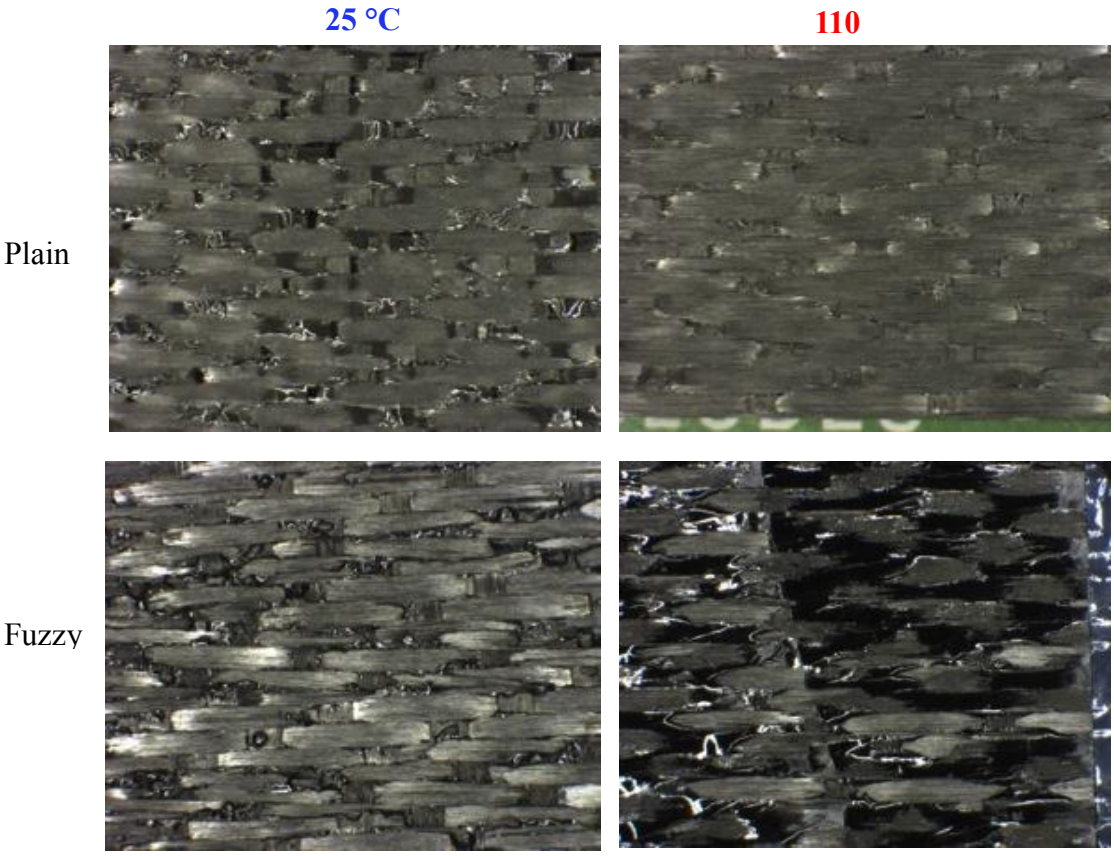

Figure 3.27 Optical microscopic images of fracture surface of T650_Epoxy specimens

4 COMPUTATIONAL ANALYSIS

4.1 Analytical Solutions for Strain Energy Release Rate Calculations

There are numerous methods reported in the literature to calculate the strain energy release rate for the asymmetric double cantilever beam (ADCB) model. The asymmetry is either due to the geometry or location of initial crack at a bi-material interface. Qiao et al [16] developed a deformable interface model to give a closed-form solution for the asymmetric double cantilever beam. However their solution is an approximation because this model considers the bonded part of the bilayer beam has infinite length. Bennati et al [17] proposed an enhanced beam theory model, which considers the deformable interface as a continuous distribution of elastic-brittle springs. This model uses interfacial stress as fundamental unknowns, thus, evaluations of different fracture modes can be achieved directly. Results from these methods are generally in good agreement with both experimental and finite element results. However, the aforementioned approaches are rather complicated. For this study, a simpler approach is considered where the analytical solution is derived from beam theory and the strain energy in bending of beams. Results are then compared to values computed using the closed-form solution proposed by Williams [18]. Williams' solution arrives from fracture mechanics, which can distinguish mode I and mode II strain energy release rates given asymmetric configurations.

4.1.1 The beam theory approach

The following derivation is for the asymmetric double cantilever beam (ADCB) shown in Figure 4.1. For displacement control loading situation, because of the asymmetric configuration, the reaction force at loading points P_1 and P_2 may not be the same. Thus, let the top arm be (1) and the bottom arm be (2) and assume displacement in each arm δ_1 and δ_2 respectively. Equilibrium of force equation reveals P_1 equals P_2.

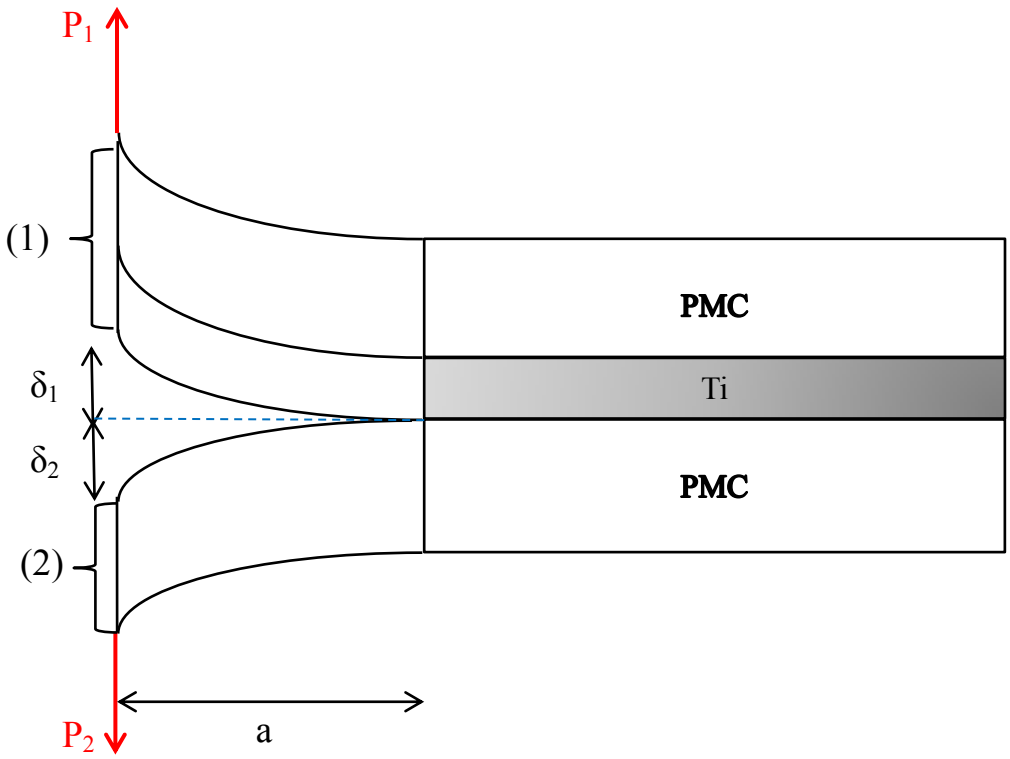

Figure 4.1 Schematic of ADCB beam in bending

From beam theory, deflection δ_1 can be calculated as

$$\delta_1 = \frac{\delta}{2} = \frac{P_1 a^3}{3E_1 I_1}$$

thus,
$$P_1 = \frac{3\delta_1 E_1 I_1}{a^3}$$

where
$$E_1 I_1 = E_{PMC} I_{PMC_{top}} + E_{Ti} I_{Ti_{top}}$$

with $I_{PMC_{top}}$ and $I_{Ti_{top}}$ are respectively the second moments of area of the PMC and Ti layers with respect to the top arm's neutral axis as shown in Figure 4.2. Calculations of $I_{PMC_{top}}$ and $I_{Ti_{top}}$ can be done using knowledge of mechanics of materials [19].

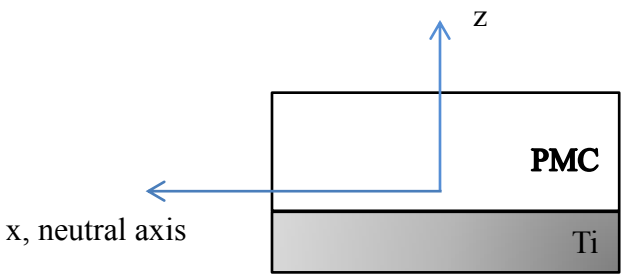

Figure 4.2 Schematic of cross-section of arm (1) and locations of its neutral axis

Similar formulas for δ_2 and P_2 can be easily obtained for arm (2). The strain energies stored in the two arms when subjected to bending are

$$U_1 = \frac{1}{2}\int_0^a \frac{M_1^2}{E_1 I_1}\,\mathrm{d}x \qquad \text{and} \qquad U_2 = \frac{1}{2}\int_0^a \frac{M_2^2}{E_2 I_2}\,\mathrm{d}x$$

where M_1 and M_2 are bending moments due to forces P_1 and P_2.

Thus, carrying out the integrations above gives the following formulas for U_1 and U_2.

$$U_1 = \frac{P_1^2 a^3}{6E_1 I_1} \qquad \text{or} \qquad U_1 = \frac{3\delta_1^2 E_1 I_1}{2a^3}$$

$$U_2 = \frac{P_2^2 a^3}{6E_2 I_2} \qquad \text{or} \qquad U_2 = \frac{3\delta_2^2 E_2 I_2}{2a^3}$$

By definition, the total strain energy U is the sum of U_1 and U_2. In addition, for constant displacement δ, the total strain energy release rate is defined as

$$G = -\frac{1}{B}\frac{\partial U}{\partial a} = \frac{1}{B}\left[\frac{\partial U_1}{\partial a} + \frac{\partial U_2}{\partial a}\right]$$

where B is the width of the specimen, $\dfrac{\partial U_1}{\partial a} = -\dfrac{9\delta_1^2 E_1 I_1}{2a^4}$ $\dfrac{\partial U_2}{\partial a} = -\dfrac{9\delta_2^2 E_2 I_2}{2a^4}$

Thus, the final formula for G is

$$G = \frac{1}{B}\frac{9}{2a^4}(\delta_1{}^2 E_1 I_1 + \delta_2{}^2 E_2 I_2)$$

The above formulas are coded in to Engineering Equations Solver (EES) software to calculate the total strain energy release rate as well as perform parametric studies. The detailed program and results can be found in Appendix B.

4.1.2 Fracture mechanics approach

Williams [18] proposed a solution to calculate mode I and mode II strain energy release rates separately for a beam of monolithic material under different loadings and geometrically asymmetric around the crack as illustrated in Figure 4.3. This closed-form solution is used to calculate the different modes of strain energy release rates as well as perform parametric studies with Engineering Equations Solver (EES) software. The detailed program and results can be found in Appendix C.

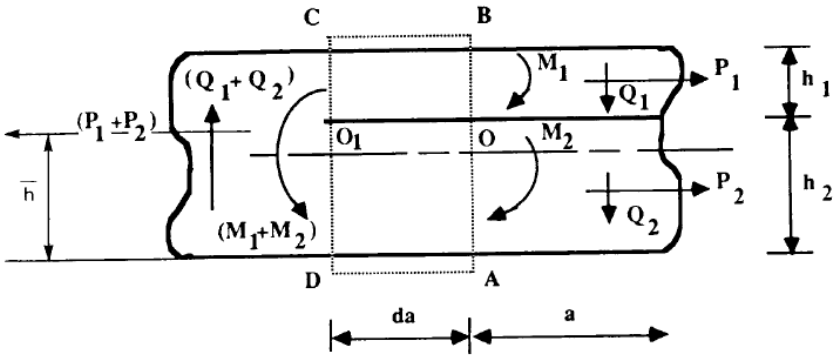

Figure 4.3 Schematic of loadings on a delamination [18]

G_I and G_{II} values calculated using Williams' model are expressed below [18]

$$G_I = \frac{a_{11}M_I^2}{BI}\frac{1+\psi}{16(1-\xi)^3} = \frac{a_{11}}{BI}\frac{(M_2-\psi M_1)^2}{16(1-\xi)^3(1+\psi)},$$

$$G_{II} = \frac{a_{11}M_{II}^2}{BI}\frac{3}{16}\frac{1-\xi}{\xi^2}(1+\psi) = \frac{a_{11}}{BI}\frac{3(1-\xi)(M_2+M_1)^2}{16\xi^2(1+\psi)},$$

where,

$$\psi = \frac{E_1 I_1}{E_2 I_2} \qquad \xi^3 = \frac{E_1 I_1}{EI} \qquad 1 - \xi^3 = \frac{E_2 I_2}{EI}$$

4.2 Virtual Crack Closure Technique in Finite Element Analysis

To model crack propagation in finite element analysis, several approaches utilized to date include employing the cohesive behavior and/or the virtual crack closure technique. When studying crack propagation in laminated composite materials, especially in the case where the crack is located at a bi-material interface, the delaminations usually have high mode-mixity. Thus, it is often of great interest to investigate the degree and effects of mode-mixity in different laminated composite layups subjected to loading schemes. The virtual crack closure technique has been widely used for this purpose. By using the mixed-mode fracture criterion in finite element analysis, energy release of separated modes can be computed.

The virtual crack closure technique is a method based on linear elastic fracture mechanics principles, therefore, suitable for brittle crack propagation problems. The main assumptions used in this technique are that the material behaves linear elastically; and that the energy required to advance a crack by a certain amount is the same as the energy required to close the crack by the exact same amount. This concept is illustrated in Figure 4.4 where crack is extended and closed between nodes i and j.

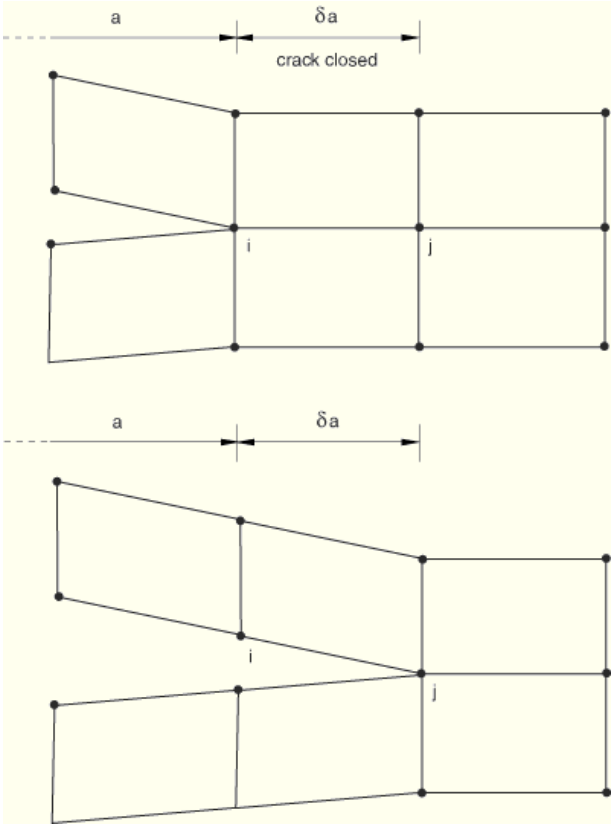

Figure 4.4 Illustration of VCCT concept where energy required to release a crack is the same as the energy needed to close it [20]

The total strain energy release rate G_T is composed of three independent components. First, the mode I, so-called the opening mode, strain energy release rate, G_I, is caused by interlaminar tension or usually the loads perpendicular to the crack plane. The second component, G_{II}, is due to sliding shear loads that are parallel to the crack plane and perpendicular to crack front. The third mode, or tearing mode, strain energy release rate G_{III}, is because of interlaminar scissoring shear, which is parallel to both the

crack plane and crack front. Illustrations of the above described three different fracture modes are shown in Figure 4.5. A simple demonstration for calculation of pure G_I is shown in Figure 4.6. In this case, only opening (vertical) force is applied.

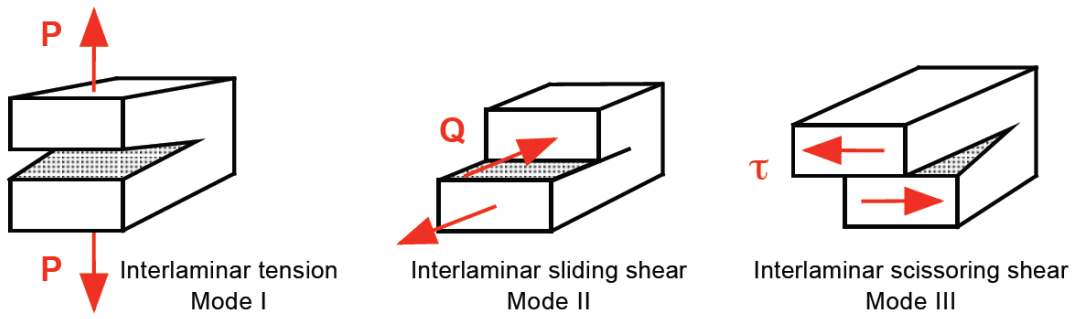

Figure 4.5 3 modes of fractures [21]

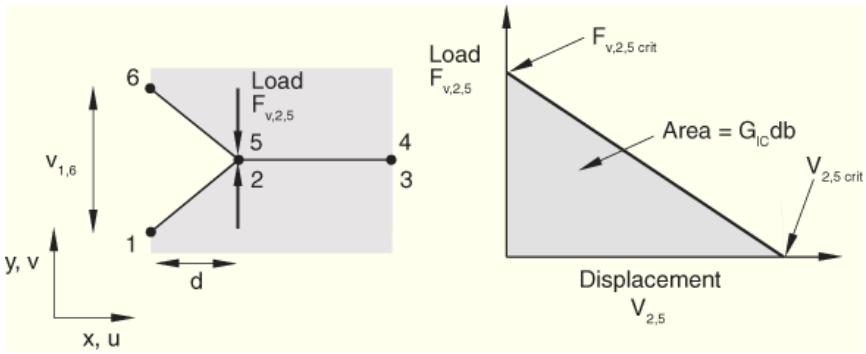

Figure 4.6 Demonstration of G_I calculation [20]

$$G_I = \frac{1}{2}\frac{v_{1,6}F_{v,2,5}}{bd}$$

In the equation to calculate mode I strain energy release rate above, b is the width and d is the length of the elements at delamination front; $v_{1,6}$ is the vertical opening

displacement between node 1 and node 6; $F_{v,2,5}$ is the vertical opening force at nodes 2 and 5. This method can be straight-forwardly extended to a full three-dimensional model for all three modes. Figure 4.7 shows a finite element mesh that consists of 8-node solid elements and the use of VCCT to calculate G_I, G_{II}, and G_{III}.

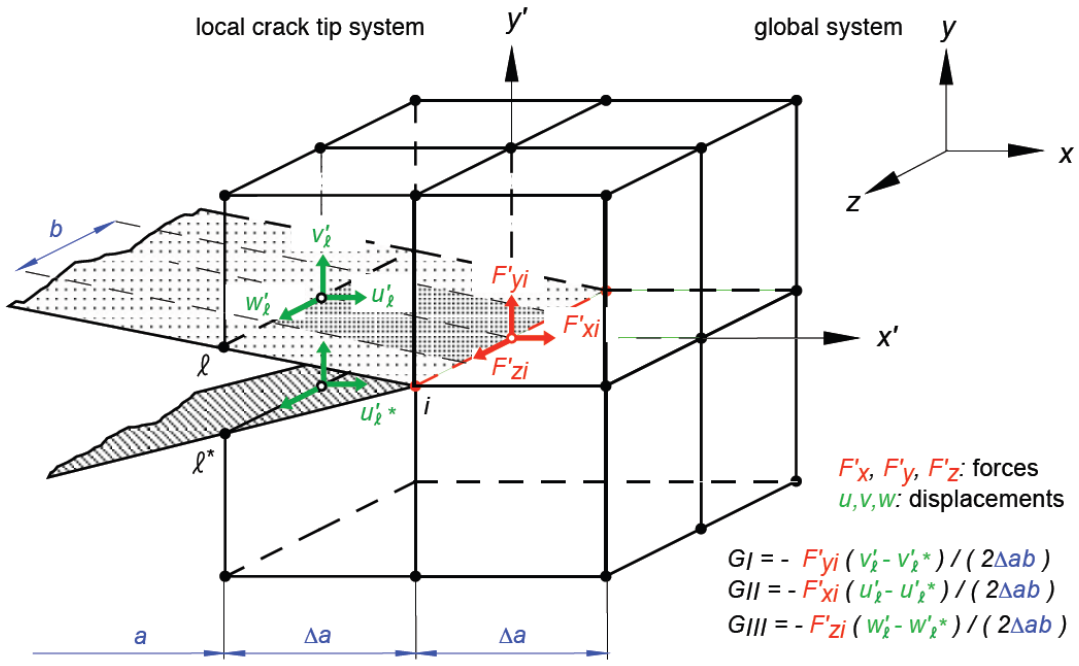

Figure 4.7 Calculations of strain energy release rates using VCCT for 8-node solid elements [21]

Each material has specific values of critical strain energy release rates of three different modes. The crack is released when the calculated total strain energy release

rate exceeds critical fracture toughness, G_c. There are different fracture criterions suggested to calculate G_c value. For example, the Benzeggah-Kenane criterion [22] suggested the following formula

$$G_c = G_{Ic} + (G_{IIc} - G_{Ic}) \cdot \left(\frac{G_{II}}{G_T} \right)^{\eta},$$

where G_{Ic} and G_{IIc} are fracture toughness values determined from experiments; and $G_T = G_I + G_{II} + G_{III}$. The Reeder criterion [23], based on the Benzeggah-Kenane criterion, also takes into account the effect of scissoring shear mode, and leads to the following expression,

$$G_c = G_{Ic} + (G_{IIc} - G_{Ic}) \cdot \left(\frac{G_{II} + G_{III}}{G_T} \right)^{\eta} + (G_{IIIc} - G_{IIc}) \cdot \frac{G_{III}}{G_{II} + G_{III}} \cdot \left(\frac{G_{II} + G_{III}}{G_T} \right)^{\eta}$$

4.3 Finite Element Analysis of Asymmetric Double Cantilever Beam Model

In order to help interpret experimental data and have a better understanding of the interface between metal and polymer matrix composite, a finite element model is developed for the T300-Ti composite configurations. It is based on the in-house finite element code called Beta developed by Whitcomb and the Virtual Crack Closure Technique (VCCT) implemented in a post-processor to calculate strain energy release rates [24].

4.3.1 Material properties

The homogenized orthotropic properties of plain weave T300 composite lamina are obtained from a meso-scale finite element model of Whitcomb [24]. Input parameters include material properties for T300 fiber and EPON 862 epoxy. The volume fraction of fibers in a tow is assumed to be 81% and the overall fiber volume fraction is 57.15%. Table 4.1 shows the effective properties of the textile layers obtained from this FEA model.

Table 4.1. Effective properties of plain weave T300 carbon fabric and EPON 862 composite

Plain Weave T300/EPON 862		
E_1 = 56.75 GPa	E_2 = 56.75 GPa	E_3 = 7.776 GPa
ν_{12} = 0.069	ν_{23} = 0.4134	ν_{31} = 0.4134
G_{12} = 2.539 GPa	G_{23} = 2.092 GPa	G_{31} = 2.092 GPa

The Titanium used in this project is a Grade 2, annealed foil. Its properties are listed in Table 4.2 below.

Table 4.2 Titanium foil properties

Titanium foil Grade 2, Annealed		
E = 102 GPa	ν = 0.34	G = 41.67 GPa

4.3.2 Model geometry and other parameters

The finite element DCB specimen in this study is modeled after the FF/Ti_1 specimen. A schematic of this model is shown in Figure 4.8.

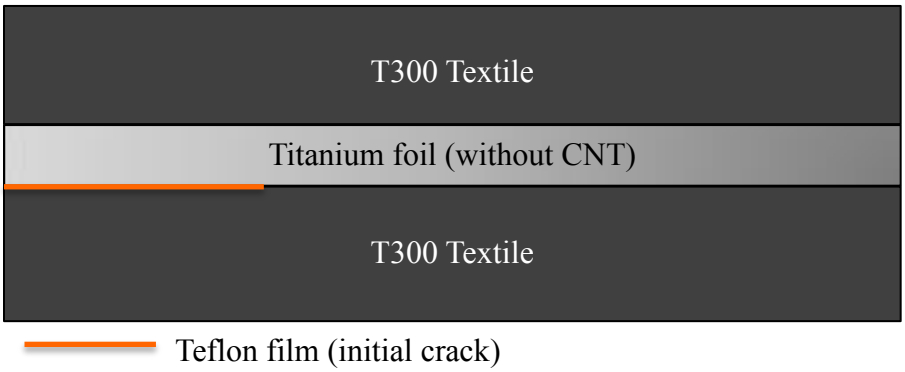

Figure 4.8 Schematic of the DCB model layup

Summary of the specimen's geometry is described in Table 4.4. The specimen is modeled full-length and full-thickness but half-width due to symmetry across the width.

Table 4.3 Summary of DCB model geometry

Length	150	mm
Half-width	12.635	mm
Thickness of each textile layer	2.1865	mm
Thickness of Ti foil	0.127	mm

Table 4.4 shows the data obtained from experiments for opening displacement at crack propagation, crack length and calculated total strain energy release rates correlated to each crack length. Displacement and crack length values are used as input for the model. Strain energy release rates calculated from the model are compared to experimental values.

Table 4.4 Experimental data for FF/Ti_1

Displacement (mm)	Crack length (mm)	G (J/m^2)	G adjusted (J/m^2)
1.98	43.27	162.22	154.84
4.57	51.77	318.58	306.38
10.08	57.27	429.02	414.12
12.50	67.27	458.82	445.19
15.75	74.27	477.74	464.84
16.99	81.77	474.90	463.23
19.99	86.27	458.68	447.98
21.39	95.77	436.87	427.66
22.50	99.27	437.56	428.66

4.3.3 Meshing and convergence

The DCB model is meshed with quadratic serendipity hexahedra (20-node brick) elements as shown in Figure 4.9. Two elements are used through the thickness of each textile layer. The mesh is refined along the free edge to capture edge effects.

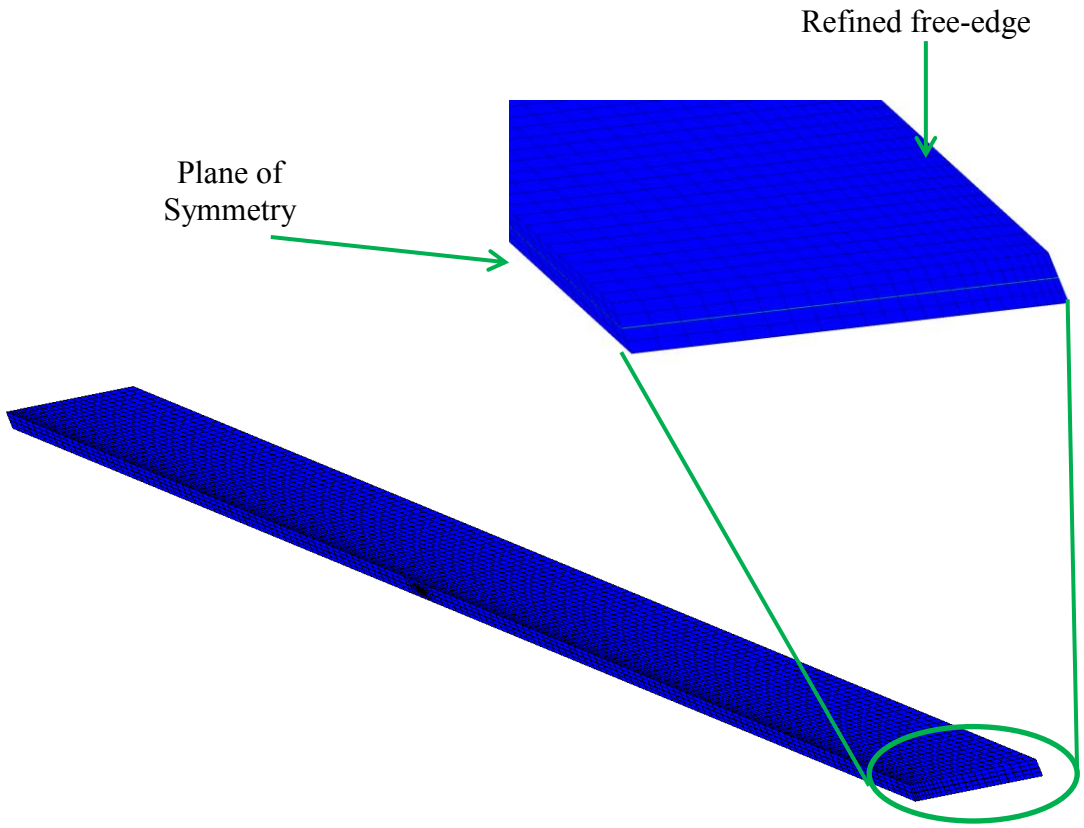

Figure 4.9 FE model of the half-width DCB specimen

To study the effect of mesh refinement around the crack tip, analyses are carried out for mesh with and without refined crack tip region. The refined mesh around the crack tip illustrated in Figure 4.10. To investigate whether results from this model is mesh-dependent or not, further refinements are done. Meshes are generated using four elements, instead of two, through thickness of each textile layer. Region around the crack tip is more refined.

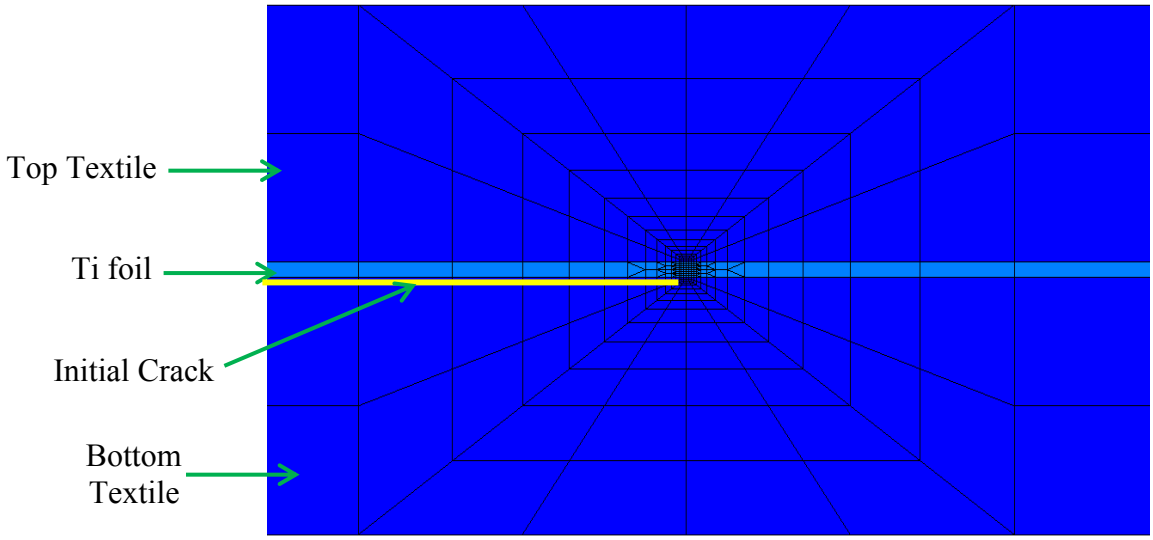

Figure 4.10 Refined mesh around the crack tip

4.3.4 Boundary conditions

Since the model is half-width, symmetric boundary condition must be applied at the cut plane. The bottom edge at the end of pre-cracked side is pinned while the top edge is applied opening displacement in the z-direction. The coordinate system and illustration of applied boundary conditions are shown in Figure 4.11.

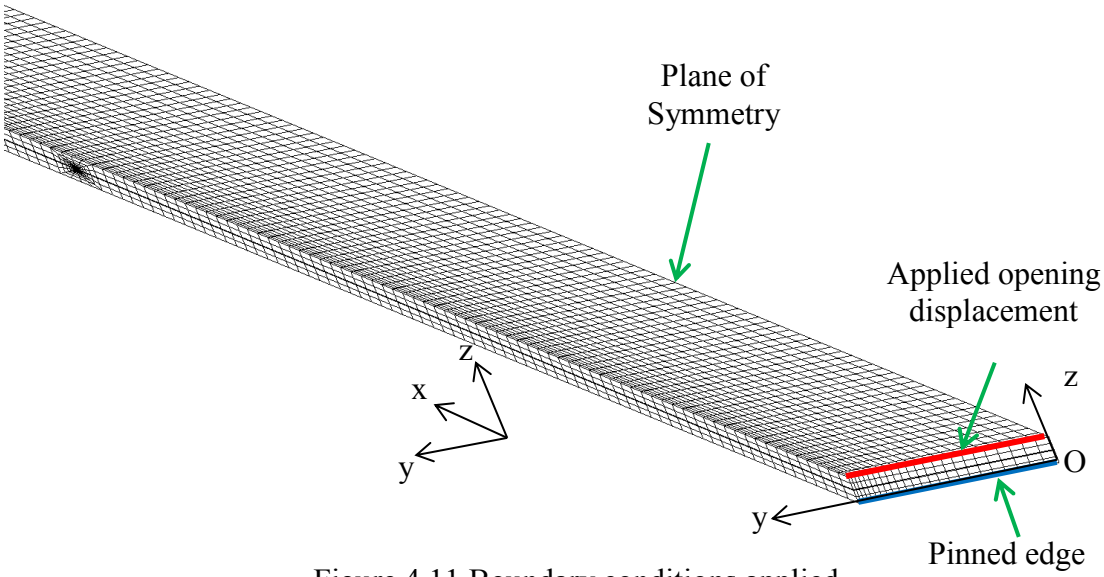

Figure 4.11 Boundary conditions applied

4.3.5 Results and discussions

4.3.5.1 Results from closed-form solutions

Results from the solution derived in this study greatly agree with the total strain energy release rates calculated from solution proposed by Williams. Figure 4.12 shows comparisons between the predictions obtained from both analytical solutions where the data points overlaid each other. Experimental data as listed in Table 4.4 are also depicted on the same plot. The models predict the crack initiation fracture toughness very well as shown. However, as the crack propagates, while R-curve behavior is observed from the experimental data, the analytical solutions for strain energy release rate fluctuate. Never the less, the general trend is a decrease in G values as a function of increasing crack length. The discrepancies in analytical and experimental results can be explained as follows. In the models, it is assumed that the crack stayed at the interface between the

metal foil and the PMC. Effective elastic properties of the PMC were used without taking into consideration presence of CNTs. As discussed earlier in the experimental section, the crack changed its plane as it propagated. In other words, the experimental values would have corresponded to crack tip location either exactly adjacent to the Titanium surface or in the resin rich region between the Ti and the fuzzy fabric layer next to it, or very close to the surface of fuzzy fabric. In addition, the existence of CNTs at the interface can play an important role in the calculated values of strain energy release rate. It should also be noted that the experimental data had scatter and the set of data plotted in Figure 4.12 came from a single specimen. As a result, it is inappropriate to conclude that the mathematical models overestimate the experimental results. Rather, it should be stated that, since the models did not take into account all the features that the real specimen embodied, and the crack-jump phenomenon was not considered in the models, the computational estimation of delamination growth is not representative of the experimental R-curve response.

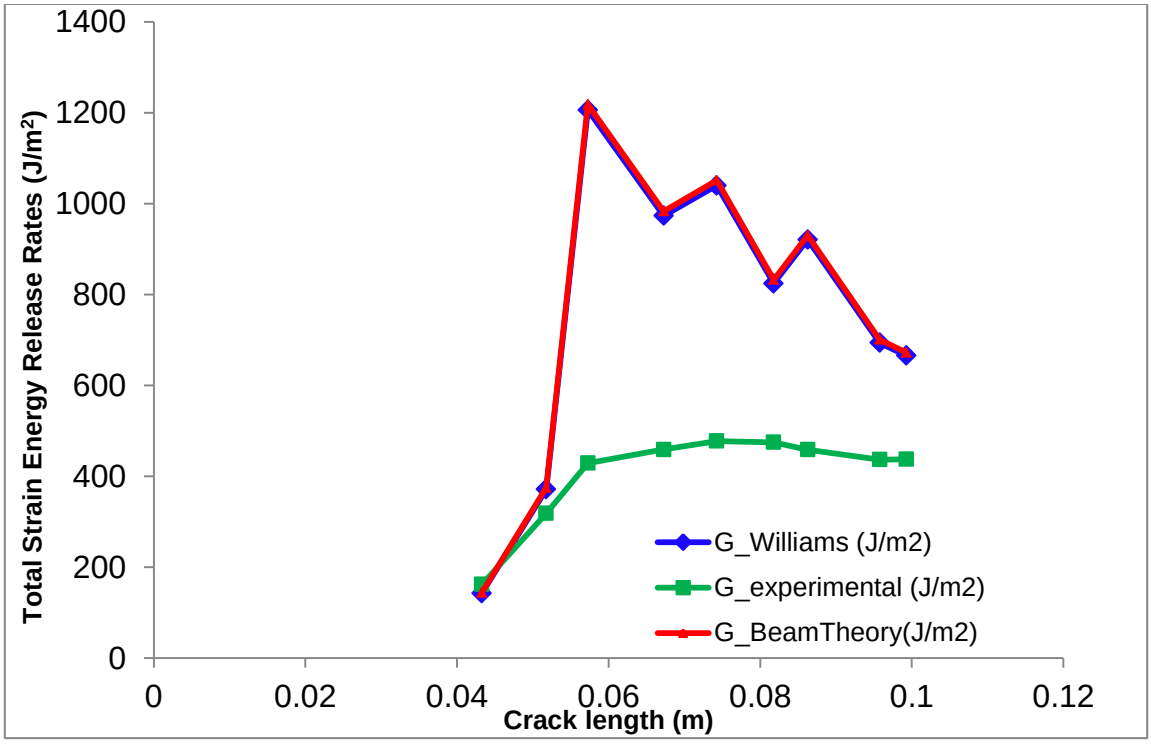

Figure 4 4.12 Values obtained from experiment and both analytical solutions for total train energy release rates plotted versus crack length

The results from Williams' solution suggest a constant ratio G_{II} to G_I of 1.4%. Figure 4.13 shows the plot of G_I, G_{II}, G_{Total} calculated using Williams' model versus crack length. This indicates a low mode-mixity given the asymmetric geometry and that the crack locates and propagates in the bimaterial interface between Ti and PMC. It should be noted that that thickness of Ti foil is only 2.8% the thickness of the entire composite beam and that the Young's modulus of Ti is almost double the longitudinal modulus of PMC.

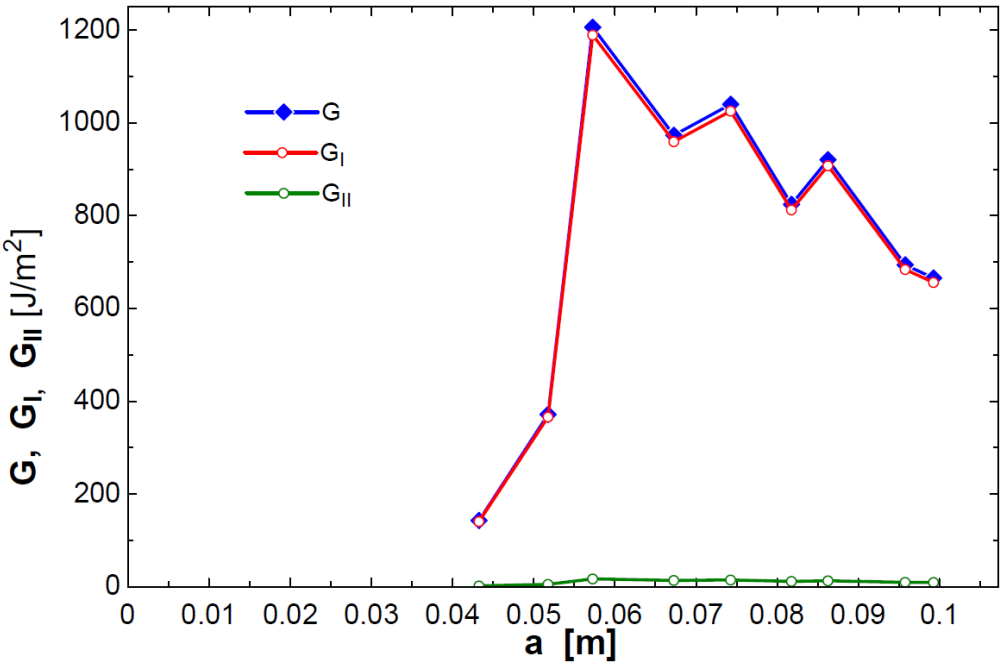

Figure 4.13 G_I, G_{II}, G_{Total} calculated using Williams' model versus crack length

4.3.5.2 Results from FE models with Beta

The deformed beam and example of stress distributions of a model with refined mesh around the crack tip are shown in Figure 4.14. The values are in Pa unit. It can be seen from the stress profile around the crack tip that there is stress concentration in the foil and stress distribution is not completely symmetric around the crack tip.

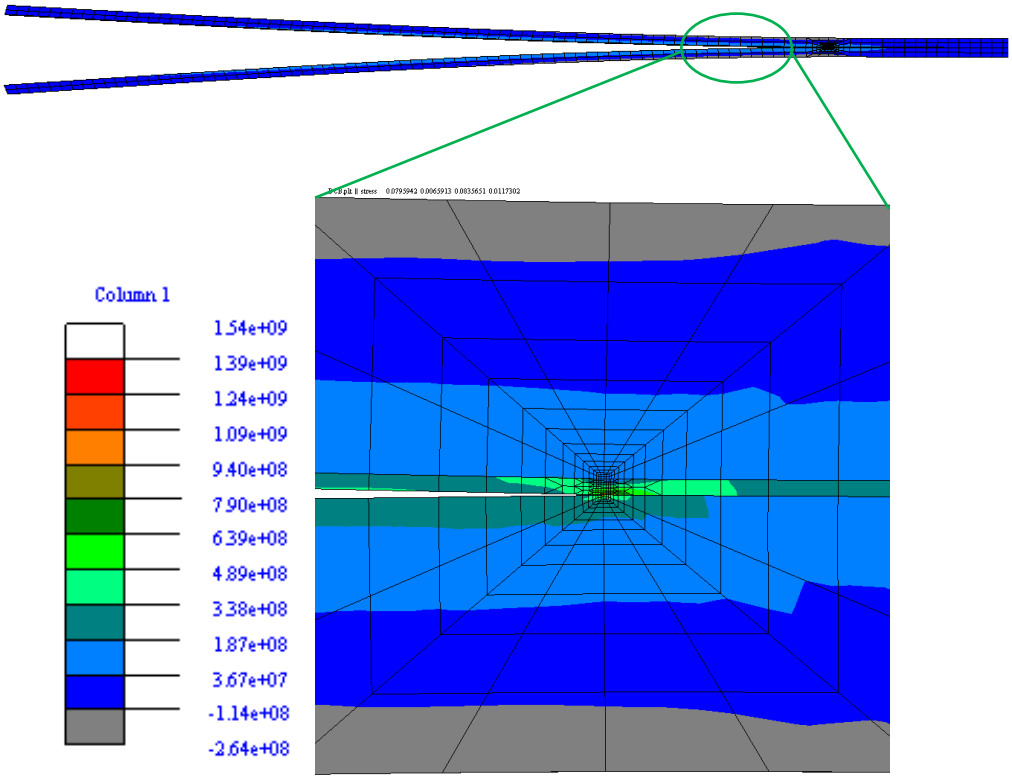

Figure 4.14 Example of stress contour in the deformed DCB beam of refined mesh

For the model with mesh that does not have crack tip refinement, example of deformed beam and stress distribution is shown in Figure 4.15.

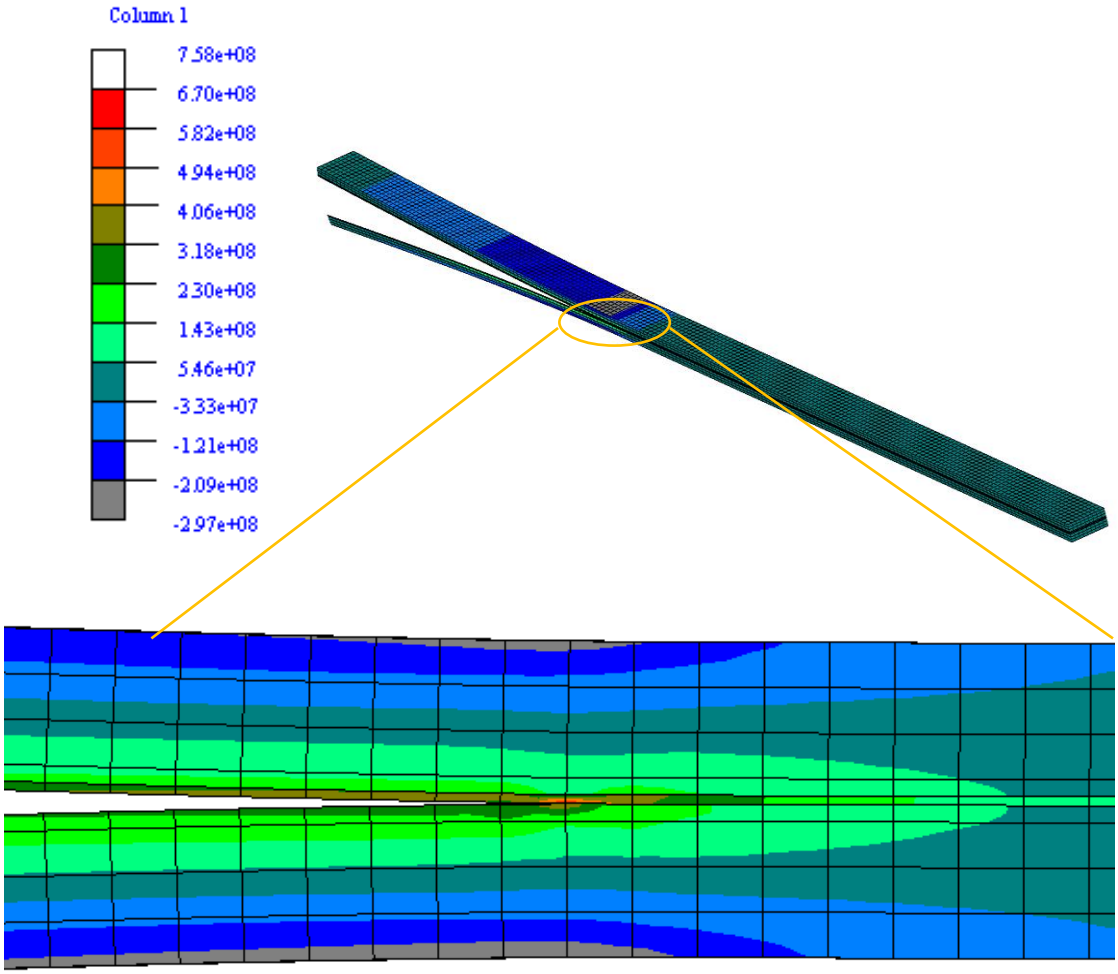

Figure 4.15 Example of stress contour in the deformed DCB beam of non-refined mesh

Figures 4.16 and 4.17 show the strain energy release rates across the width calculated using nodal forces along the crack front plotted versus the normalized half-width. These results are generated for the initial crack length of 74.27 mm and corresponding opening displacement of 15.75 mm as taken from experimental data shown in Table 4.4. Figure 4.16 came from VCCT results for a less refined mesh than

the mesh used to generate plot in Figure 4.17. That is, instead of using two elements through thickness of each textile layer as described above, four elements were used through thickness of each textile layer in the mesh for results plotted in Figure 4.17. The region around the crack tip in the latter mesh is refined at a higher degree. The mentioned two plots indicate that the results are mesh-dependent. Figure 4.18 shows results from the model that has the mesh without refinement around crack tip. Mode-mixity predicted from this model is very small. In fact, the G_{II} to G_I ratio is approximately 1%.

For both cases, the results show that this is a mode I dominant problem and there is some mode II due to sliding shearing effect. However, for a less refined mesh, mode-mixity cannot be seen as clear as for the more refined mesh. In other words, the ratio between mode II and mode I strain energy release rates is higher for the more refined mesh, while G_{III} remains null contribution as there is no scissoring shear presented. In addition, the calculated total strain energy release rate from the model, for both the described cases, is above 900 J/m^2, which is almost double the total strain energy release rate obtained from experiment, which is 464.84 J/m^2.

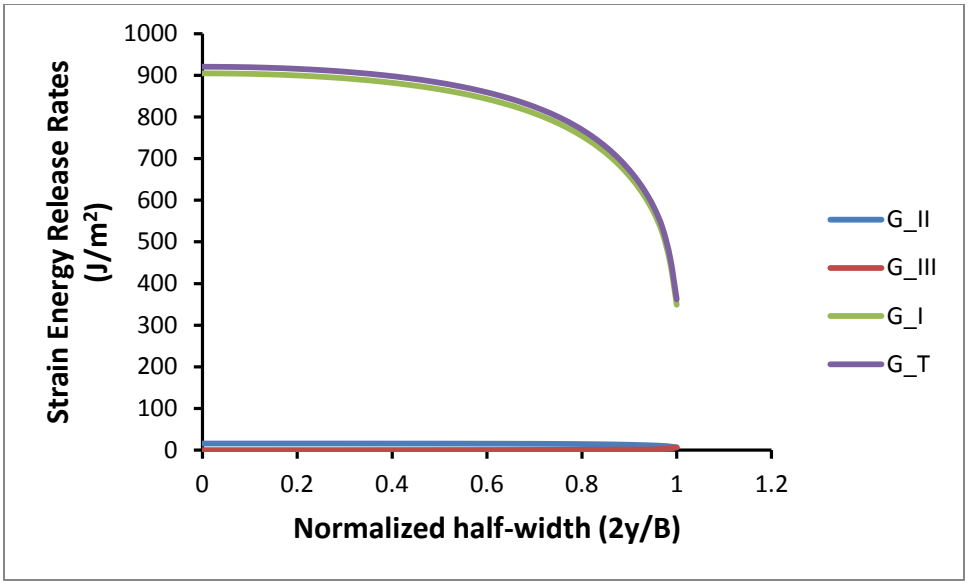

Figure 4.16 Strain energy release rates vs normalized half width for a = 74.27 mm, model using 2 elements through thickness of each textile layer with refined mesh at crack tip

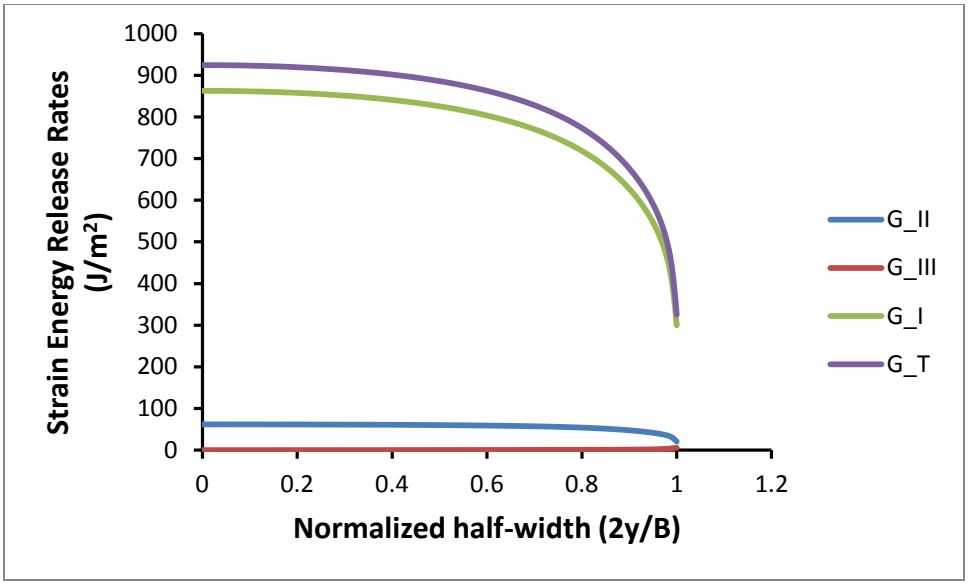

Figure 4.17 Strain energy release rates vs normalized half width for a = 74.27 mm, model using 4 elements through thickness of each textile layer with a more refined mesh at crack tip

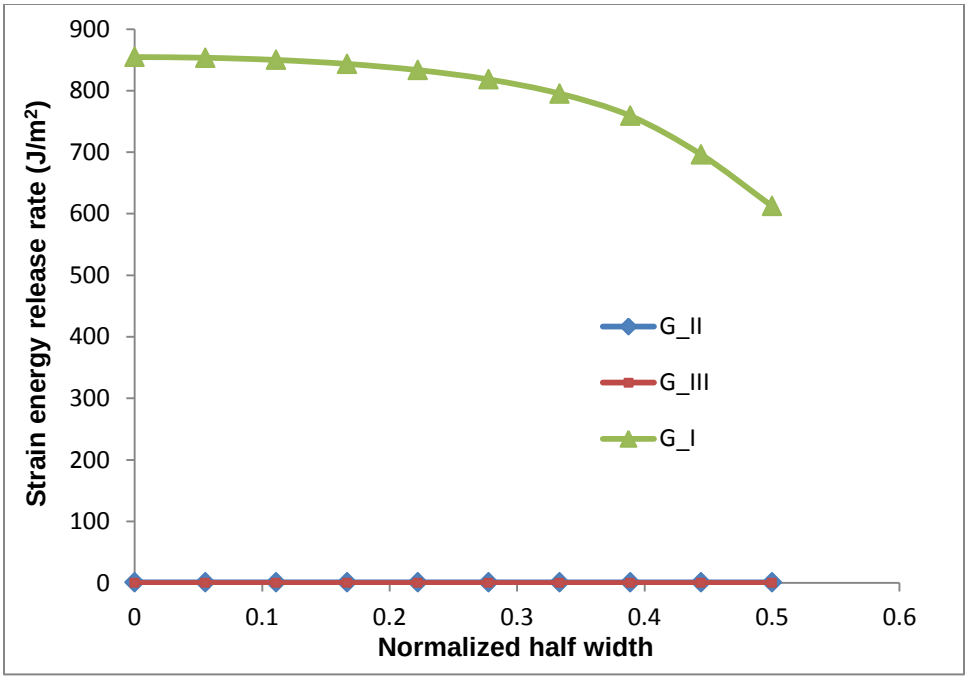

Figure 4.18 Strain energy release rates vs normalized half width for a = 74.27 mm, model using mesh without tip refinement

4.3.5.3 Convergence study

Since mesh-dependent behavior was observed in the results discussed in previous section, convergence study is carried out. Further refinement in the mesh at the crack tip for models with Ti foil was analyzed. However, very slow convergence process was seen. The more refined is the mesh, the higher degree of mode-mixity is observed. One of the reasons can be because the crack locates at and propagate in a bi-material interface. Properties for Ti and PMC are too different and the FEA results are harder to converge. This hypothesis is checked by carrying out analysis for the same models, but

properties of Ti are replaced with PMC properties. That is, the crack now lies inside a monolithic materials and mode-mixity only comes from slightly asymmetric geometry. Figures 4.19 and 4.20 show the results from two models, one has a more refined mesh than the other. The two plots show now significant differences; in fact, they are almost identical. It can be concluded that the existence of Titanium mid-layer makes a difference. More investigations should be carried out to study the effect of bi-material interfaces.

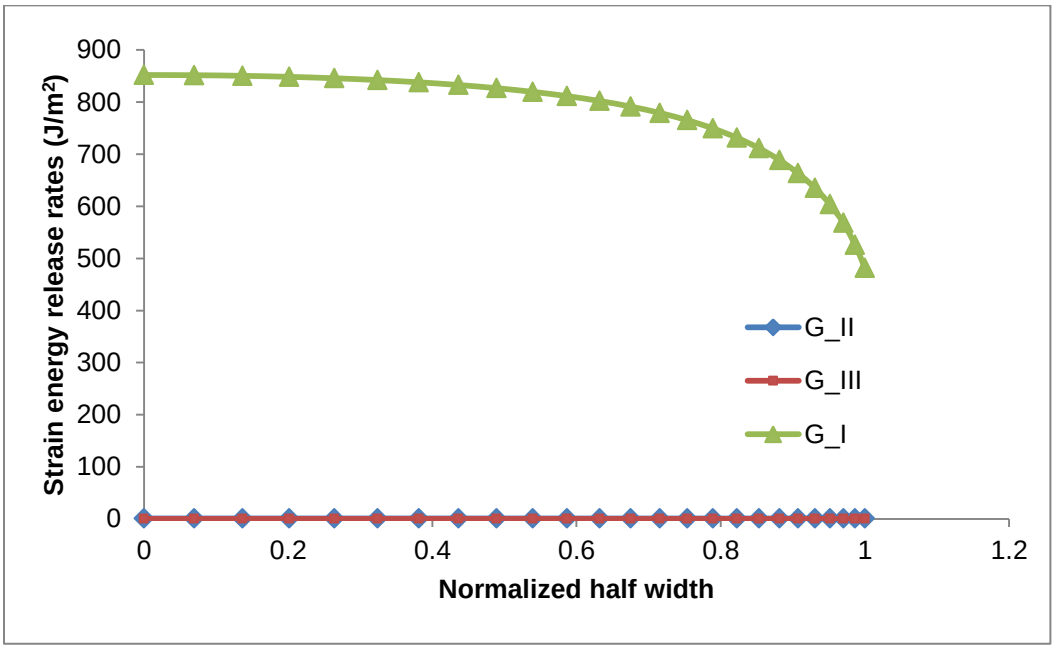

Figure 4.19 Strain energy release rates vs normalized half width for a = 74.27 mm, model with less refined mesh, Ti properties are replaced with PMC properties

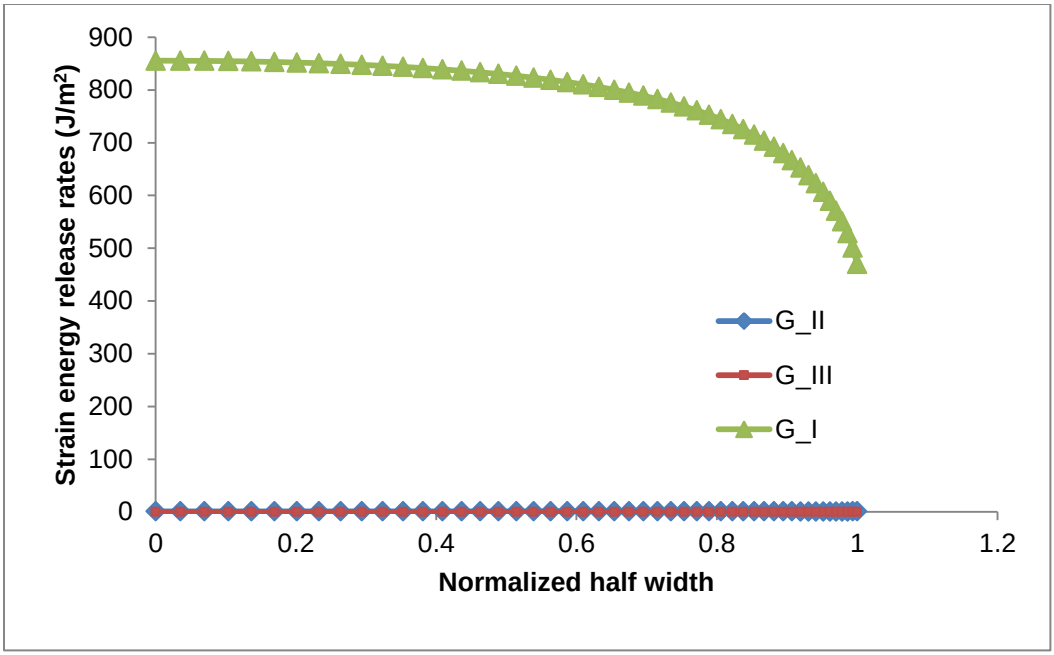

Figure 4.20 Strain energy release rates vs normalized half width for a = 74.27 mm, model with more refined mesh, Ti properties are replaced with PMC properties

4.3.5.4 Mode-mixity predictions: FEA vs. analytical solutions

The analytical solution proposed by Williams suggested a G_{II} to G_I ratio of 1.4% while FEA analyses indicate that ratio to be approximately 1%. Figure 4.21 compared G_{II} and G_I values calculated at different crack lengths from both FEA and closed-form solution.

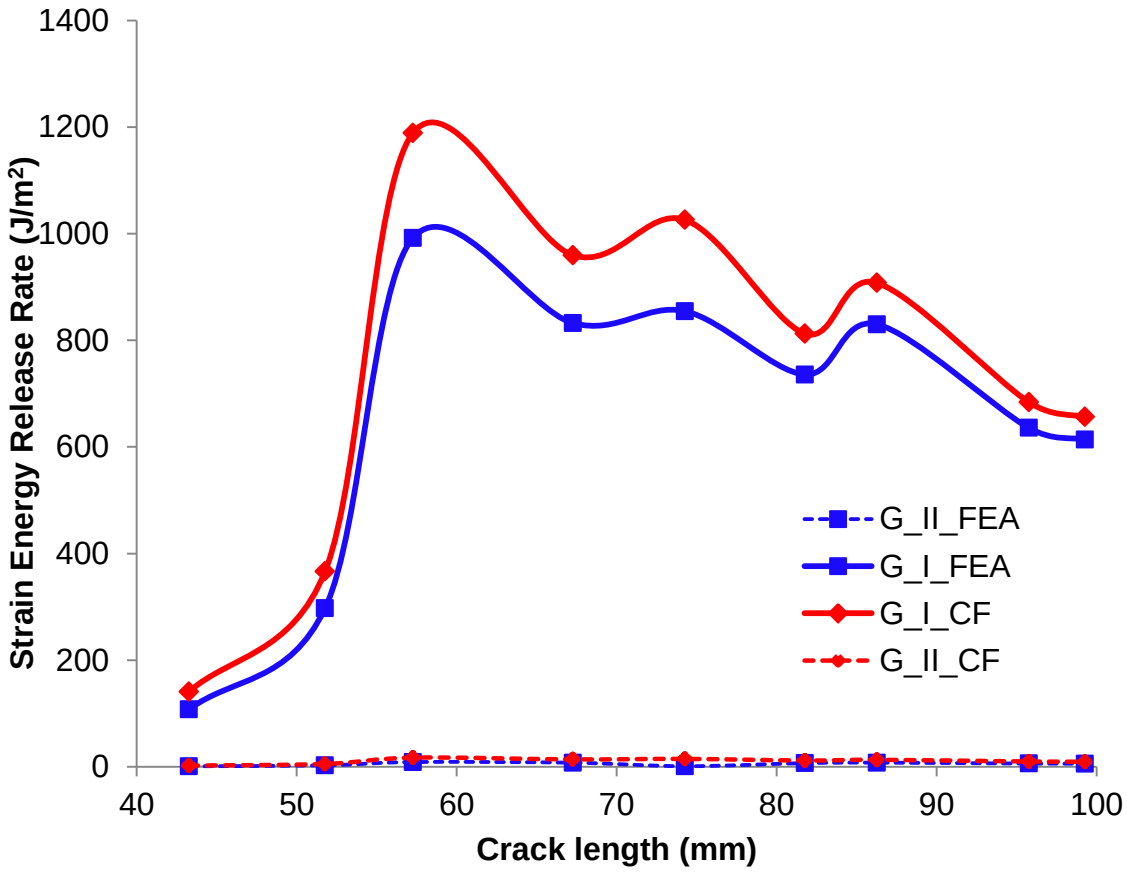

Figure 4.21 G_{II} and G_I versus crack lengths calculated from FEA models and closed-form solution proposed by Williams

5 CONCLUSIONS

5.1 Conclusions

Multifunctional hybrid composites are attractive material systems for wide range of applications. As in all heterogeneous, anisotropic systems overcoming delamination is a critical issue. This study focused on understanding of the bonding and interlaminar fracture toughness of PMC-Ti hybrid laminates with and without CNT reinforcement.

For the first time, a set of hybrid composite panels were made with Titanium foil located in the center, surrounded by two layers of CNT reinforced carbon fabric. Room temperature fracture toughness tests revealed that the interfacial bonding was improved up to 2.5 times in samples with CNT reinforced interface. It is also noted that there are no significant differences in the fracture toughness of fuzzy interfaces at room temperature versus elevated temperature. A general trend observed in this study confirms that CNTs improve bonding between the thin metal foil and polymer matrix composites both at room temperature and high temperature. During the DCB tests, the crack propagation did not consistently remain in the same plane and jumped to adjacent layers. Thus it is important to use these tests as a general study of the Metal-PMC interfaces. Intensive optical microscope and SEM investigations of cross-sections and fracture surfaces documented that CNTs are not necessarily firmly attached to the carbon fabric surface nor to metal foil but remained in the nearby resin rich areas of the interface. Furthermore, the distribution of CNTs is observed to be non-uniform.

Computational models have been developed to help interpret experimental results and further investigate damage modes at the interface. Total strain energy release rate obtained from FE model and closed form solution is within 10% of each other. The ratio between the mode II and mode I strain energy release rates obtained in both analytical solutions and FE models with coarse and fine mesh runs are within 2% between all models. Models with finer mesh exhibit slightly higher mode-mixity.

5.2 Future Work

In the current research, the elevated temperature used for testing was 110^{o}C, as suggested by T_g characterizations with DSC. In order to have higher working temperature, the composites must utilize a different thermoset matrix that has higher glass transition temperature such as bismaleimide (BMI) or polyimide resins. In addition, the digital image correlation (DIC) techniques can be used as an in-situ testing method with the traditional fracture toughness tests. Results from DIC can give strain profile around the crack tip, which can be compared to strain field obtained from finite element models and verify the accuracy of FEA in predicting mode-mixity.

In this work, the effects of CNTs at the interface as well as thermal effects have not been addressed in the computational models. Methods should be developed to model the fuzzy layers and study the influences of CNTs to interlaminar fracture toughness. Effects of temperature should also be taken into account, especially for composites that have BMI or polyimide matrix that are cured and can operate at much

higher than systems contain epoxy matrix. Thus, residual stress could be a big issue in these situations.

REFERENCES

[1] Shima, D.J., Alderliestenb, R.C., Spearinga, S.M., Burianek, D.A. (2003). Fatigue crack growth prediction in GLARE hybrid laminates. *Composites Science and Technology*, 63:1759–1767.

[2] Vlot, A., Gunnink, J. W. (2001). *Fiber Metal Laminates – An Introduction.* Dordrecht, The Netherlands: Kluwer.

[3] Khan ,S.U., Alderliesten, R.C., Benedictus R. (2009). Post-stretching induced stress redistribution in Fibre Metal Laminates for increased fatigue crack growth resistance. *Composites Science and Technology*, 69(3-4):396-405.

[4] Krishnakumar, S. (1994). Fiber Metal Laminates - The Synthesis of Metals and Composites. *Materials and Manufacturing Processes*, 9(2):295-354.

[5] Burianek, D. A. (2001). *Mechanics of Fatigue Damage in Titanium Graphite Laminates.* Cambridge: Massachusetts Institute of Technology.

[6] Alderliesten, R.C., Benedictus, R. (2008). Fiber/Metal composite Technoligy for Future Primary Aircraft Structures. *Journal of Aircraft*, 1182-1189.

[7] Johnson, W. S., Hammond, M. W. (2008). Crack Growth behavior of internal titanium plies of a fiber metal laminate. *Composites Part A: Applied Science Manufacturing* , 39(11):1705-1715.

[8] Tong, L., Mouritz, A. P., Bannister, M.K. (2002). *3D Fibre Reinforced Polymer Composites.* Oxford, UK: Elsevier Science Ltd.

[9] Mouritz A. P., Leong K. H, Herszberg I. (1997). A review of the effect of stitching on the in-plane mechanical properties of fibre-reinforced polymer composites. *Composites Part A: Applied Science Manufacturing*, 28(12):979-991.

[10] Steeves, C. A. (2006). In-plane properties of composite laminates with through thickness pin reinforcement. International Journal of Solids Structures. *International Journal of Solids and Structures*, 43(10): 3197-3212.

[11] Mouritz, A. P. (2007). Review of z-pinned composite laminates. *Composites Part A: Applied Science Manufacturing*, 38(12):2383-2397.

[12] Zhu, J., Kim, J., Peng, H. et al. (2003). Improving the Dispersion and Integration of Single-Walled Carbon Nanotubes in Epoxy Composites through Functionalization. *Nano Letters*, 3(8):1107–1113.

[13] Zhu, J., Peng, H., Rodriguez-Marcias, F. et al. (2004). Reinforcing Epoxy Polymer Composites Through Covalent Integration of Functionalized Nanotubes. *Advanced Functional Materials*, 14(7):643-648.

[14] Bekyarova, E., Thostenson, E. T., Yu, A., Kim, H., Gao, J., Tang, J., Hahn, H,. T., Chou, T. W., Itkis, M. E., Haddon, R. C. (2007). Multiscale Carbon Nanotube-Carbon Fiber Reinforcement for Advanced Epoxy Composites. *Langmuir*, 23(7):3970-3974.

[15] Standard test method for mode I internalminar fracture toughness of unidirectional fiber-reinforced polymer matrix composites. ASTM D 5528-01. (2007). *Annual Book of ASTM Standards*.

[16] P. Qiao and J. Wang, "Mechanics and fracture of crack tip deformable bi-material interface," *International Journal of Solids and Structures*, vol. 41, no. 26, pp. 7423-7444, Dec. 2004.

[17] S. Bennati, M. Colleluori, D. Corigliano, and P. S. Valvo, "An enhanced beam-theory model of the asymmetric double cantilever beam (ADCB) test for composite laminates," *Composites Science and Technology*, vol. 69, no. 11–12, pp. 1735-1745, Sep. 2009.

[18] J.G. Williams, "Fracture mechanics of anisotropic materials," K. Friedrich (Ed.), *Application of Fracture Mechanics to Composite Materials*, Elsevier, Amsterdam (1989).

[19] J. Gere, *Mechanics of Materials.* Thompson Learning, Belmont, CA (2004).

[20] ABAQUS 6.9 EF., Analysis User's Manual, ABAQUS 2009

[21] R. Krueger, "An Approach to Assess Delamination Propagation Simulation Capabilities in Commercial Finite Element Codes," Hampton, VA, April, 2008.

[22] Benzeggagh, M., and M. Kenane, "Measurement of Mixed-Mode Delamination Fracture Toughness of Unidirectional Glass/Epoxy Composites with Mixed-Mode Bending Apparatus," *Composite Science and Technology*, vol. 56 439, 1996.

[23] Reeder, J., S. Kyongchan, P. B. Chunchu, and D. R.. Ambur, "Postbuckling and Growth of Delaminations in Composite Plates Subjected to Axial Compression," 43rd AIAA/ASME/ASCE/AHS/ASC Structures, Structural Dynamics, and Materials Conference, Denver, Colorado, vol. 1746, p. 10, 2002.

[24] B. C. Owens, J. D. Whitcomb, and J. Varghese, "Effect of Finite Thickness and Free Edges on Stresses in Plain Weave Composites," *Journal of Composite Materials*, vol. 44, no. 6, pp. 675-692, Oct. 2009.

APPENDIX A

T300_AM_FF/Ti_1

Room temperature DCB

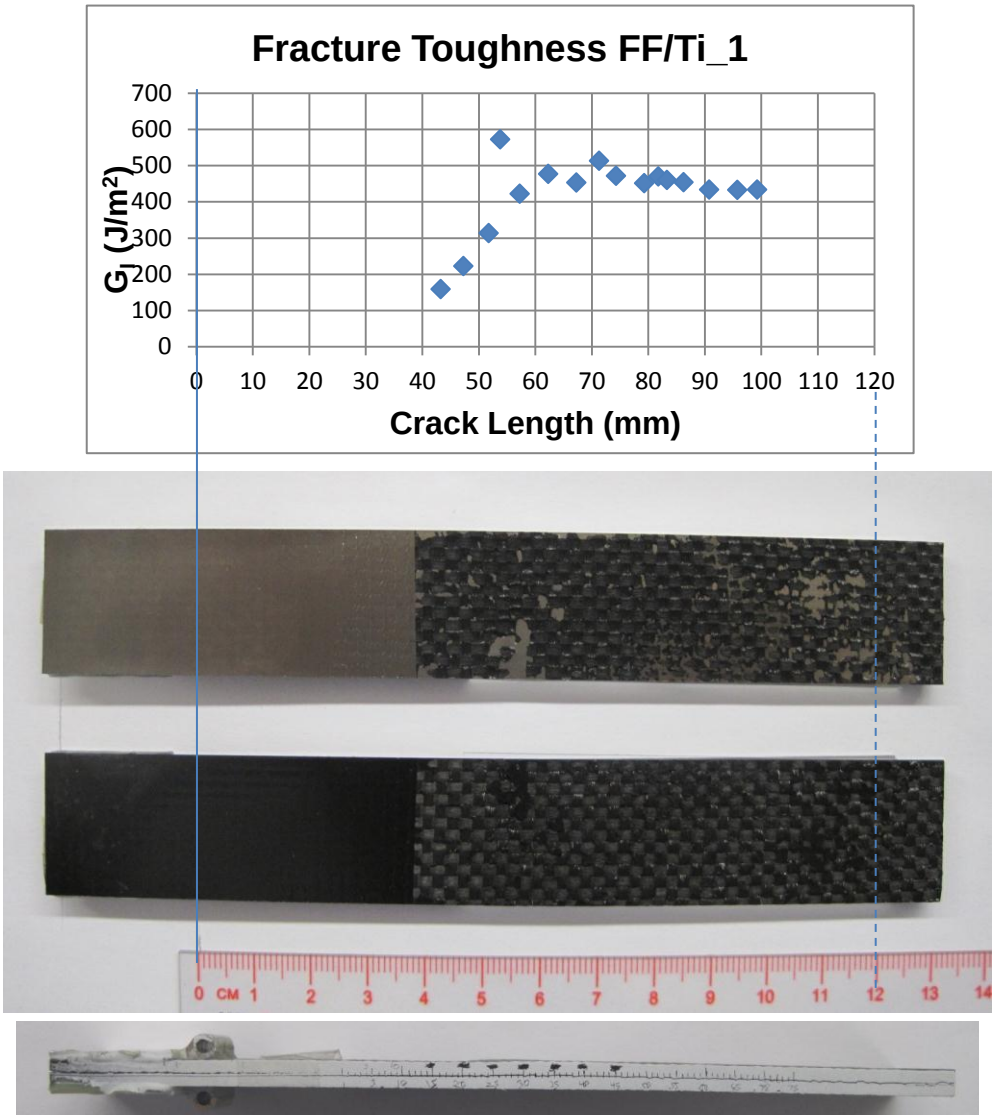

T300_AM_FF/Ti_2

Room temperature DCB (Over-cured specimen)

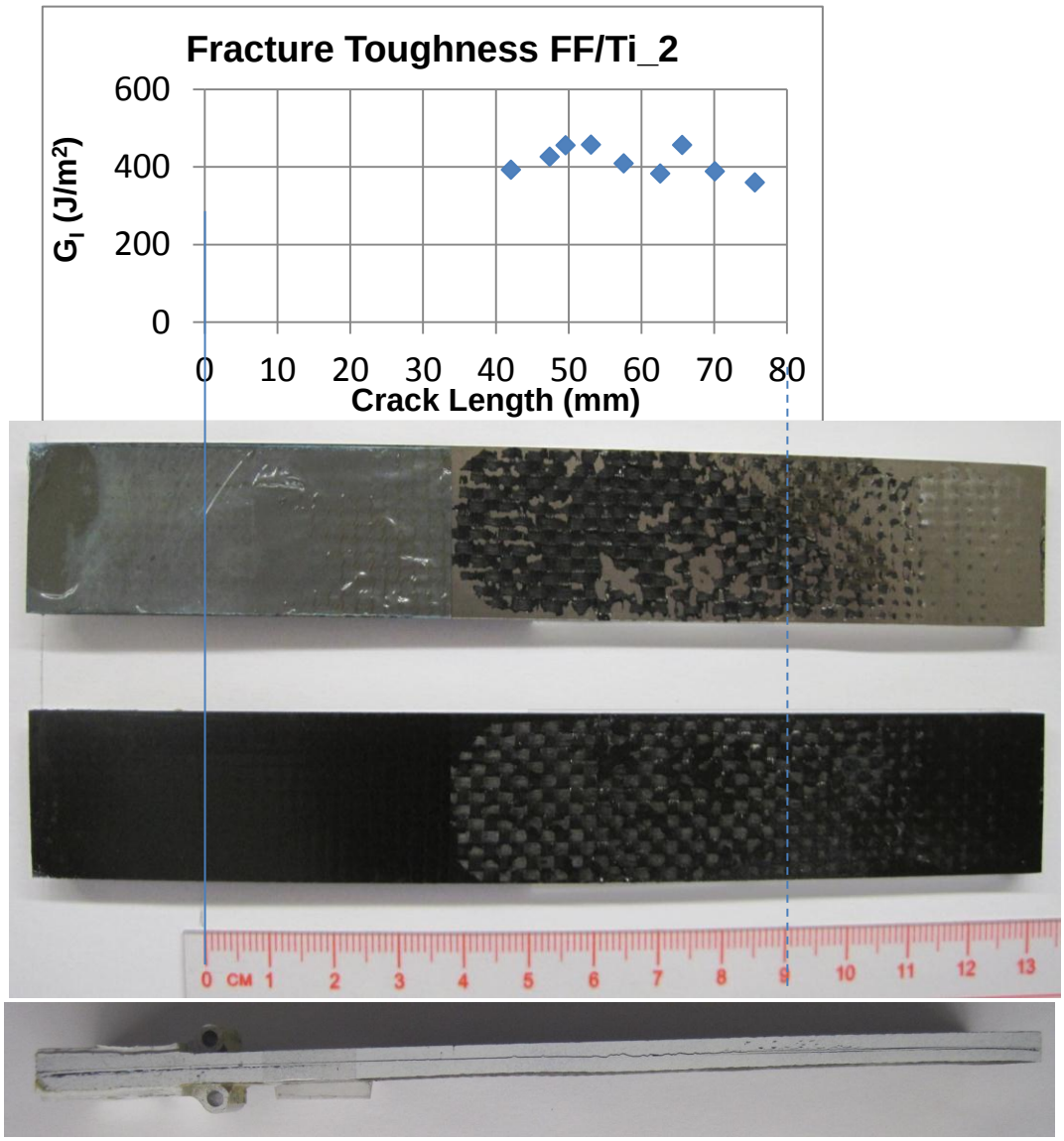

T300_AM_FF/Ti_3

High temperature DCB (Over-cured specimen)

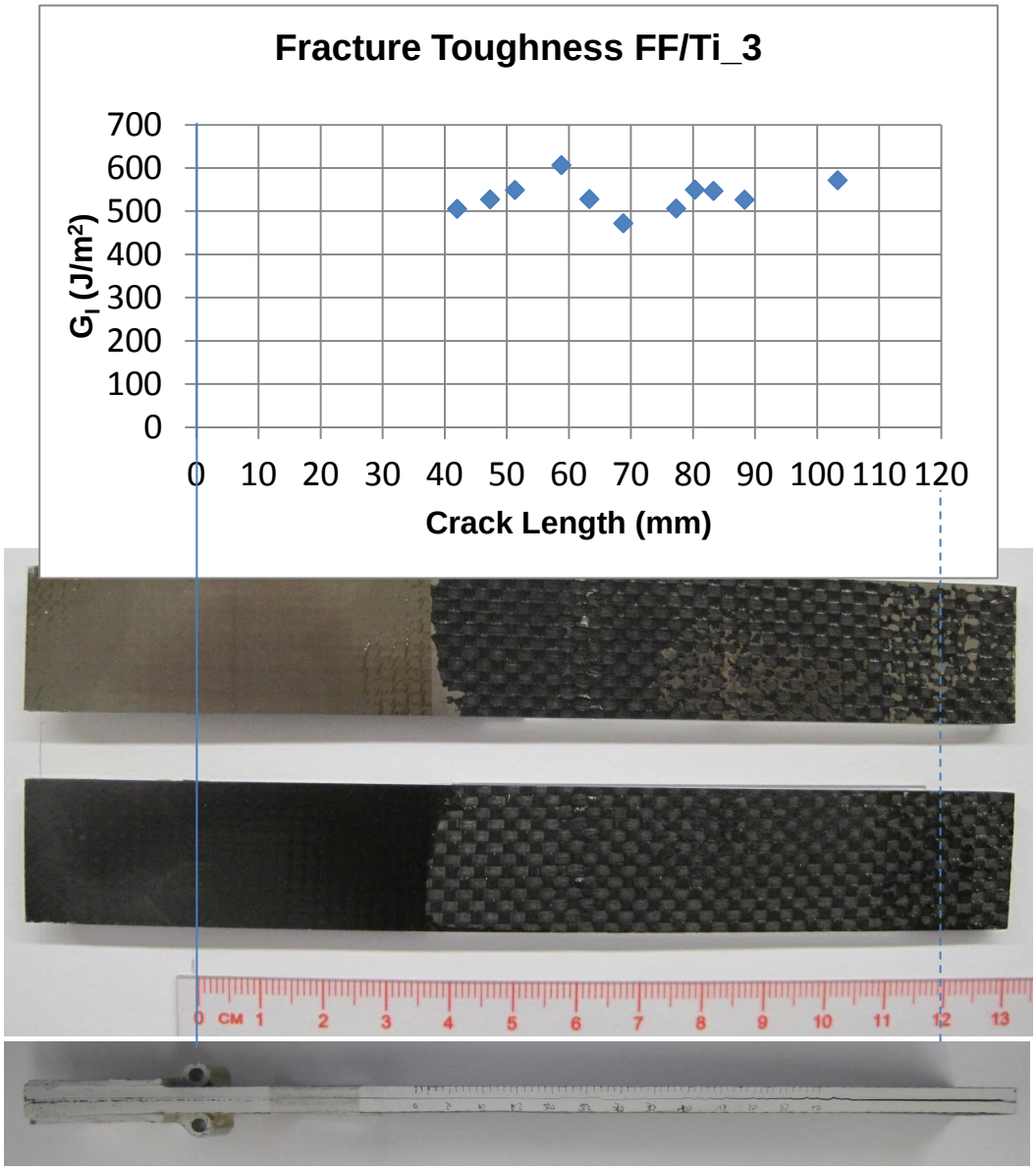

T300_AM_FF/Ti_4

High temperature DCB

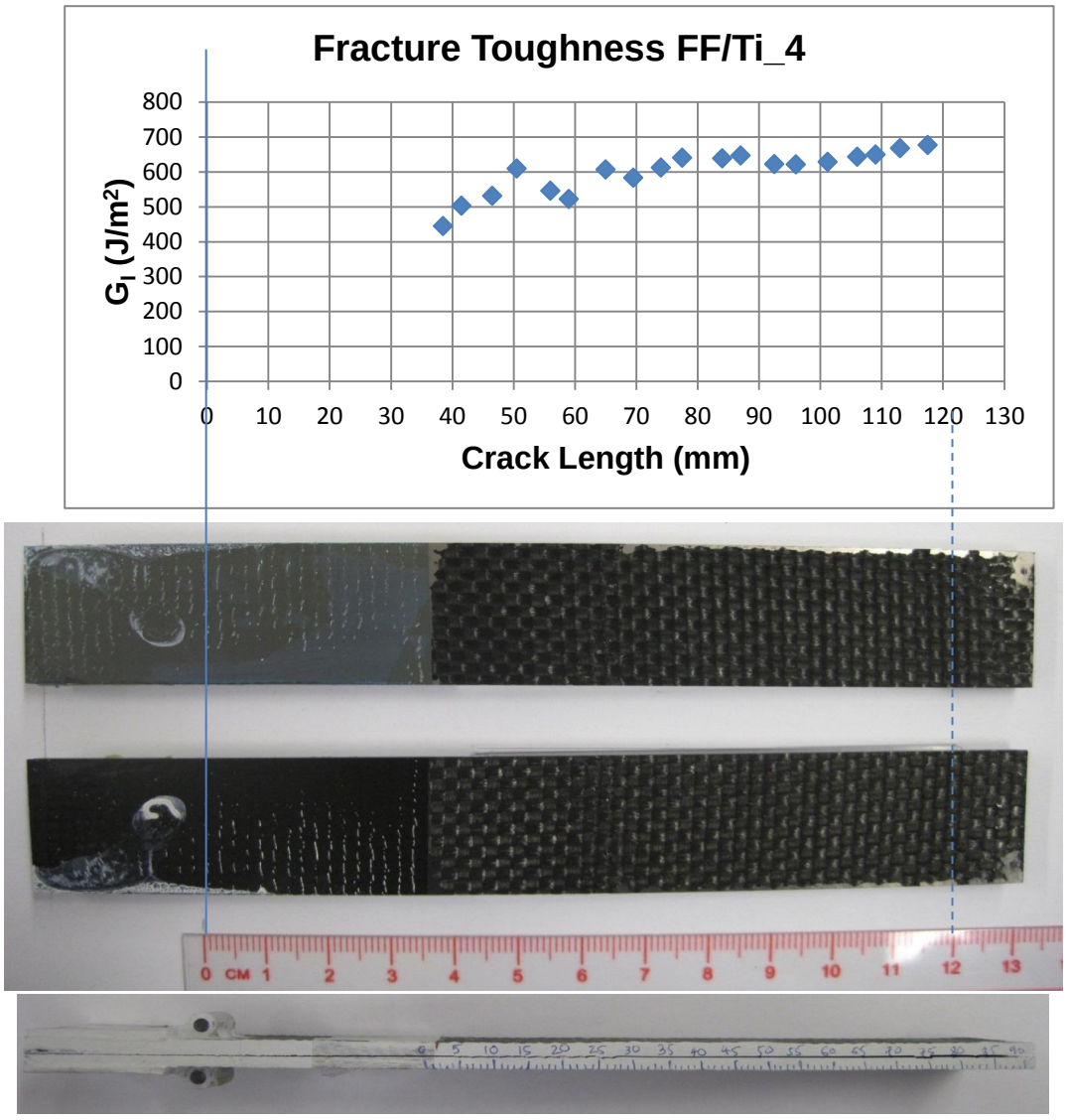

T300_AM_FF/fTi_1

Room temperature DCB

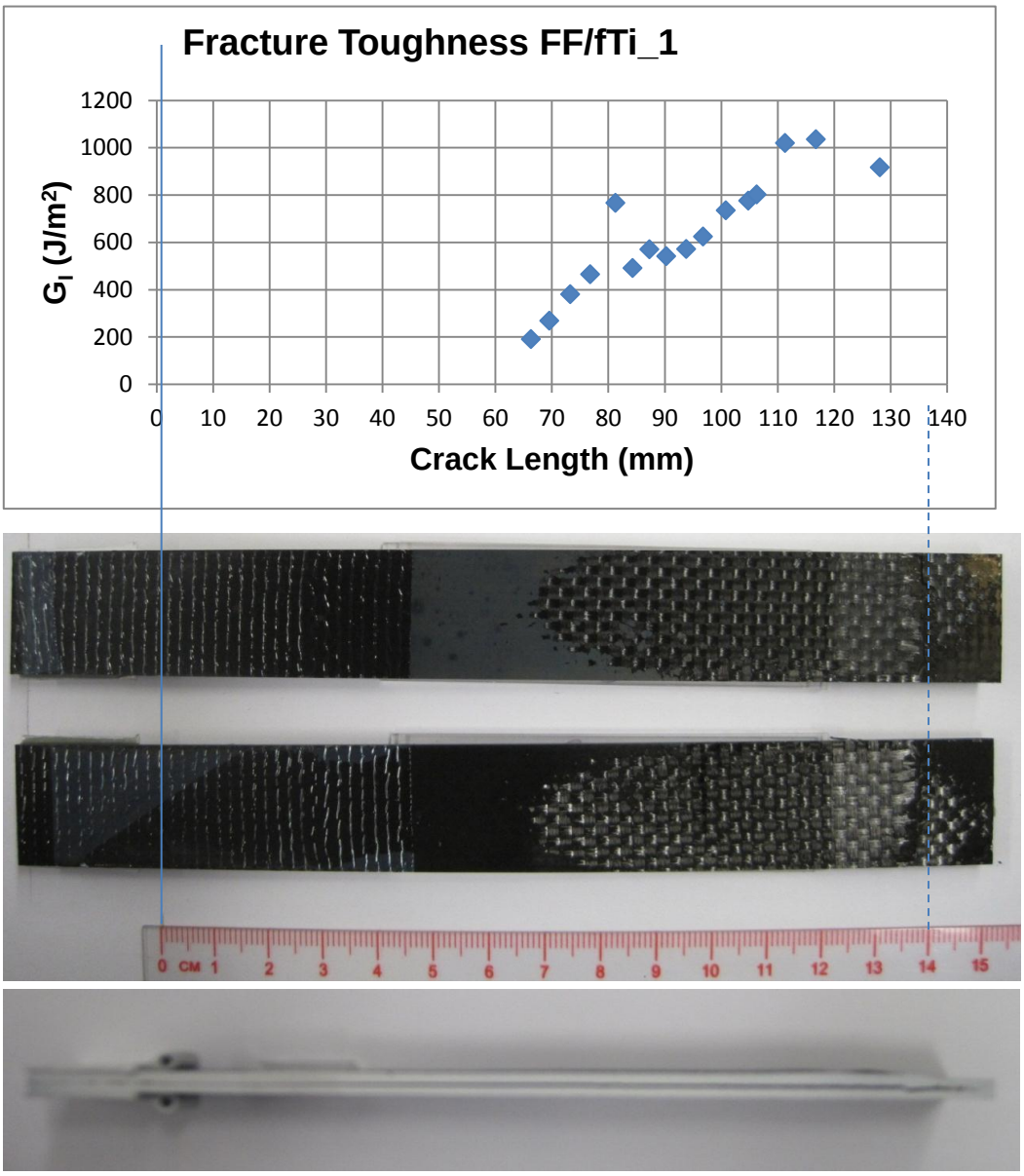

T300_AM_FF/fTi_2

Room temperature DCB (Over-cured specimen)

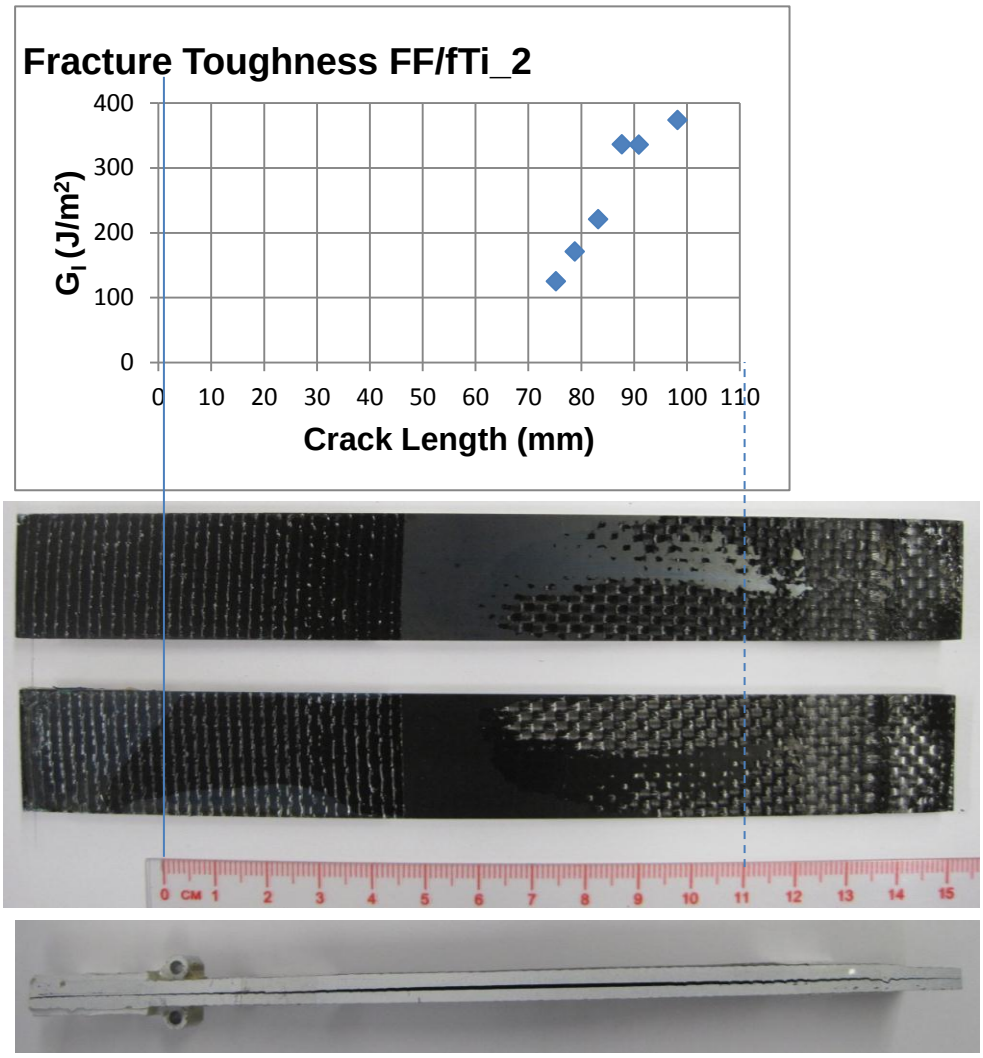

T300_AM_FF/fTi_3

High temperature DCB (over-cured)

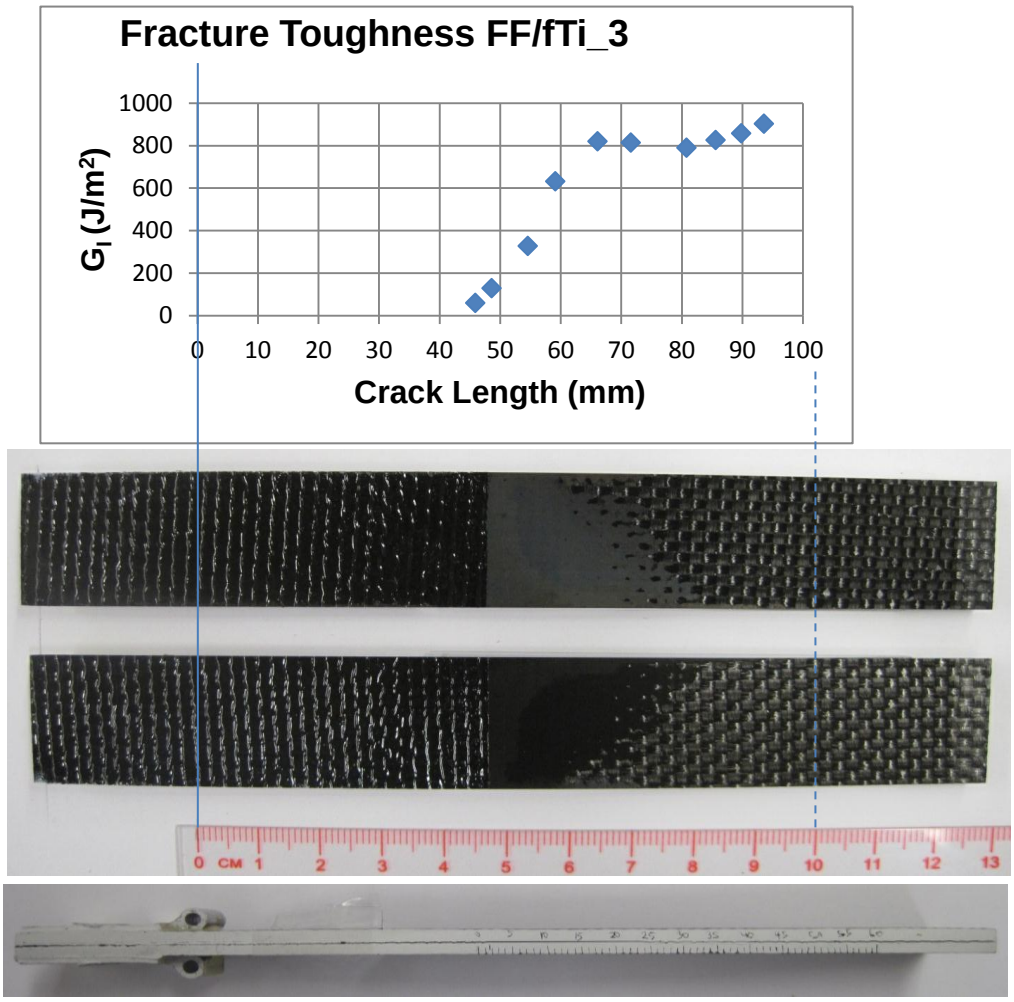

T300_AM_FF/fTi_4

High temperature DCB

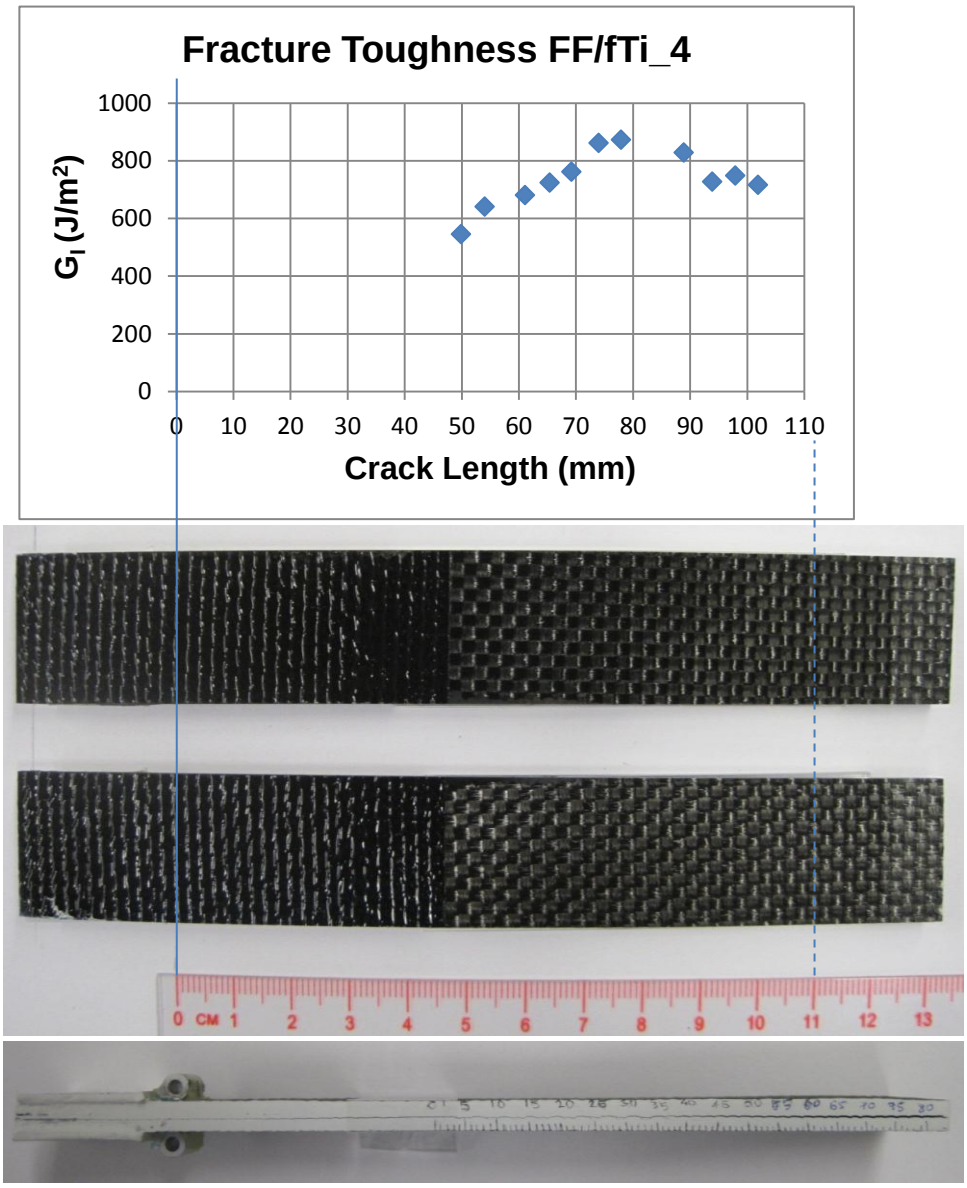

T300_AM_FF/fTi_6

Room temperature DCB

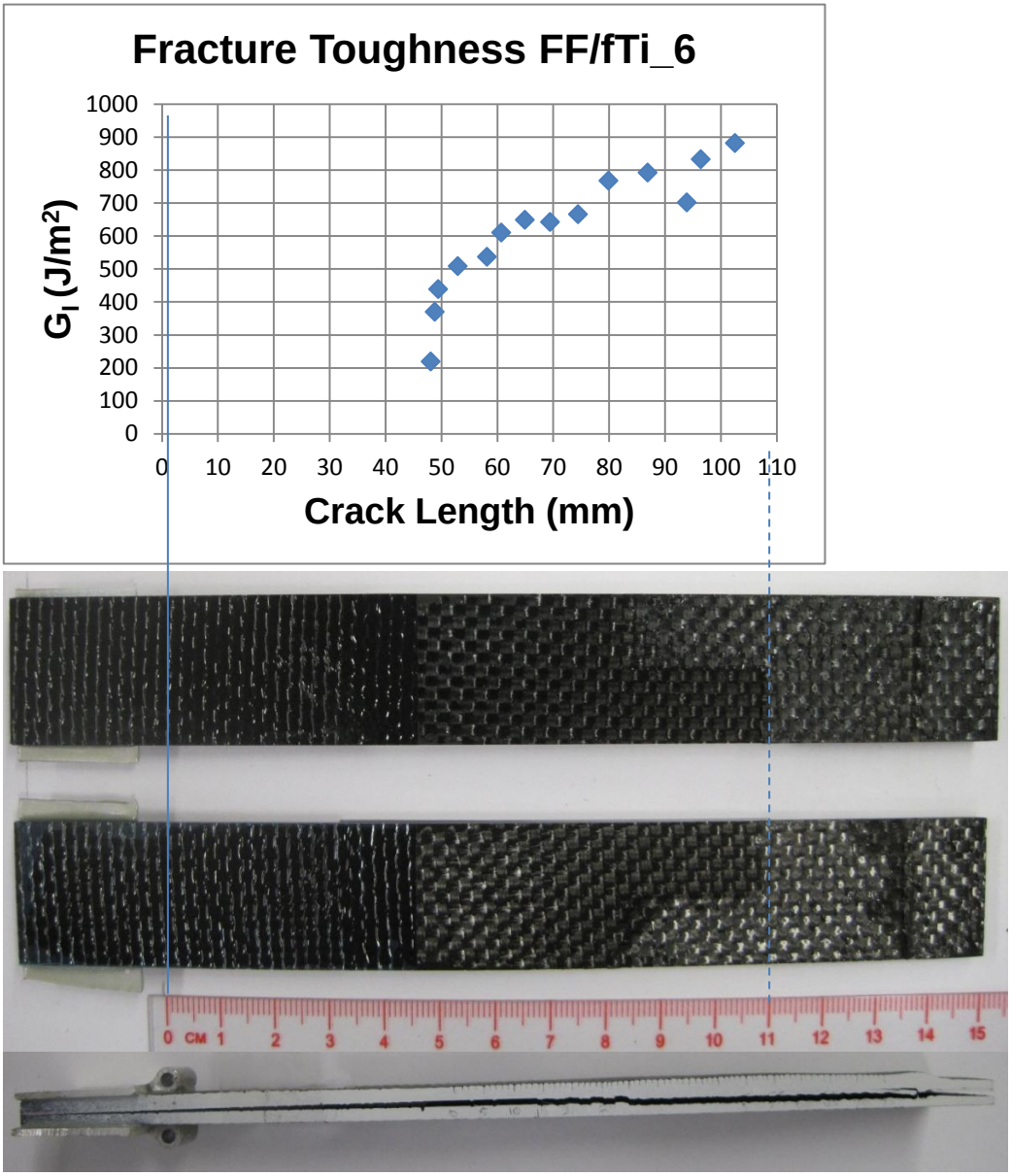

APPENDIX B

B.1 EES program using the analytical solution from beam theory

```
"Beam Theory Analysis for Asymmetric DCB Specimen"
"Specimen Geometry"
B=0.02527 [m] "Specimen width"
{a=0.07427 [m]} "Crack length"
h_Ti=0.000127 [m] "Thickness of Ti layer"
h_PMC=0.0021865 [m] "Thickness of each PMC layer"
{delta=0.015748 [m]} "Opening displacement associated with crack length"
"Material Properties"
"Plain weave T300-EPON862 PMC"
E_PMC=5.675*10^10 "E11 of PMC in Pascal"
{E_Ti=5.675*10^10 "E11 of PMC in Pascal - For convergence check"}
E_Ti=102*10^9 "Young's modulus of Ti in Pascal"
n=E_Ti/E_PMC
"Consider the top arm that contains 1 layer of PMC on top of aTi foil layer"
"Finding location of neutral axis"
"Let h_1 be the location of neutral axis from the top of PMC layer and h_2 be the location of
neutral axis from the bottom of Ti
layer"
h_1=(h_PMC^2/2+(h_Ti/2+h_PMC)*h_Ti*n)/(h_PMC+n*h_Ti)
h_2=h_PMC+h_Ti-h_1
delta_top=delta/2 "Opening displacement of top arm associated with crack length"
"Second moments of area with respect to the neutral axis"
I_PMC_top=1/12*B*h_PMC^3+B*h_PMC*(h_1-h_PMC/2)^2
I_Ti=1/12*B*h_Ti^3+B*h_Ti*(h_2-h_Ti/2)^2
I_Total_top=I_PMC_top+I_Ti
EI_top=I_PMC_top*E_PMC+I_Ti*E_Ti
"Force applied, bending moment and strain energy stored in top arm"
P_1=3*delta_top*EI_top/a^3
M_1=-P_1*a
U_1=P_1^2*a^3/(6*EI_top)
delta_U1=-9/2*delta_top^2*EI_top/a^4
"U_11=3*delta_top^2*EI_top/(2*a^3)"
"Consider the bottom arm that contains only 1 layer of PMC. Second moment of area of bottom
arm:"
I_PMC_bottom=1/12*B*h_PMC^3
EI_bottom=I_PMC_bottom*E_PMC
delta_bottom=delta/2 "Opening displacement of top arm associated with crack length"
"Force applied, bending moment and strain energy stored in bottom arm"
M_2=P_2*a
P_2=3*delta_bottom*EI_bottom/a^3
U_2=P_2^2*a^3/(6*EI_bottom)
delta_U2=-9/2*delta_bottom^2*EI_bottom/a^4
"Total strain energy release rate"
G=-1/B*(delta_U1+delta_U2)
```

APPENDIX C

C.1 EES program using the analytical solution proposed by Williams [3.7]

```
"Fracture Mechanics Solutions for Asymmetric DCB Specimen - J. G. Williams"
"Specimen Geometry"
B=0.02527 [m] "Specimen width"
{a=0.07427 [m]} "Crack length"
h_Ti=0.000127 [m] "Thickness of Ti layer"
h_PMC=0.0021865 [m] "Thickness of each PMC layer"
{delta=0.015748 [m]} "Opening displacement associated with crack length"
"Material Properties"
"Plain weave T300-EPON862 PMC"
E_PMC=5.675*10^10 "E11 of PMC in Pascal"
{E_Ti=5.675*10^10 "E11 of PMC in Pascal - For convergence check"}
E_Ti=102*10^9 "Young's modulus of Ti in Pascal"
n=E_Ti/E_PMC
"Consider the top arm that contains 1 layer of PMC on top of aTi foil layer"
"Finding location of neutral axis"
"Let h_1 be the location of neutral axis from the top of PMC layer and h_2 be the location of
neutral axis from the bottom of Ti
layer"
h_1=(h_PMC^2/2+(h_Ti/2+h_PMC)*h_Ti*n)/(h_PMC+n*h_Ti)
h_2=h_PMC+h_Ti-h_1
delta_top=delta/2 "Opening displacement of top arm associated with crack length"
"Second moments of area with respect to the neutral axis"
I_PMC_top=1/12*B*h_PMC^3+B*h_PMC*(h_1-h_PMC/2)^2
I_Ti=1/12*B*h_Ti^3+B*h_Ti*(h_2-h_Ti/2)^2
I_Total_top=I_PMC_top+I_Ti
EI_top=I_PMC_top*E_PMC+I_Ti*E_Ti
"Force applied, bending moment in top arm"
P_1=3*delta_top*EI_top/a^3
M_1=-P_1*a
"Consider the bottom arm that contains only 1 layer of PMC. Second moment of area of bottom
arm:"
I_PMC_bottom=1/12*B*h_PMC^3
EI_bottom=I_PMC_bottom*E_PMC
delta_bottom=delta/2 "Opening displacement of top arm associated with crack length"
"Force applied, bending moment and strain energy stored in bottom arm"
M_2=P_2*a
P_2=3*delta_bottom*EI_bottom/a^3
psi=EI_bottom/EI_top
psi=((1-xi)/xi)^3
"Consider half of the entire DCB that contains 1 layer of PMC on top of half ofTi foil layer"
"Finding location of neutral axis"
"Let h_1 be the location of neutral axis from the top of PMC layer and h_2 be the location of
neutral axis from the bottom of Ti
layer"
h_1h=(h_PMC^2/2+(h_Ti/4+h_PMC)*h_Ti/2*n)/(h_PMC+n*h_Ti/2)
```

h_2h=h_PMC+h_Ti/2-h_1h
"Second moments of area with respect to the neutral axis"
I_PMC_toph=1/12*B*h_PMC^3+B*h_PMC*(h_1h-h_PMC/2)^2
I_Ti_h=1/12*B*(h_Ti/2)^3+B*h_Ti/2*(h_2h-h_Ti/4)^2
I_Total_toph=I_PMC_toph+I_Ti_h
EI=I_PMC_toph*E_PMC+I_Ti_h*E_Ti
"Strain energy release rates"
G_I=1/(B*EI)*(M_2-psi*M_1)^2/(16*(1-xi)^3*(1+psi))
G_II=1/(B*EI)*(3*(1-xi)*(M_1+M_2)^2)/(16*xi^2*(1+psi))
G=G_I+G_II
Ratio_mixmode=G_II/G_I*100[%]